



Università Politecnica delle Marche
Scuola di Dottorato di Ricerca in Scienze dell'Ingegneria
Curriculum in Ingegneria Civile, Edile e Architettura

Dynamics induced by steep waves at a vertical slender cylinder in deep waters: laboratory experiments

Ph.D. Dissertation of:
Giulia Antolloni

Advisor:

Prof. Alessandro Mancinelli

Coadvisors:

Prof. Maurizio Brocchini

Prof. Atle Jensen

Curriculum supervisor:

Prof. Stefano Lenci

XVII edition - new series

Acknowledgements

I would like to thank all the people I met along my Ph.D. who, consciously or unconsciously, directly or not, contributed to the realization of this thesis. This work was possible only thanks to the support and the collaboration by each one of you.

First, my gratitude goes to my supervisor Prof. Alessandro Mancinelli, for having considered me up and gave me the possibility to attend the PhD course. I would like to thank my Italian coadvisor Prof. Maurizio Brocchini, who accepted to help me when I was in difficult and navigated me through the thesis. Particularly thanks for having helped me to conduct my research experience abroad.

I would like to express my deep gratitude to Prof. Atle Jensen, my Norwegian coadvisor, for having accepted to host me in his institution's laboratory, and to all of the team of the Hydrodynamics Laboratory of the University of Oslo, who have been very friendly and gave me any kind of support for the experiments. I spent some very special moments there and it was one of the most exciting experience in my life. Particular thanks go to the laboratory engineer Olav Gundersen: without his help, everything in the laboratory would be much harder to attain.

A very special thanks to Prof. Carlo Lorenzoni, for his never-ending encouragement during this period.

Thanks to all my colleagues of department, with which I shared the joys and the pains of the Ph.D. Special gratitude to Eleonora, my partner-in-crime, for having “fighting” with me and for her infinite patience.

Finally, I am very grateful to my family and Mattia, who always were very comprehensive and ever sustained all my decisions.

Abstract

Steep water waves may be responsible for damages to offshore structures as inducing a high-frequency resonant response, commonly known as *ringing*. The occurrence of ringing has been recently found to be in conjunction with a peak in the load timeseries, named *secondary load cycle*, whose causes are still not properly known. The presence of a secondary load means a wave excitation at higher harmonic frequencies which may induce a tuned build-up of resonant high-frequency vibrations of the structure with burst-like characteristics. The prediction of ringing is thus subject of attention by research community, because an adequate understanding of the underlying physical processes has not been still reached.

In this thesis, an experimental study on the forces upon, flow separation and vortex formation behind a bottom-hinged, surface-piercing, vertical, slender cylinder forced by steep waves, both breaking and non-breaking, is presented. A complex experimental setup was arranged, innovative in the sense that combines the use of many different experimental measurements techniques at the same time, thus increasing the information acquired about the phenomenon. Laboratory experiments consisted in the investigation of the flow by means of Particle Image Velocimetry (PIV) measurements over four horizontal planes parallel to the bottom at different elevations and downstream of the cylinder. In addition, measurements of the wave force acting on the cylinder and of the elevation of the incoming wave were made, synchronously with the acquisition of images.

PIV results showed the occurrence of flow separation and the formation of vortices for many of the breaking waves cases and for all the non-breaking waves, but with a completely different fashion. A correlation between the vorticity generation appearance and some wave parameters, as the wave period T , the dimensionless wavenumber kR and the wave slope $k\eta$ is attempted, limiting to the small size of the test matrix.

Furthermore, a correspondence between the secondary load cycle and the vortical structures has been found: vortex formation starts just after the wave crest has passed, at a stage where a second peak occurs in the force signal, at a loading stage correspondent to one quarter of the wave period following the main load peak, recognized as secondary load cycle. The occurrence of the phenomenon has been described also through some synthetic governing parameters, like the Keulegan-Carpenter number (KC) and the Froude number (Fr), as well as kR and $k\eta$. For the presented experiments, the secondary load cycle is observed for $Fr > 0.6$, $k\eta_c > 0.25$ and $kR > 0.1$. Although the fairly limited test matrix, all these features of the phenomenon are in agreement with the limits of $Fr > 0.4$ (and some weak events for $Fr \sim 0.35$) and for $k\eta_c > 0.3$ and kR in the range 0.1-0.33 provided by the experiences of Chaplin et al. (1997), Grue and Huseby, 2002, Suja-Thauvin et al. (2017) and Riise et al. (2018b) on the occurrence of the secondary load cycle. Moreover, the relationship between the shed vorticity and the hydrodynamic loads is investigated insights through the calculation of force induced by vorticity fields (Wu et al., 2007). The comparison between calculated force by vorticity and measured force acting on the cylinder, together with the visualization of vortex patterns, proved that the vortex generation and secondary load are correlated, but the vortex formation is not the only physical explanation for the secondary load cycle occurrence.

Concerning the contribution of vortical structures to the excitation of high-order wave force on high-frequency ringing response, disagreement with evidences provided by the recent CFD-computation by Paulsen et al., 2014 and Kristiansen and Faltinsen (2017) is seen, being the measured vortex generation tinier (20-30% of the cylinder radius) than what obtained by the authors. Furthermore, the occurrence of SLC and ringing response is found to coincide and both free surface and flow separation effects are seen to originate the nonlinear high frequency forces driving the ringing response (Riise et al., 2018b).

Contents

List of Figures	xiii
List of Tables.....	xvii
Chapter 1 INTRODUCTION	1
1.1 Thesis objective	1
1.2 Background.....	2
1.3 Outlines of the thesis.....	6
Chapter 2 THEORETICAL FUNDAMENTALS.....	7
2.1 Deep-water wave theory	7
2.1.1 Breaking waves in deep waters	11
2.1.2 Kinematic formulations for steep waves: the Stokes theory	13
2.2 Flow around a cylinder in oscillatory flow	17
2.2.1 Flow regime and vortex formation	19
2.3 Wave loads on vertical slender cylinders	22
2.3.1 Wave breaking load	23
2.3.2 Higher-order wave loads	25
2.3.2.1 Secondary load cycle.....	27
Chapter 3 METHODOLOGY	29
3.1 Quantitative imaging techniques	29
3.1.1 Particle Image Velocimetry (PIV).....	30
3.2 Wave focusing technique.....	34
3.2.1 Wave focusing generation in the wave flume	36
3.3 Vortices and Coherent Structures	38
3.3.1 Vortex identification criteria	39
Chapter 4 LABORATORY EXPERIMENTS	43
4.1 The wave flume	43
4.2 Experimental overview	43
4.2.1 Physical model.....	45
4.2.2 Instrumentation.....	46

4.2.2.1	Wave surface elevation measurements	46
4.2.2.2	Force measurements	47
4.2.2.3	Pressure measurements	49
4.2.2.4	PIV arrangements	50
4.2.3	Synchronization system	53
4.3	Experimental investigation of the flow upstream the cylinder: Setup1.	55
4.4	Experimental investigation of the flow downstream the cylinder: Setup2.	57
4.5	Wave generation	60
4.6	Wave characteristics	60
Chapter 5	RESULTS AND DISCUSSION.....	63
5.1	Overview of the acquired data	63
5.2	Data analysis	64
5.2.1	Elevation signals.....	64
5.2.2	Force signals	65
5.2.3	PIV images analysis	67
5.2.4	PIV post-processing: vorticity analysis	68
5.3	Vortex generation and evolution.....	69
5.4	Secondary load cycle dynamics	76
5.5	Vortex-induced force evaluation	82
5.6	Discussion.....	93
Chapter 6	CONCLUSIONS.....	99
References.....		103

List of Figures

Figure 1. Applicability ranges of various wave theories (from Le Méhauté, 1969). d : mean water depth; H : wave height; T : wave period; g : gravitational acceleration.....	8
Figure 2. A physical illustration of sinusoidal (a) and asymmetric (b) wave profiles.	10
Figure 3. Wave elevation signal: comparison of experiments with wave theories from the work of Veic et al. (2016).....	11
Figure 4. Breaking wave in deep ocean. Left panel: spilling breaking wave. Right panel: plunging breaking wave. From Banner and Peregrine (1993).....	12
Figure 5. Meaning of the KC number: definition sketch. From Sumer and Fredsøe (2006).....	18
Figure 6. Regimes of flow around a smooth, circular cylinder in an oscillatory flow. $Re = 10^3$	19
Figure 7. Vortex shedding regimes around a smooth circular cylinder in an oscillator flow. NL is the number of oscillations in the lift force per flow cycle. From Sumer and Fredsøe (2006).	21
Figure 8. Wave force induced on a slender vertical cylinder: sketch for Morison's formulation. From Matteotti (1995).	22
Figure 9. Sketch for the breaking wave impact force.....	24
Figure 10. Occurrence of the secondary load cycle, visible on the excitation force (left panel). Estimation of F_{SLC} parameter (right panel). From Suja-Thauvin et al.(2017).....	28
Figure 11. Cross-correlation. <i>Top panel</i> : Example of the formation of the correlation plane by direct cross-correlation: here a 4×4 pixel template is correlated with a larger 8×8 pixel sample to produce a 5×5 pixel correlation plane. <i>Bottom panel</i> : Composition of peaks in the cross-correlation function. From Raffel et al. (1998).	32
Figure 12. The medium-size wave flume of the Hydrodynamics Laboratory (left panel). Details of the wavemaker (top right panel) and of the absorbed beach (bottom right panel).....	44
Figure 13. Global sketch of the experimental setups. The cylinder reports all instruments in use: wave gauges close to the cylinder (WG3, WG4, in yellow) and force measurements system (FX1, FX2, in black) common to	

both configurations; pressure transducers (P1-P5, red dots) relative to Setup1 and horizontal sheets (POS0-POS4, green lines) relative to Setup2. Dimensions are expressed in m.	46
Figure 14. Acoustic wave gauges system for measurements of the water level. Left panel: in-line arrangement of acoustic wave gauge. Right panel: acquisition controller box.	47
Figure 15. Force measurement system arrangement. Left panel: general view. Right panel: detail of load cell.....	48
Figure 16. Miniaturized pressure transducer.	49
Figure 17. Light sources: LED line (left panel) and laser (right panel).	51
Figure 18. CCD cameras. Left panel: Teledyne DALSA. Right panel: Photron FASTCAM SA5.	52
Figure 19. Seeding particles.	52
Figure 20. Timing diagram of the synchronization system related to the Setup 2.	54
Figure 21. Setup1. Configuration of pressure transducers, namely P1 to P5, from top to bottom. Left panel: cylinder with pressure transducers at the frontline, i.e. the rotation of the cylinder is equal to 0° . Right panel: counterclockwise rotation of 15° of the cylinder with pressure transducers.	56
Figure 22. View of the final configuration of Setup1, right after the seeding with particles.....	57
Figure 23. Sketch of the PIV arrangement for Setup2.	58
Figure 24. View of the final configuration of Setup2, during a PIV acquisition.	59
Figure 25. Example of curve fitting on wave 3.1.	65
Figure 26. Example of filtering of a force signal: wave 1.1 (top panel) and 4.1 (bottom panel).....	66
Figure 27 Example of instantaneous velocity field from PIV analysis: case 1.1 (left panel) and case 3.1 (right panel), at different times subsequent to the wave passage, with incident flow from bottom to top.....	68
Figure 28. Vortex evolution for case 1.1. Top panel: Time history of the wave elevation. Bottom panel: Vorticity maps at times (A-D) and at horizontal planes (POS1-POS3). Incident flow from bottom to top.....	72
Figure 29. Vortex evolution for case 3.1. Top panel: Time history of the wave elevation. Bottom panel: Vorticity maps at times (A-D) and at horizontal planes (POS1-POS3). Incident flow from bottom to top.....	73
Figure 30. Vortex evolution for case 3.3. Top panel: Time history of the wave elevation. Bottom panel: Vorticity maps at times (A-D) and at horizontal planes (POS1-POS3). Incident flow from bottom to top.....	74
Figure 31. Vortex evolution for case 4.1. Top panel: Time history of the wave elevation. Bottom panel: Vorticity maps at times (A-D) and at horizontal planes (POS1-POS3). Incident flow from bottom to top.....	75

Figure 32. SLC dynamics for case 1.1. Top panel: Time histories of wave elevation (in blue) and wave-exciting moment (in red). Bottom panel: Evolution of the vorticity at times (A'-D') significant for the SLC, and at horizontal planes (POS1-POS3). Incident flow from bottom to top.....	77
Figure 33. SLC dynamics for case 2.1. Top panel: Time histories of wave elevation (in blue) and wave-exciting moment (in red). Bottom panel: Evolution of the vorticity at times (A'-D') significant for the SLC, and at horizontal planes (POS1-POS3). Incident flow from bottom to top.....	79
Figure 34. SLC dynamics for case 3.1. Top panel: Time histories of wave elevation (in blue) and wave-exciting moment (in red). Bottom panel: Evolution of the vorticity at times (A'-D') significant for the SLC, and at horizontal planes (POS1-POS3). Incident flow from bottom to top.....	80
Figure 35.. SLC dynamics for case 4.1. Top panel: Time histories of wave elevation (in blue) and wave-exciting moment (in red). Bottom panel: Evolution of the vorticity at times (A'-D') significant for the SLC, and at horizontal planes (POS1-POS3). Incident flow from bottom to top.....	81
Figure 36. Vortex-induced force evaluation for case 1.1. Top panel: Time histories of measurement wave-induced force on the cylinder (in black) and calculated transversal (in red) and inline (in blue) drag force components induced by vorticity, at the elevations corresponding to horizontal planes (POS1-POS3). Bottom panel: evolution of the vorticity at significant times (A''-E''), and at horizontal planes (POS1-POS3). Incident flow from bottom to top.	86
Figure 37. Vortex-induced force evaluation for case 4.1. Top panel: Time histories of measurement wave-induced force on the cylinder (in black) and calculated transversal (in red) and inline (in blue) drag force components induced by vorticity, at the elevations corresponding to horizontal planes (POS1-POS3). Bottom panel: evolution of the vorticity at significant times (A''-E''), and at horizontal planes (POS1-POS3). Incident flow from bottom to top.	88
Figure 38. Vortex-induced force evaluation for case 3.1. Top panel: Time histories of measurement wave-induced force on the cylinder (in black) and calculated transversal (in red) and inline (in blue) drag force components induced by vorticity, at the elevations corresponding to horizontal planes (POS1-POS3). Bottom panel: evolution of the vorticity at significant times (A''-E''), and at horizontal planes (POS1-POS3). Incident flow from bottom to top.	89
Figure 39. Vortex-induced force evaluation for case 2.1. Top panel: Time histories of measurement wave-induced force on the cylinder (in black) and calculated transversal (in red) and inline (in blue) drag force components induced by vorticity, at the elevations corresponding to horizontal planes (POS1-POS3). Bottom panel: evolution of the vorticity at significant times (A''-E''), and at horizontal planes (POS1-POS3). Incident flow from bottom to top.	91

- Figure 40 Vortex-induced force evaluation for case 3.3. Top panel: Time histories of measurement wave-induced force on the cylinder (in black) and calculated transversal (in red) and inline (in blue) drag force components induced by vorticity, at the elevations corresponding to horizontal planes (POS1-POS3). Bottom panel: evolution of the vorticity at significant times (A''-E''), and at horizontal planes (POS1-POS3). Incident flow from bottom to top. 92
- Figure 41. Extreme response events identification. Experimental data (red markers) and data by Riise et. al, 2018 (black dots). Open square: vorticity generation occurrence with no SLC (case 3.1). Filled square: vorticity generation and SLC (cases 1.1, 1.2, 3.1, 4.1). Open triangle: no vorticity, presence of SLC (cases 2.1, 2.3). Dashed line: $KC=0.5$. Continuous line: $Fr=0.4$. Adapted from Fig. 10d by Riise et al. (2018b)..... 97

List of Tables

Table 1. Position of the investigated horizontal light sheets on the backside of the cylinder.	59
Table 2. Parameters of the tested waves: η_c surface elevation at the crest measured by WG4, T_{tt} trough-to-trough period, T_f zero up-crossing period of the force history, $T_{av}=(T_{tt}+T_f)/2$ average period, L wave length, k wave number, $k\eta_c$ wave slope, kR dimensionless wave number with respect to the cylinder radius, Re Reynolds number, KC Keulegan-Carpenter number and Fr Froude number.	62
Table 3. Reorganized parameters of the tested waves in light of results available: η_c surface elevation at the crest measured by WG4, T_{tt} trough-to-trough period, T_f zero up-crossing period of the force history, T_{av}^* dimensionless average period, L wave length, k wave number, $k\eta_c$ wave slope, kR dimensionless wave number (with respect to the cylinder radius), Re Reynolds number, KC Keulegan-Carpenter number and Fr Froude number. VG means Vortex Generation, while SLC secondary load cycle, whose presence is indicated by ‘Y’(yes) or ‘N’ (no).	98

Chapter 1

INTRODUCTION

In the last decades, the worldwide increasing demand for energy, especially from the renewable forms, such as wind power plants, led the offshore industry to move its activities towards deeper waters. Although the aim is to enhance the energy production, an increase in installation and maintenance costs must be faced because structures are more often exposed to high dynamic loads caused by the harsh environment, thus they are more prone to be damaged (for example by fatigue, vibrations and resonance). Starting from the observation of episodes of damages involving offshore structures, especially on platforms and wind turbines mainly constituted by cylindrical sub-structures, it has been revealed (Jefferys and Rainey, 1994; Faltinsen et al., 1995; Chaplin et al., 1997) that even the impact of steep waves, both breaking and near-breaking waves, may induce destructive effects such as *ringing*, a high frequency transient resonant response of the structure that may arise even if the wave period is far from the eigenperiod of the structure (Stansberg et al., 1995; Marthinsen et al., 1996; Welch et al., 1999). Notwithstanding the many efforts made by the research community on the comprehension of the phenomenon, its causes of occurrence and effects are still not fully understood.

1.1 Thesis objective

The present thesis aims to improve the knowledge on the dynamic processes arising around a vertical slender cylinder hit by a steep wave, breaking and non-breaking, in deep waters. Specific focus is on the *secondary load cycle*, a second load peak arising after the main peak in force signal, whose connection with the ringing phenomenon is likely.

Findings on the generation mechanisms of the secondary load cycle are still insufficient, thus an experimental campaign was conducted aimed at collecting useful data and information on this phenomenon.

In light of the complexity of the topic, which involves several nonlinear processes, such as the breaking and the impulsive nature of the wave-induced load on the structure, a broad investigation is needed. The laboratory experiments have been designed mainly focusing on the investigation of flow separation and vortex formation on the downstream side of the cylinder, in conjunction both with the identification of the specific features of the measured force signal, e.g. the second load cycle, and with the incoming wave characteristics.

The broad overview of the results coming from the experiments, that covered all the above-mentioned aspects, may constitute the ground on which to build an interpretation of the conditions that give rise to the higher-order response of vertical cylinders in deep waters when they are exposed to steep waves.

The present research has been undertaken in an effort to improve the understanding the ringing phenomenon in view of the applications typical of the oil and gas industries, renewable energy industries and the scientific community. It is widely recognized that ringing-induced excitation threatens the safety of offshore structures, and, therefore, arise the need to take it into consideration within standards codes as an important issue during the design process.

1.2 Background

Steep near-breaking and breaking waves, likely occurring in deep waters, make structures suffered to large high-frequency loads, in the same extent of more extreme wave events. Furthermore, the nonlinear inertia loading transferred by steep waves contributes to the high-frequency ringing response build-up in structures, together with the nonlinearity of the wave motion and of the dynamic response of the structure itself (Tromans et al., 2006).

Ringing generates very high stress level with a burst of only a few higher harmonic oscillations (Chaplin et al., 1997) and imposes a serious potential danger to the structures.

Field observations revealed that cylindrical monopiles, which are by far the most popular support structures for gravity-based platforms (GBS) and wind turbine substructures, being also used in tension-leg platforms (TLP), may be affected by ringing. The first observations of the ringing responses date back to the mid-1990s and were obtained at the Hutton and Heidrun oil production platforms and at the deep water concrete towers of Draugen and Troll platforms in the Norwegian Sea fields (Natvig and Teigen, 1993). Evidence of these tests was discussed also in Jefferys and Rainey (1994), reporting examples of the ringing-type responses from the Heidrun model tests. Again, the occurrence of ringing was also observed at the Norwegian oil production Gullfaks C during operation in storm conditions (Langen et al., 1998).

These experiences motivated the significant amount of research that followed over the years. On the theoretical side, it is worth recalling the relevant efforts on the estimation of higher-order harmonic force on cylinders. An analytical solution accounting up to the third-harmonic of the wave forcing by regular waves in deep water was derived by Faltinsen et al. (1995a). This is known as the FNV method, and has been recently generalized to finite water depths by Kristiansen and Faltinsen (2017), whereas third-harmonic forces theories for irregular waves were presented by Newman (1996), Krokstad et al. (1998) and Johannessen (2011).

Recently, the strong worldwide incentive towards renewable energy, which has driven the development of wind farms, which are planned to expand more and more, renewed the interest in the investigation of higher-harmonic wave loads and in the prediction of the associated ringing phenomenon. The concern arise from the fact that, the trend in increasing the size of the offshore wind turbines together with the limited blade tip velocity, led to a decrease of the natural frequencies of the support structures, thus making these structures more prone to ringing responses (Suja-Thauvin et al., 2014).

The problem of predicting the ringing response, in terms of identification of hydrodynamic processes at the base of higher-harmonic load phenomena and ringing occurrence, have stimulated many experimental and numerical studies over the years. Particular focus has been on the investigation of the flow characteristics at and forces on the cylinders exposed to steep waves.

The early experiment in infinite water depths was conducted by Grue et al. (1993) on restrained vertical cylinder. A higher harmonic oscillation was first identified in the recorded force measurements for certain values of wave height. This phenomenon, called *secondary load cycle*, was also reported by Chaplin et al. (1997) and Chaplin and Rainey (2003) as due to focusing waves and by Grue and Huseby (2002) as evolving during the transient of a regular wave train; the same phenomenon has been observed by Stansberg et al. (1995) as forced by irregular waves.

The secondary load cycle looks like an additional force peak that occurs shortly prior to the time of minimum loading, at about one quarter wave period after the force main peak, and lasts for about 15% of the wave period (Grue et al., 1993). Grue and Huseby (2002) investigated the secondary load cycle for both a small and a moderate scale cylinder, i.e. for cylinder of radius 3cm and 6cm respectively. They found that the occurrence of the secondary load cycle depends on the wave steepness, in agreement with Chaplin et al. (1997). In particular, in small-scale experiments, the secondary load cycle was observed for waves of slope $k\eta_c > 0.3$ in the range of $kD < 0.66$, where k is the wavenumber, η_c the wave elevation at crest and D the diameter of the cylinder; whereas for moderate-scale, the phenomenon was observed for smaller wave slopes. Furthermore, Grue and Huseby (2002) suggested the Froude number Fr ($Fr = \omega\eta_c / \sqrt{gD}$ where ω is the wave frequency) as a governing parameter for the secondary load cycle, reporting the occurrence of such small-scale load for $Fr > 0.35$. These trends in the occurrence of the phenomenon have been confirmed also by the most recent experiences (Li et al., 2014; Suja-Thauvin et al., 2017; Fan et al., 2018; Riise et al., 2018b, 2018a; Liu et al., 2019).

The secondary load cycle has been regarded to largely contribute to the higher-harmonic component of the total force exerted by incident steep waves on the cylinder (Grue et al., 1993) and this aspect has been put in relation with the ringing motion of vertical cylinders (Chaplin et al., 1997; Stansberg, 1997; Grue and Huseby, 2002) . However, a comprehensive knowledge of the ringing generations mechanisms is still lacking and the origin of the secondary load cycle, and its possible relation with the ringing occurrence, are still under discussion.

Grue and Huseby (2002) documented that pronounced ringing occurs for the same wave parameters as a secondary load cycle in the wave force. Besides, they attributed the

appearance of the secondary load cycle to a suction force acting at about one cylinder radius below the still-water level and describe the phenomenon as a resonance between a local induced flow and the cylinder. The conjecture that the secondary load may be a cause of ringing response has been supported also by the works of Chaplin *et al.* (1997), Suja-Thauvin and Krokstad (2016) and Riise *et al.* (2018b).

Differently, Rainey (2007) ascribed the origin of the secondary load cycle to a kind of wave run-up on the downstream side of the cylinder, in agreement also with evidences by Krokstad and Solaas (2000), thus attributing no direct connection with the nonlinear behaviour of the ringing force. Other experimental tests, concerning steep and breaking irregular waves on cylinders (Bachynski *et al.*, 2017; Suja-Thauvin *et al.*, 2017) reported both the secondary load cycle and ringing response, but without finding a correlation between the characteristics of the two phenomena. In fact, some ringing events occurred with no presence of secondary load cycle, suggesting that the secondary load cycle does not necessary induce ringing response.

More recently, computational fluid dynamics models have been used to study the higher harmonic wave loads in periodic waves. Paulsen *et al.*, 2014 discussed the physics of the secondary load cycle, recognizing it as "*[...] an indicator of strong non-linear flow more than a contributor to the resonant forcing*". In addition, the observation of a rather strong vortex downstream the cylinder owing to the return flow that has been seen in conjunction with the secondary load cycle, suggested it could contribute to the origin of the secondary load cycle. Lately, a similar CFD-calculation of such large vortex formation was presented as part of the theoretical and experimental study by Kristiansen and Faltinsen (2017), also in periodic waves. Moreover, with the aim to include turbulence effects, the numerical study by Liu *et al.* (2019) in breaking waves, pointed out a process of water up-rushing on the back of the cylinder just after the wave front had passed the cylinder, at which the secondary load cycle begins to occur and develops up to vanishing.

Those latter studies have opened a new direction of investigation of the topic focused on the role of flow separation and vortex formation which is still poorly explored.

1.3 Outlines of the thesis

This thesis starts with a short overview of the main theoretical fundamentals at the basis of the investigated phenomena. Wave theories regarding solitary and breaking waves in deep water are reported in Chapter 2, together with aspects relative to the hydrodynamics induced by these waves on vertical slender cylinders. Focus on higher-harmonic wave load is given and an analytical description of waves is provided therein.

Chapter 3 includes a theoretical description and practical information of the measuring methods used in the thesis. Several different aspects are covered. First, a short introduction to Particle Image Velocimetry (PIV) and the analysis of images are given. Secondly, a description of the wave focusing generation technique is provided. Finally, a discussion on vortex identification criteria in literature is developed.

A practical full description of the experiments, measuring tools and experimental techniques is illustrated in Chapter 4. Experimental setups are described in detail, pointing out the difficulties in their realization. The laboratory instruments needed for the work are described. Information about the wave input and the wave characterization is also given.

The main PIV results, in terms of vorticity and velocity fields, are discussed in conjunction to both force and surface elevation signals in Chapter 5. The secondary load cycle occurrence is discussed. A brief summary of the results and suggestions for further improvements of the work can be found in Chapter 6.

Chapter 2

THEORETICAL FUNDAMENTALS

2.1 Deep-water wave theory

The great variety of water waves, e.g. from storm waves generated by wind, to seiches in harbour basins, up to tsunami waves generated by earthquakes, to name but a few, makes it evident that a general analytical solution of wave motion does not exist. Indeed, a large amount of physical aspects are involved in the generation and characterization of wave motion.

Numerous water wave theories have been thus developed providing approximate solutions for the study of wave motion which are applicable to different environments dependent on the specific environmental parameters, e.g. water depth, wave height and wave period.

Because of the simplifying assumptions to be introduced in the attempt for giving solutions, a water wave theory is valid within its own established limits of applicability. One of the main challenges for engineers is the adoption of the most appropriate mathematical approach valid for the description of the problem under study.

Figure 1 illustrates qualitatively the range of validity of the main wave theories in literature. The regions are described in terms of H/T^2 and d/T^2 , i.e. of wave height H and water depth d in relation to wave period T . Water depth is used to distinguish between shallow-water waves for $d/L < 0.05$ and deep-water waves for $d/L > 0.5$ (where L is the wavelength), while in between (see the vertical dashed lines in the graph) are intermediate depth waves. Waves in shallow water are significantly affected during their propagation to

shore by seabed level changes, while deep water waves are not affected by the seabed topography.

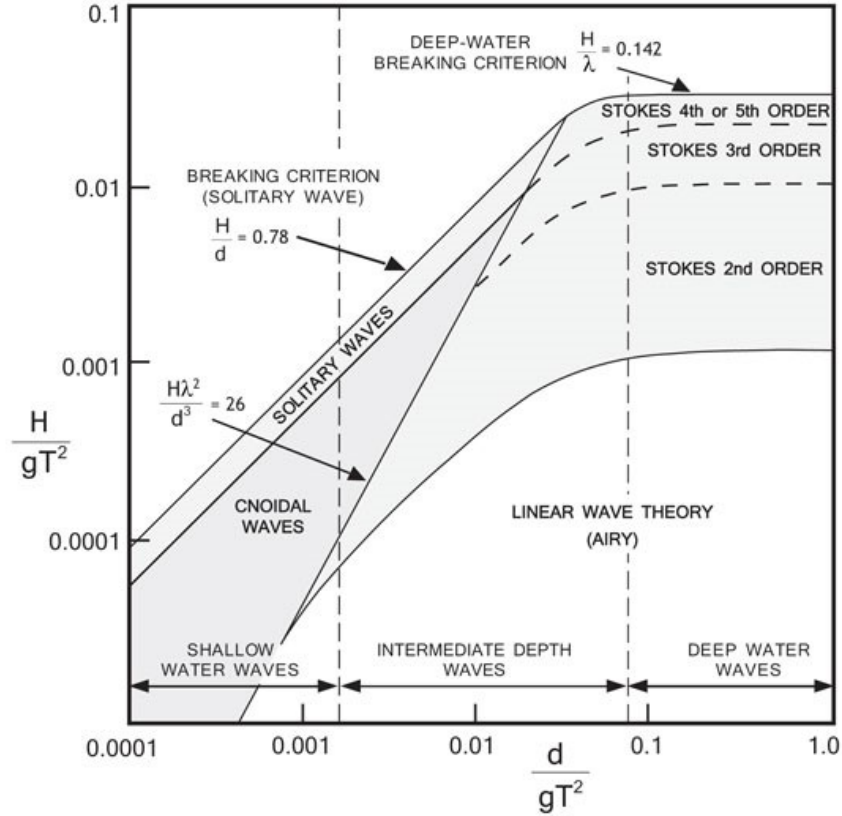


Figure 1. Applicability ranges of various wave theories (from Le Méhauté, 1969). d : mean water depth; H : wave height; T : wave period; g : gravitational acceleration.

The graph is limited by a breaking criteria which implies that there is a maximum value for the wave steepness, which is function of the relative depth. A number of equivalent definitions have been provided for breaking criteria. Breaking occurs when: a) the particle velocity at the crest becomes larger than the wave velocity, b) the pressure at the surface is incompatible with the atmospheric pressure, c) the particle acceleration at the crest tends to separate the particles from the bulk of water surface, d) the free surface becomes vertical. Accordingly, the following theoretical limits were reported in the graph:

In deep water
(Mitchell limit)
$$\frac{H}{L} < 0.142 \quad (2.1)$$

In intermediate water depth
(Miche formula)
$$\frac{H}{L} < 0.14 \tanh\left(\frac{2\pi d}{L}\right) \quad (2.2)$$

In case of solitary waves

$$\frac{H}{d} = 0.78 \quad (2.3)$$

The analyses that follow focus on deep-water wave theories, which are limited to a flat bottom and a constant uniform water depth. In the framework of the theories most commonly used in the design of offshore structures, they are: (1) linear Airy wave theory, (2) Stokes higher-order theory and (3) stream function theory. A brief discussion on their limits and regions of applicability is developed, following Chakrabarti (1987).

At the basis of all water wave theories there are the assumptions of two dimensional periodic and uniform waves, of horizontal ocean floor giving constant depth d from the still water level (swl) and of progressive waves in the horizontal direction. The main challenge for any wave theory is to determine the unknown boundary condition of the free surface, starting from the solution of the velocity potential, Φ or, equivalently, of the stream function, Ψ . Airy and Stokes formulations are based on the potential function and are developed around the wave height as a perturbation parameter that is limited to a given order of the wave theory. Differently, the stream function is expressed in a general order and a numerical solution is sought from the formulation.

The small amplitude wave theory is the simplest and most used of all theories. It is based on the assumption that the wave height is small compared to both wave length and water depth. With this assumption, the free surface boundary conditions can be linearized by neglecting the wave height terms beyond the first order. The solution of Φ takes the form of a power series in terms of a non-dimensional perturbation parameter ε , defined as the wave slope (wave height/wave length) as $\varepsilon = ak$, in which k is the wave number, defined as $k = 2\pi/L$ and a is the amplitude, here equal to $H/2$. The linear theory gives symmetric profiles about the swl and it is upper limited by the wave height at which waves becomes unstable and break. In deep water the limiting wave steepness is represented by the Mitchell limit reported by Equation 2.1.

Around this steepness limit, the loss in symmetry of the wave surface is relevant. Asymmetry consists in the wave crest becoming more and more narrow and steep, whereas the wave trough becomes long and flat (Figure 2). Nonlinearity of wave manifests itself in

an increased steepness of the wave, and so the sinusoidal wave theory by Airy breaks down. Higher order perturbation solutions must, therefore, be adopted.

Stokes employed the perturbation technique and expanded the solution to higher orders, taking into account the nonlinear part of the solution. This formulation is taken to be valid for $H/d \ll (kd)^2$, for $(kd) < 1$ and $H/L \ll 1$ which constitute severe restrictions on the wave heights in shallow water, thus the Stokes theory is not generally applicable to shallow-water waves.

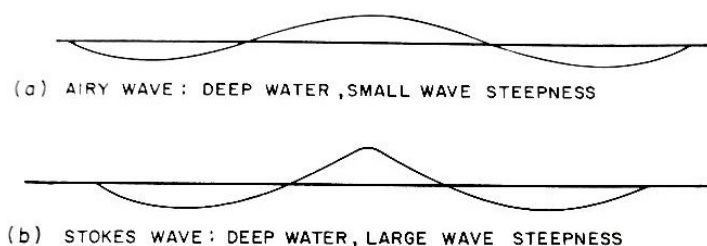


Figure 2. A physical illustration of sinusoidal (a) and asymmetric (b) wave profiles.

From Le Méhauté (1969).

Perturbative terms of increasing order are included in the velocity potential expression as the higher order considered. The mathematics is clearly more cumbersome and complexity increases with the increase in accuracy, but Stokes formulation up to the fifth-order and coefficients formulations are provided in literature (Skjelbreia and Hendrickson, 1960).

Not reported in the graph, but well known in literature, is the stream function theory developed by Dean (1965). It is a nonlinear wave theory, related to that of Stokes, but based on a stream function representation of the flow. A more detailed description of this theory is beyond the scope of this discussion, but it would point out the advantage that no restriction is imposed to the wave form. The wave can change form as it propagates due to the interaction of components at various phase speeds and relative motion. In general, the stream function theory may be appropriate and consistent over most of the wave parameter domain of Figure 1 except at very low ends of the values.

In conclusion, in deep water ($d/L > 0.5$ or $d/T^2 > 1$), the Stokes nonlinear theory is more appropriate to describe waves fitting the near-breaking conditions with increasing accuracy for increasing order of expansion. However, the best fit for the kinematic condition is

found for the stream function theory. Figure 3 is reported as example of the wave description provided by the above-mentioned wave theories, noting that steep waves in deep water need to be described by nonlinear wave theories.

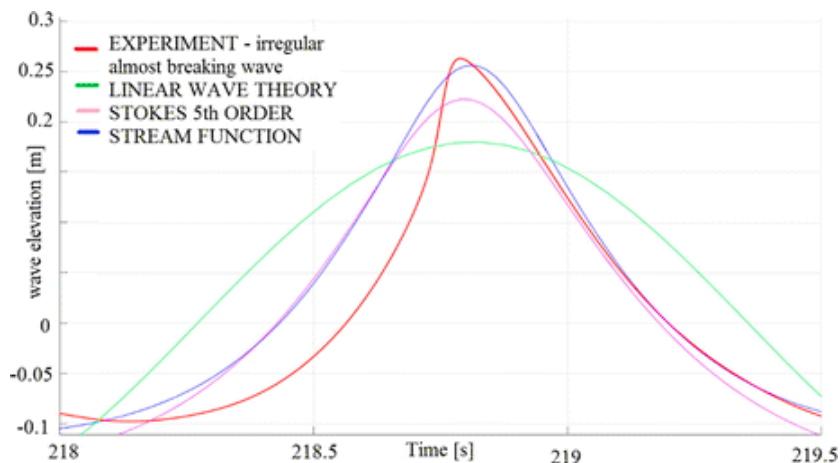


Figure 3. Wave elevation signal: comparison of experiments with wave theories from the work of Veic et al. (2016).

2.1.1 Breaking waves in deep waters

Breaking waves play an important role in the exchange of mass, momentum, energy transfer between the atmosphere and the sea, which may have effects on climate as well as in turbulence generation and turbulence-wave interactions. Furthermore, knowledge of hydrodynamics of breaking waves has always been sought by the engineers community, interested in improving the design procedures of marine structures often subjected to impulsive and extreme wave loads transferred by breaking waves.

In nature, wave breaking can be observed in the open ocean as well as in regions near the coastline, but with completely different generating processes. Breaking waves are generally divided into two regimes: *deep water breaking waves*, where the water is sufficiently deep that the waves are not affected by the seabed topography, and *shallow water breaking waves*, where the waves break due to effects induced by changes in water depth.

With reference to breaking wave in deep water many reviews are available (Bonmarin, 1989; Banner and Peregrine, 1993; Melville, 1996; Perlin et al., 2013). Direct observation

and measurements in the field have shown that breaking waves are universally present over the ocean surface as well as in all environments where the deep-water condition is reached.

In this environment, two types of breaking waves were observed. *Spilling* (Figure 4, left panel) is the more typical breaking type in deep water. Spilling breaking waves are characterized by white-capping near the crest, due to entrained wave bubbles and drops created at the surface, gently spreading down the forward face of the wave. Secondly, *plunging breakers* (Figure 4, right panel) can occur, where the forward face of the breaker overturns violently into the slope of the preceding trough, causing splashes, eddies and large air entrainment. Even if the plunging breakers are more common on beaches, they may occur, with less frequency than spilling, also in deep water, usually during severe storms and represent the most dramatic event.

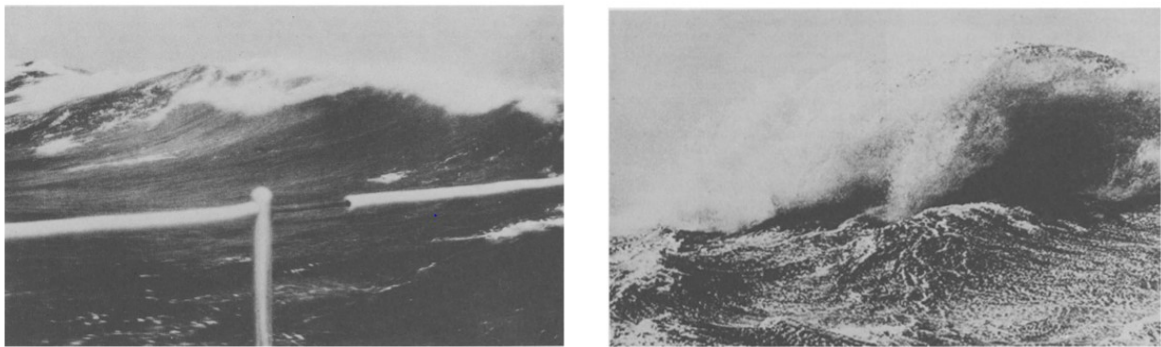


Figure 4. Breaking wave in deep ocean. Left panel: spilling breaking wave. Right panel: plunging breaking wave. From Banner and Peregrine (1993).

It is widely recognized that an individual wave breaking event starts when water particles near the wave crest develop a velocity in the wave propagation direction sufficiently large from them to fall down the front of the wave. If on one hand this phenomenon is evident during the propagation of a wave toward the shore, where the wave become steeper due to the effects of the variation of the seabed topography, on the other hand less intuitive are the mechanisms of generation of wave breaking in deep waters and the definition of the breaking criteria.

Direct observations in field and a large amount of investigation show that breaking in deep water may result from: i) the interaction of waves and currents, ii) direct forcing by wind

(Phillips, 1977), iii) intrinsic instabilities of the wave field (Melville, 1982), and iv) the constructive interference of a number of Fourier components. Melville and Rapp (1988) supported that the latest of such mechanisms may be the most important for waves near the peak of the spectrum, whereas the direct effect of wind forcing is likely to be of little significance near the peak of the spectrum, but may dominate at higher frequencies.

Especially in a random sea, where waves with different propagation directions interact, the superposition of wave components at different frequencies can occur. This may lead to the generation of a highly asymmetric non-steady wave, that can break if it reaches a certain breaking limit. The classical breaking criterion is represented by the geometric criterion that a wave at the point of breaking is a Stokes wave with a limiting crest angle of 120° and a maximum steepness $(ak)_{\max} = \pi/7$. Although, this is usually applicable, rarely a geometric criterion for breaking is applied because definition of wave height and slope can be ambiguous (Melville and Rapp, 1988). For this reason, the research moved towards the definition of global breaking criteria, also investigating the kinematics (Kjeldsen et al., 1980; Bonmarin and Ramamonjiarisoa, 1985; Longuet-Higgins, 1988) or energetics (Schultz et al., 1994) of wave breaking.

Furthermore, several instability mechanisms were observed that can provoke wave breaking in deep water. Tanaka (1983, 1985) demonstrated that periodic waves with wave steepness greater than 0.43 are unstable, a discovery that led Jililians (1989) to investigate more on the evolution of instability and its role on the onset of breaking, who found that the instability is concentrated near the crest. Another form of instability regarding wave trains was found by Benjamin and Feir (1967), this consisting in an infinitesimal long modulations of a wave train growing in amplitude until strongly modulated wave groups occur. Finally, three-dimensional instability was observed for steeper deep-water wave trains in which alternate crests grow at the expenses of those in between (Longuet-Higgins, 1978).

2.1.2 Kinematic formulations for steep waves: the Stokes theory

With the assumptions of fluid incompressible, inviscid and irrotational, the flow can be described by the potential function (or velocity potential), Φ . The velocity potential Φ and

the surface displacement η are determined from solving Laplace's equation (Equation 2.4) for the given boundary conditions.

The free surface kinematic condition of Equation 2.5 states that a particle lying on the free surface remains on the free surface over time. The free surface dynamic condition, based on the assumption that the atmospheric pressure outside the fluid is constant, is reported Equation 2.6 Finally, the no-slip condition at the seabed states that the velocity is zero at the horizontal seabed (Equation 2.7).

For uniform depth, the boundary value problem to be solved is conclusively written as:

$$\nabla^2 \Phi = 0 \quad \text{for } -h < z < \eta \quad (2.4)$$

$$\frac{\partial \eta}{\partial t} + \frac{\partial \Phi}{\partial x} \frac{\partial \eta}{\partial t} - \frac{\partial \Phi}{\partial x} = 0 \quad \text{at } z=\eta \quad (2.5)$$

$$\frac{\partial \Phi}{\partial t} + \frac{1}{2} (\nabla^2 \Phi) + gz = 0 \quad \text{at } z=\eta \quad (2.6)$$

$$\frac{\partial \Phi}{\partial z} = 0 \quad \text{at } z=-h \quad (2.7)$$

where x represents the horizontal axis and z the vertical axis of a two dimensional Cartesian coordinate system with origin at the undisturbed free surface.

The linear Airy theory provides the simplest way to predict the wave kinematics, under the assumption of small wave amplitude a with respect to the wave length. For a regular wave a possible solution to the linear problem is:

$$\eta = a \cos(kx - \omega t + \varphi) \quad (2.8)$$

$$\phi = a\omega \frac{\cosh k(z + h)}{k \sinh kh} \sin(kx - \omega t + \varphi) \quad (2.9)$$

where $\omega = 2\pi/T$ is the angular frequency, k and ω are related through the linear dispersion relation

$$\omega^2 = gk \tanh kh \quad (2.10)$$

and φ is a phase displacement, which may be set equal to zero with a suitable choice of the time/space origin.

Irregular waves may be composed by superposing plane wave components with different amplitudes and phases. By means of the linear Airy theory, the surface displacement and the potential function may appear as:

$$\eta = \frac{1}{2} \sum_j \left(a_j e^{i(k_j x - \omega_j t)} + c.c \right) \quad (2.11)$$

$$\phi = -\frac{1}{2} \sum_j \left(i a_j \omega_j \frac{\cosh k_j(z+h)}{k_j \sinh k_j h} e^{i(k_j x - \omega_j t)} + c.c \right) \quad (2.12)$$

where a_j is a complex amplitude containing both the modulus of the amplitude $|a_j|$ and the phase displacement $\varphi_j = \arg a_j$.

For the solution of the nonlinear boundary value problem, Stokes introduced harmonic power series in terms of a parameter containing the amplitude. In Stokes' original theory the parameter $\varepsilon = ak$ was used to expand the series. Looking at the surface displacement the most noticeable higher order effect is the second order contribution that makes both the crest and trough higher. Skjelbreia and Hendrickson (1960) developed a fifth-order method to calculate both the surface displacement and the kinematics with $\varepsilon = ak$ as the expansion parameter. Later, Fenton (1985) showed this method to be wrong at the fifth order and introduced the wave steepness $\varepsilon = kH/2$, where H is the wave height from crest to trough, as the expansion parameter.

Fenton's method for steady propagating waves at finite depth is:

$$\phi = (c - \bar{u})x + C_0 \sqrt{g/k^3} \sum_{i=1}^5 \varepsilon^i \sum_{j=1}^i A_{ij} \cosh jk(z+h) \sin jk(x-ct) + O(\varepsilon^6) \quad (2.13)$$

$$\bar{u} \sqrt{k/g} = C_0 + \varepsilon^2 C_2 + \varepsilon^4 C_4 + O(\varepsilon^6) \quad (2.14)$$

$$\begin{aligned}
k\eta &= kh + \epsilon \cos k(x - ct) \\
&+ \epsilon^2 B_{22} \cos 2k(x - ct) + \epsilon^3 B_{31} (\cos k(x - ct) - \cos 3k(x - ct)) \\
&+ \epsilon^4 (B_{42} \cos 2k(x - ct) + B_{44} \cos 4k(x - ct)) \\
&+ \epsilon^5 (-(B_{53} + B_{55}) \cos k(x - ct) + B_{53} \cos 3k(x - ct) +) \\
&+ B_{55} \cos 5k(x - ct) + O(\epsilon^6)
\end{aligned} \tag{2.15}$$

where $c=L/T$ and H are known. For cases where L and T are known the theory can be directly applied. Otherwise, it is necessary to specify the current or the mass flux. The A, B and C coefficients and additional ways to find the wave length and the wave period can be found in Fenton's work (Fenton, 1985).

Grue's method (Grue et al., 2003) offers a simple way to predict the wave kinematics in deep waters. For deep water a possible solution to the boundary value problem (Equations 2.4-2.7), using Stokes original parameter ϵ for the expansion, is:

$$\frac{k\phi}{\sqrt{g/k}} = \epsilon e^{ky} \sin(kx - \omega t) + O(\epsilon^4) \tag{2.16}$$

$$\begin{aligned}
k\eta &= \left(1 + \frac{1}{8}\epsilon^2\right) \epsilon \cos(kx - \omega t) + \frac{1}{2}\epsilon^2 \cos 2(kx - \omega t) + \frac{3}{8}\epsilon^3 \cos 3(kx - \\
&\omega t) + O(\epsilon^4)
\end{aligned} \tag{2.17}$$

$$\frac{\omega}{gk} = 1 + \epsilon^2 + O(\epsilon^3) \tag{2.18}$$

and for a wave event the maximum surface displacement is denoted η_c and

$$k\eta_c = \epsilon + \frac{1}{2}\epsilon^2 + \frac{1}{2}\epsilon^3 + O(\epsilon^4) \tag{2.19}$$

The parameter ϵ is found by solving the two equations for frequency dispersion (Equation 2.17) and wave steepness (Equation 2.18)(2.13). In $\omega=2\pi/T$ the time scale T is the local wave period from trough-to-trough for the wave event.

The horizontal velocity is given by:

$$u = \frac{\partial \phi}{\partial x} = \epsilon \sqrt{g/ke^{ky}} \cos(kx - \omega t) \quad (2.20)$$

At crest the horizontal velocity reaches its maximum $u_{\text{crest}} = \epsilon \sqrt{g/ke^{ky}}$. When the velocity is made dimensionless with the reference velocity, the exponential profile $u_{\text{crest}}/u_{\text{ref}} = e^{ky}$ is obtained.

The simplicity of Grue's method comes from the deep water condition, where $kh \gg 1$. When $kh \gg 1$ the coefficients of the second and third-order terms of the velocity potential converge to zero. Looking at the velocity potential the only correction from the first to the third order is in the dispersion relation, where the amplitude is included at third order. For finite depths the solution that satisfies the third-order boundary conditions becomes considerably more complex (Riise, 2009).

2.2 Flow around a cylinder in oscillatory flow

The hydrodynamic quantities describing the flow around a smooth, circular cylinder in steady currents depend on the Reynolds number. In the case where the cylinder is exposed to an oscillatory flow additional dynamics described by the so-called Keulegan-Carpenter number appear. The Keulegan-Carpenter number, KC , is defined by:

$$KC = \frac{U_m T_w}{D} \quad (2.21)$$

in which U_m is the maximum velocity and T_w is the period of the oscillatory flow. If the flow is sinusoidal with velocity given by:

$$U = U_m \sin(\omega t) \quad (2.22)$$

then, the maximum velocity is

$$U = a\omega = \frac{2\pi a}{T_w} \quad (2.23)$$

where a is the amplitude of the motion. For the sinusoidal case the KC number is, therefore, identical to:

$$KC = \frac{2\pi a}{D} \quad (2.24)$$

The angular frequency of the motion that appears in Equation 2.22 relates to the frequency f_w as

$$\omega = 2\pi f_w = \frac{2\pi}{T_w} \quad (2.25)$$

The physical meaning of the KC number can probably be best explained with reference to Equation 2.24. The numerator on the right-hand-side of the equation is proportional to the stroke of the motion, namely $2a$, while the denominator, the diameter of the cylinder D , represents the width of the cylinder (Figure 5). Small KC numbers, thus, mean that the orbital motion of the water particles is small relative to the total width of the cylinder. Stating that, when KC is very small, separation behind the cylinder is expected to not occur.

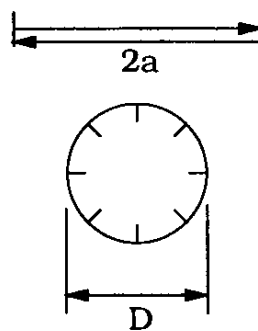


Figure 5. Meaning of the KC number: definition sketch. From Sumer and Fredsøe (2006).

Large KC numbers, on the other hand, mean that the water particles travel quite large distances relative to the total width of the cylinder, resulting in separation and probably vortex shedding. For very large KC numbers ($KC \rightarrow \infty$), it may be expected that the flow for each half period of the motion resembles that experienced in a steady current.

2.2.1 Flow regime and vortex formation

Figure 6 summarizes the most significant changes that occur in the flow around a vertical circular cylinder as the Keulegan-Carpenter number increases from zero. The images are related to the Reynolds number ($Re = 10^3$), which is defined as:

$$Re = \frac{U_m D}{\nu} \quad (2.26)$$

and where ν is the kinematic viscosity of the fluid; for water $\nu = 10^{-6} \text{ m}^2/\text{s}$.

Inspection at the table, from top to bottom, reveals that for very small values of KC no separation of the flow is present (Figure 6a), as expected.


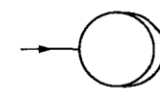
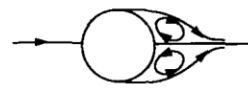
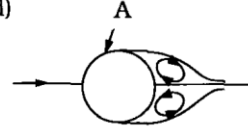
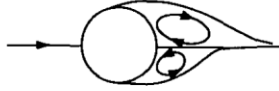
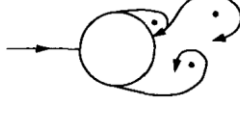
a)		No separation. Creeping (laminar) flow.	$KC < 1.1$
b)		Separation with Honji vortices. See Figs. 3.3 and 3.4	$1.1 < KC < 1.6$
c)		A pair of symmetric vortices	$1.6 < KC < 2.1$
d)		A pair of symmetric vortices. Turbulence over the cylinder surface (A).	$2.1 < KC < 4$
e)		A pair of asymmetric vortices	$4 < KC < 7$
f)		Vortex shedding	$7 < KC$ Shedding regimes

Figure 6. Regimes of flow around a smooth, circular cylinder in an oscillatory flow. $Re = 10^3$. Limits of the KC intervals may change as a function of Re . From Sumer and Fredsøe (2006).

Separation first appears when KC is larger than 1.1 (Figure 6b). This occurs in the form of the so-called Honji instability. Reached this KC condition, the purely two-dimensional flow over the cylinder surface breaks into a three-dimensional flow pattern that exhibits repeatedly, in the cylinder's length direction, pairs of rolls extending along the cylinder circumference. The pattern oscillates in time, appearing and disappearing with a cycle of period being half of the oscillation period. Visualization of these streaks by means of flow-visualization techniques, shows that fluid particles transported by the roll pairs may exhibit a periodic pattern of mushroom-shape vortices (Honji, 1981).

With a further increase of KC , separation occurs in the form of a pair of symmetric, ordinary, attached vortices (Figure 6c,d). This regime covers the KC range $1.6 < KC < 2.6$ while the range $2.1 < KC < 4$ is characterized by the appearance of turbulence over the cylinder (Sarpkaya, 1986), always for $Re=10^3$.

When KC increase even further, the symmetry between the two attached vortices breaks down (Figure 6e). The vortices remain attached to the cylinder, and no shedding occurs. The significance of this regime, prevailing over the range $4 < KC < 7$, is that the lift force is no longer zero and this is caused by the asymmetry in the formation of the attached vortices.

For KC larger than 7, the vortex-shedding regime is established (Figure 6f). In this regime, the vortex shedding onset occurs during each half period of the oscillatory motion. Several such regimes can be distinguished, each of which has a different vortex flow pattern, observed for different ranges of the KC number, as discussed by Williamson (1985).

The transverse-vortex-street regime is known to occur in the range $7 < KC < 13$. A vortex street perpendicular to the flow direction is formed at the lower side of the cylinder. It consists in a pair of vortices, of opposite sign, that are alternatively shed from the side of the cylinder, each forced by the velocity field of the other (mutual induction). The position of the vortex street relative to the cylinder is connected to the direction of the lift force, which must be non-zero in this flow regime. With reference to the KC range $13 < KC < 15$, the wake consists of a series of pairs convected away from the cylinder during each cycle at about 45° to the flow oscillation direction, and on one side of the cylinder only.

The Double-Pair regime occurs in the range $15 < KC < 24$, in which the wake is the result of two vortices being shed at each half cycle. Two trails of vortex pairs move away from the cylinder in opposite directions and from opposite sides of the cylinder. For $24 < KC < 32$,

the wake presents three vortices shed during a half cycle and three vortex pairs are comprised in a cycle. For higher KC regimes, the number of vortex pairs increases by one each time the KC regime is changed to a higher order, in the order of two more vortex sheddings each time a higher order is reached.

With reference to the effect of Re for large KC numbers ($KC > 3$), the available data have been collected by Sumer and Fredsøe (2006) in a graph like that of Figure 7. No extensive data is provided in the literature. Nevertheless, Sumer and Fredsøe matched the extensive data by Sarpkaya (1976) covering a wide range of KC for lower Re regimes along with the data of Figure 7 to interpret what happens also for increasing Re numbers.

With reference to vortex-shedding, the figure shows that the curves begin to bend downward, as Re approaches the value 10^5 . This means that in this region the normalized lift frequency N_L , described as $N_L = f_L / f_w$, where f_L is the fundamental lift frequency and f_w is the frequency of the oscillatory flow, increases with increasing Re . This is consistent with the corresponding result in steady currents, namely that the shedding frequency increases with increasing Re at 3.5×10^5 when the flow is switched from subcritical to supercritical through the critical (lower transition) flow regime.

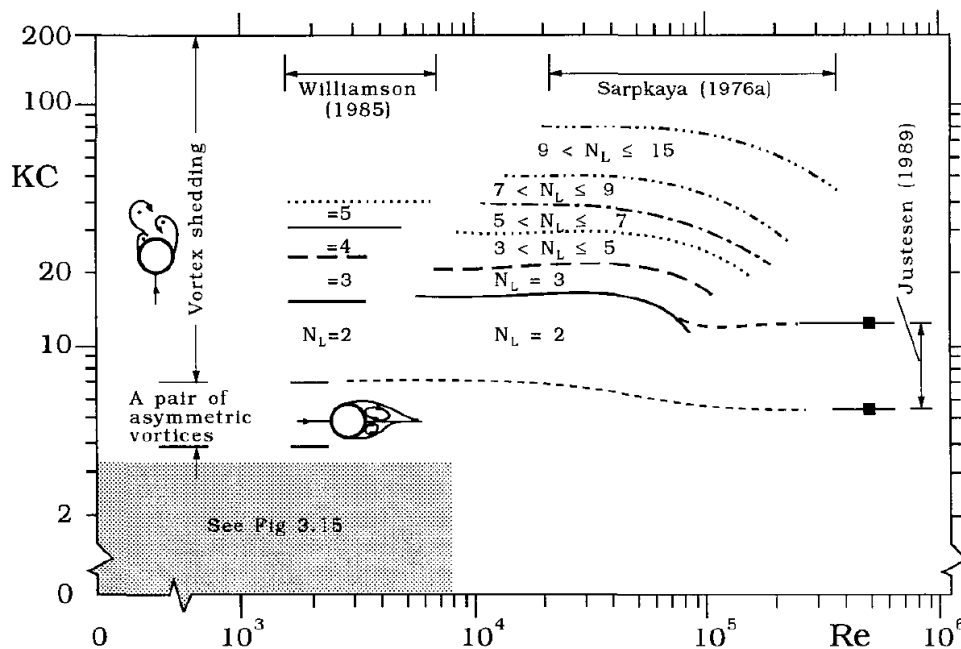


Figure 7. Vortex shedding regimes around a smooth circular cylinder in an oscillator flow. N_L is the number of oscillations in the lift force per flow cycle. From Sumer and Fredsøe (2006).

2.3 Wave loads on vertical slender cylinders

Wave forces on a vertical slender cylinder, i.e. a cylinder with diameter small compared to the water wave length, has proven to be well approximated by the Morison equation (Morison et al., 1950).

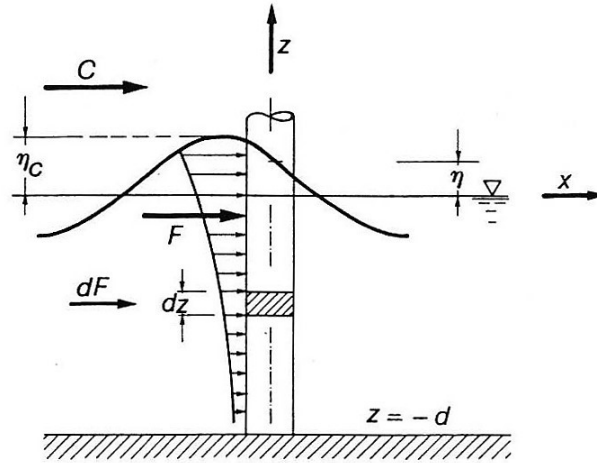


Figure 8. Wave force induced on a slender vertical cylinder: sketch for Morison's formulation. From Matteotti (1995).

The Morison equation assumes the total in-line wave force to be composed by the inertia force (from potential theory and oscillating flow) and the drag forces (from real flows and constant currents) linearly added together (Equation 2.27).

$$\begin{aligned}
 F(t) &= F_{inertia}(t) + F_{drag}(t) = \\
 &= \int_{-d}^{\eta} \frac{1}{2} \rho C_M \frac{\pi D^2}{4} \dot{u}(z) dz + \int_{-d}^{\eta} \frac{1}{2} \rho C_D D u(z) |u(z)| dz
 \end{aligned} \tag{2.27}$$

in which ρ is the water density and D , η and d were already defined in previous sections (see also Figure 8). C_M and C_D are two empirical coefficients, the inertia and the drag coefficient, respectively.

The inertia force, representing the force opposed by the structure against the wave action, depends on the acceleration of the water particles $\dot{u} = du/dt$. Differently, the drag force, representing the drag action exerted by the wave on the cylinder due to the pressure differential created by the wake between the upstream and downstream sides of the cylinder, depends on the square of the water particle velocity, in the direction of wave

propagation. Therefore, the drag and the inertia force components are 90° out of phase with each other over time. It follows that, for small KC values, the inertia component of the in-line force is large compared with the drag component, thus in such cases the drag can be neglected. However, as the number of KC is increased, flow separation begins and the drag force becomes increasingly important.

The original form of the Morison equation is empirical. Over the years, its physical foundations have often been questioned, especially with regard to the dependency on the two empirical coefficient C_M and C_D and to the linear superposition of the two force components, as well as to the validity of neglecting other forces, e.g. the wave run-up, the wave impact (*slamming*), the ringing, and so on.

Since the original Morison's formulation was proposed under the assumption of small-amplitude waves, hence describing a quasi-static force action on a cylinder, such formulation would not be able to represent the load caused by an impulsive breaking event nor loads induced by random seas. While the Morison's equation remains a proper engineering approximation, the wave condition for which this can be applied need to be investigated more in detail. Wave breaking, for example, may induce very high impact forces with extremely short duration on a slender structure, which is not taken into account in the original Morison's formulation.

2.3.1 Wave breaking load

The impact forces generated by breaking waves can attain very large values. Works by Kjeldsen et al.(1986) and Basco and Niedzwecki (1989) showed that plunging wave forces on a pile can be 2-3 times larger than the ordinary forces with waves of comparable amplitudes. A similar multiplicative factor to Morison's original formulation, established to be 2.5, is suggested by SPM 1984 in order to account for the impact force induced by a breaking wave. However, no information about the time history of this force is given.

Under breaking wave attack, the description of the total breaking wave force must also include the additional impact force term F_{impact} , (Wienke et al., 2000), which represents the dynamic component of the acting force not considered before in Equation 2.27.

Therefore, Equation 2.27 changes in:

$$\begin{aligned}
 F(t) &= F_{inertia}(t) + F_{drag}(t) + F_{impact}(t) = \\
 &= \int_{-d}^{\eta} \frac{1}{2} \rho C_M \frac{\pi D^2}{4} \dot{u}(z) dz + \int_{-d}^{\eta} \frac{1}{2} \rho C_D D u(z) |u(z)| dz + \rho \frac{D}{2} C_b^2 C_s \lambda \eta_b
 \end{aligned}
 \tag{2.28}$$

where, relatively to F_{impact} , C_b is the celerity at breaking, C_s is the slamming factor, λ is the curling factor, which indicates how the wave crest is active in inducing a slamming force and it depends on the breaker type and the relative distance between breaking wave point and the structure location, and η_b is the maximum water surface elevation at the breaking point (see also the sketch reported in Figure 9).

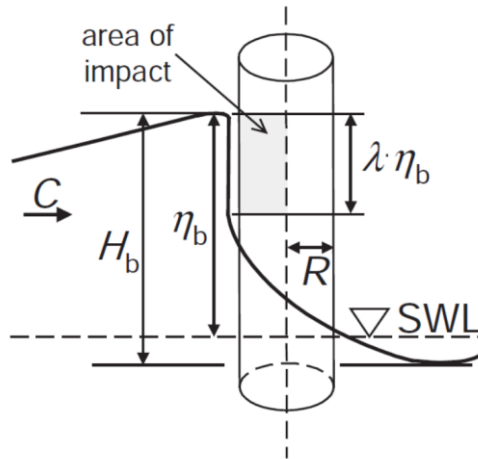


Figure 9. Sketch for the breaking wave impact force.

The analytical formulation for the impact force contribution is derived from calculations by Goda et al. (1966). It is assumed that the breaker front is vertical and moves with the wave celerity C , hitting the cylinder over the height of the impact area $\lambda \eta_b$. The maximum line force on the cylinder is calculated by using Wagner or von Karman's theory, respectively if considering or disregarding the flow besides the flat plate, with which cylinder is approximated (*pile-up effect*). Therefore, the slamming coefficient C_s is determined. Wienke and Oumeraci (2005) found $C_s=2\pi$, thus estimating in

approximately twice the force and a half the duration of the impact with respect to what obtained by Goda et al. (1966). Similar results were obtained also by Sawaragi and Nochino (1984) and Chan et al. (1995).

Many studies over the years have been conducted aimed at improving the knowledge in the topic. As an example, we report, among them, the study by Wienke et al.(2001) on the curling factor determination relying on: i) the breaker type, ii) the classification of the breaking wave loads, iii) the relative distance between breaking point and position of the structure (Tanimoto et al., 1986; Wienke et al., 2000). We, finally, recall the large-scale model tests by Wienke and Oumeraci (2005) from which the three-dimensional force model used to estimate the maximum impact force on a slender cylinder has been recently developed.

2.3.2 Higher-order wave loads

The analysis of wave and corresponding structural responses are of great importance to ocean engineers in the design, and for the operational safety of offshore structures.

When a nonlinear wave, such as a steep wave, passes an offshore structure, the higher-order loads may in certain situations excite the structure as much as its natural frequencies. In an inner domain close to the body surface, in fact, the wave elevation is assumed to be significantly affected even by nonlinearities due to the presence of the structure causing wave diffraction and scattering. These nonlinear loads may induce undesired effects on the structures, such as vibrations.

Potential theory is usually used to investigate these effects, assuming viscous effects to be negligible.

The calculation of the first-order wave effects is regarded as straightforward and the linearized diffraction problem is well predicted by Morison equation, when only the inertia term is retained.

More interest is in the calculation of the higher-order wave effects. For tension leg platforms (TLPs) second-order wave loads have been found to induce resonant axial deflections of the tendons under moderate sea-state. This phenomenon is known as

springing and consists in steady-state oscillations, mainly caused by weakly nonlinear forces at the second harmonic of the wave frequency. Springing loads have been calculated by Chen et al. (1991) and Eatock Taylor and Chau (1992).

Recently, TLPs and monopiles were found to be subjected to a transient resonance condition at their natural frequencies, substantially higher than the governing wave frequency (Faltinsen et al., 1995). This phenomenon involves harmonic wave load components higher than second order and it has become known as *ringing*. Ringing occurs as an axial deflection of the tendons of TLPs, and as a structural deflection in the bending mode for monopiles.

The cause of ringing is not still fully understood. It has been observed that ringing tends to occur when waves are steep and the wave amplitude is of the same order of the radius of the structure. Furthermore, the debate is still open on whether the nonlinear wave kinematics or the nonlinearities arising during wave-structure interaction is the most important factor.

Many different directions have been undertaken to calculate the third-order loads exactly, in order to investigate the ringing in more detail. One approach has been to extend the Morison equation, which gives good estimates for the first-order wave loads in long waves (Madsen, 1986; Rainey, 1989), which was used by Jefferys and Rainey (1994) to predict ringing. Another approach has been presented by Malenica and Molin (1995). They captured the complete third-order velocity potential for a fixed cylinder in finite depth based on the traditional Stokes perturbation method. Later, Faltinsen et al. (1995) presented the FNV theory, based on the long-wave approximation, which has been recently generalized to finite water depth (Kristiansen and Faltinsen, 2017).

The causes of the large higher-order loads have also been investigated experimentally and numerically. On the experimental side, Grue and Huseby (2002) documented that pronounced ringing occurs for the same wave parameters of a secondary load cycle in the wave force signal. This work drove many other experimental studies over the year, aimed at confirming or denying the connection between ringing and secondary load cycle occurrences.

On the numerical side, the more recent work by Paulsen et al., 2014a adds more information on the secondary load origin, but no connection with the ringing has been

found. Again, Kristiansen and Faltinsen (2017) states that the load associated with the run-up, generated by vortical structures arising by flow separation, and the subsequent propagation of steep local waves are the cause of large higher-order loads.

2.3.2.1 Secondary load cycle

Beyond its likely association with ringing, the *secondary load cycle* is a strongly nonlinear phenomenon regarding the wave load on the vertical cylinder. Indeed, Paulsen et al., 2014 found, in their experience, the secondary load cycle to belong to a frequency range above the sixth-harmonic wave frequency.

The secondary load cycle appears as a rapid and high-frequency increase of the excitation force and, occurs after the main peak in the load time-series, at the time of minimum loading (Figure 10, left panel).

The phenomenon was firstly described by Grue et al. (1993) from their experiments. The secondary load can be identified by some own characteristics. For example, it typically occurs about one quarter wave period after the main peak of the excitation force (Grue and Huseby, 2002) and it lasts for about 15% of the wave period (Grue et al., 1993).

Grue and Huseby (2002) further suggested some parameters that are currently used both as tools for the identification of secondary load occurrence and for the investigation of the causes and effects connecting on it. Among them, there are some wave parameters; in particular KC , measuring the flow separation effects, the Froude number Fr , measuring the role of surface gravity waves, the dimensionless wave slope $k\eta_c$ and the wave number kR .

The secondary load cycle has been observed for $KC > 4-5$, $Fr \sim 0.35-0.4$, $k\eta_c > 0.3$ and $kR > 0.1$. The intensity of the secondary load cycle can be estimated by the SLC ratio, defined as $SLC = F_{SLC}/F_{PP}$, i.e. its magnitude over the peak-to-peak force (Figure 10, right panel).

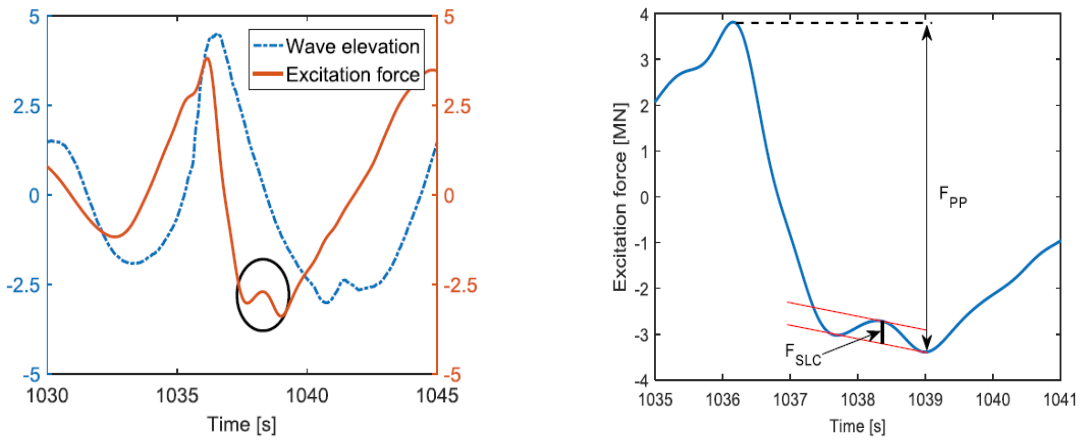


Figure 10. Occurrence of the secondary load cycle, visible on the excitation force (left panel). Estimation of F_{SLC} parameter (right panel). From Suja-Thauvin et al.(2017).

Chapter 3

METHODOLOGY

3.1 Quantitative imaging techniques

Quantitative imaging techniques are a general class of optically-based laboratory measurement techniques, often used to investigate aspects of fluid dynamics (Sveen and Cowen, 2004). These techniques can be utilized to measure the fluid motion close to boundaries and free surfaces, so that they offer new insights in fluid mechanics especially in studying unsteady flows. One of the most important aspects that led to the emerging dominance of quantitative imaging techniques is their capacity to capture whole field properties, e.g. the velocity field, the vorticity field, the Reynolds stress field and the turbulent dissipation field.

These optical measurement techniques can be first divided into two main groups: techniques where a continuous tracer is seeded (e.g., fluorescent dyes) and techniques where the flow is seeded with passive particles. The former ones are generally used to determine a scalar field quantity, while the latter ones are generally employed for the determination of the flow velocity. Particle Image Velocimetry (PIV) and Particle Tracking Velocimetry (PTV) belong to this latter group.

Again, two main descriptions of the fluid motion are possible: the Eulerian and the Lagrangian representations. The Eulerian representation describes flow properties of a fluid at fixed spatial positions. The PIV technique is based on this representation, so velocity fields are generally determined on an interrogation grid and each vector is the average velocity over many tracers contained in a small volume of fluid. Therefore, the

seeding density of the fluid has to be adequate to ensure that all small subregions have several distinct discretely-imaged particles within them and relatively few particle images overlap.

On the other side, the Lagrangian representation is an expansion of single particle kinematic, where the trajectories of single particles are followed. The PTV technique adopts this representation, therefore velocity vectors are determined from individual particle images by a single particle at random locations. To do that, the seeding density of the flow has to be sufficiently low that the velocity can be extracted by tracking the motion of individual non-interfering particles over known times.

Many techniques have been developed starting from PIV and PTV principles, up to the most recently three-dimensional techniques. In this context, the basics of the PIV technique are briefly given, which constituted the method of investigation used in the present study.

3.1.1 Particle Image Velocimetry (PIV)

The experimental setup of a PIV system typically consists of several subsystems. PIV is a pattern-matching technique that calculates velocity fields in fluids, based on an Eulerian representation of the fluid motion. Therefore, the fluid has to be seeded with passive tracers, which are near-neutrally buoyant with respect to the fluid. The particles are illuminated by a light source, generally a laser light source. The laser beam is sent through a slit, such that a 2D light sheet illuminates the particles in the field of interest. In most cases, a digital camera captures images of field of view (FOV), with a Δt time difference between the images. Once a particle has moved of a displacement Δx , from one image to another, the velocity can be indirectly calculated as $u = \Delta x / \Delta t$. In general, computer-controlled timing signals are sent to the digital camera and laser light source to synchronize the light source to the camera such that discrete images of particles with short time exposure, are captured at desired times within each collected image.

The analysis of the flow field by PIV images starts from a pairs of consecutive collected raw images. Each image is divided into interrogation subwindows of dimension in size depending on image resolution and fluid velocity. As a general rule, the size of the

subwindows must be large enough, so that at least 4 to 5 particles are contained in each one, and it must also cover the largest particle displacement possible.

On each subwindow, a difference algorithm is applied to calculate a correlation peak between two consecutive images. The most common method to find the displacement of a particle in time is the cross-correlation analysis (see, Figure 11, top panel). The cross-correlation function is given by:

$$R(s, t) = \frac{1}{N^2} \sum_{i=0}^{N-1} \sum_{j=0}^{N-1} \{F'_{i,j}(i, j)\} \{F''_{i,j}(i + s, j + t)\} \quad (3.1)$$

where N is the width and height of the picture in pixels, $F'_{i,j}$ is the (i, j) subwindow of the first image and $F''_{i,j}$ is the corresponding subwindow from the second image. The indices (i, j) correspond to a pixel location, (r, s) correspond to a sought displacement, and $R(s, t)$ is the cross correlation plane.

The cross-correlation function can also be computed in the spectral domain, making use of \mathcal{F} and \mathcal{F}^{-1} which denote Fourier and inverse Fourier transform:

$$R(s, t) = \mathcal{F}^{-1}[\mathcal{F}^*\{F'_{i,j}(i, j)\} \mathcal{F}\{F''_{i,j}(i + s, j + t)\}] \quad (3.2)$$

where a star denotes the complex conjugate.

The location difference between the centre of the correlation plane and the highest correlation peak found is the largest obtained displacement.

If the actual displacement x is larger than $N/2$ pixels, the correlation peak will alias to the location $-(N-x)$. If the displacement is larger than N pixels, no particles from the first subwindow can be detected in the second subwindow, and the correlation peak in the correlation plane will represent a random correlation of two uncorrelated subwindows.

The correlation plane (Figure 11, bottom panel) can be separated into three layers (Adrian, 1988): the correlation of the mean background intensities $R_b(s, t)$, the correlation between mean and fluctuating intensities $R_f(s, t)$, and the correlation between the fluctuating intensities $R_d(s, t)$. The last one contains the actual displacement peak, and can be found by calculating a normalized correlation given by:

$$R(s, t) = \frac{1}{N^2} \frac{\sum_i \sum_j [F'(i, j) - \bar{F}'] [F''(i + s, j + t) - \bar{F}'']}{\sum_i \sum_j ([F'(i, j) - \bar{F}']^2 [F''(i + s, j + t) - \bar{F}'']^2)^{1/2}} \quad (3.3)$$

where \bar{F}' and \bar{F}'' are the means of $F'(i, j)$ and $F''(i + s, j + t)$, respectively. The range of $R(s, t)$ is 0 to 1, where 1 indicates strong correlation between subwindow F' and F'' .

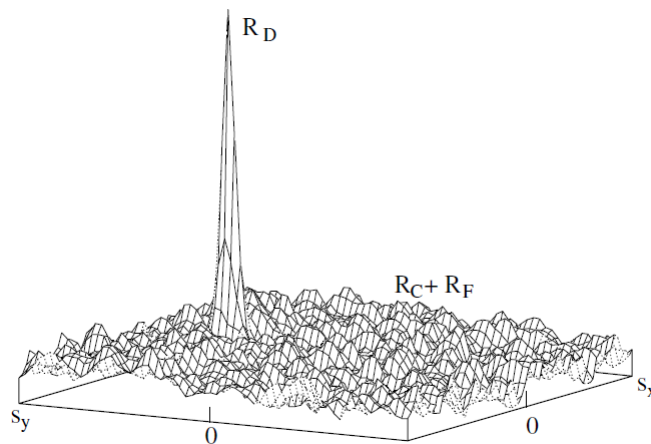
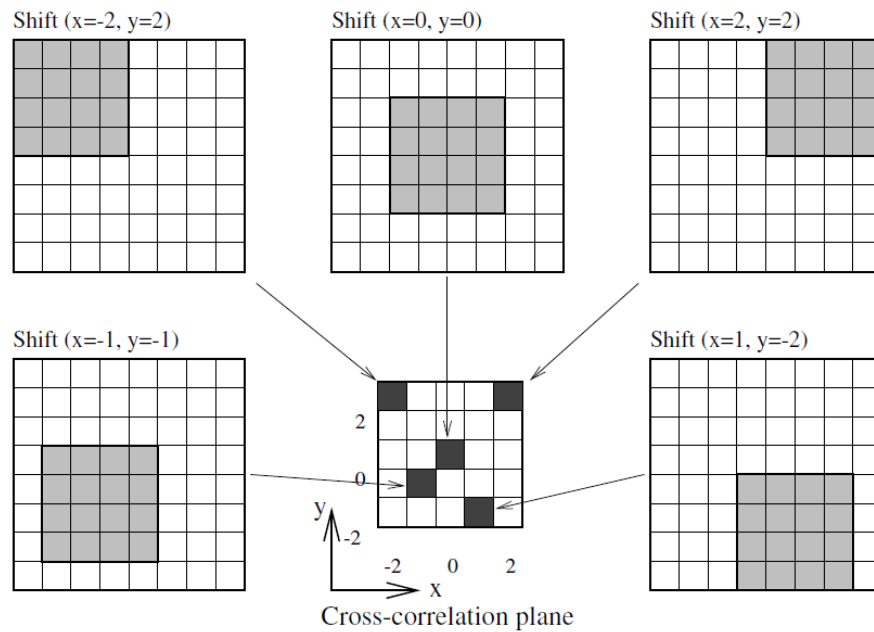


Figure 11. Cross-correlation. *Top panel*: Example of the formation of the correlation plane by direct cross-correlation: here a 4×4 pixel template is correlated with a larger 8×8 pixel sample to produce a 5×5 pixel correlation plane. *Bottom panel*: Composition of peaks in the cross-correlation function. From Raffel et al. (1998).

To be able to find the exact location of the centre of a particle, the particle has to cover at least 2-4 pixels. The exposure time of the camera must also be set such that the particle centre can be determined by looking at the intensity of each pixel the particle covers. It is desirable that the centre pixels have higher intensity than the pixels on the boundaries of particles.

One problem with this method is peak-locking, a bias error for which the displacement of a particle always is locked to whole pixels. For example, if the actual displacement is 3.4 pixels, the displacement will be locked to 3 pixels, which gives an error of 11%. Peak-locking can be solved by using curve fitting on the displacement peak and the neighbouring peaks, to estimate an exact displacement. Gaussian peak fit is often used and is a good approximation for spherical particles (Sveen and Cowen, 2004). Another way to solve peak-locking is to dynamically shift the subwindows so the sub-pixel displacement converges to zero.

In conclusion, each subwindow pair generates one velocity vector. To validate the vectors, two criteria must be fulfilled: good signal quality and smoothness in both time and space. Vectors can be filtered by setting a threshold on the signal to noise ratio (SNR). This is the ratio between the highest correlation peak to the second highest peak in the correlation plane, where the threshold is often set in the range of 1.2-1.5 (Raffel et al., 1998).

Local and global filters are often applied. Global mean filters compare a vector to the mean of all the vectors collected in an image pair. Local filters compare a vector to its surrounding vectors. The median is often used, as outliers affect the mean dramatically.

Finally, the velocity field resulting from the analysis of all the subwindows in the pair of images, following the above described procedure, has to be reported in world coordinates. In order to do a transformation from pixels into world coordinates, a picture of a coordinate system in the correct focal plane has to be captured, where the spacing between the dots or crosses on it are known, in order to establish the coordinate transform function.

Many and increasingly higher performant softwares and codes dedicated to PIV data analysis were developed over the last decades, driven by computer and image capture technologies progresses. Among these softwares are the techniques, algorithm and

statistics element reported above working on digital images, making the analysis faster and even more accurate.

3.2 Wave focusing technique

Wave breaking in deep water can be simulated in the laboratory by studying the impact of individual steep waves on some model of the real offshore structure. In order to achieve these extreme loads onto a body of interest the individual wave of large steepness has to be generated right in front of the body (a cylinder in this case).

The waves of interest for our analyses, mostly breaking, have been reproduced by means of the frequency-focusing technique. It is based on use of the dispersive nature of surface gravity waves, which makes it possible to focus individual wave components of a wave train to produce a single large wave at the desired time and spatial location. This approach is also called *wave focusing*.

Chaplin (1996) have been identified and discussed three methods, namely: the phase speed method, the reverse dispersion method and the group celerity method.

The *phase speed method* is based on the properties of wave trains of different frequencies to travel at different speeds. This method has been discussed and implemented by Baldock et al. (1996). The linear dispersion relation implies that the waves of higher period have higher group velocity than the waves of smaller period. A large single wave can be created if several wave trains all come to a common phase at some a given point away from the wavemaker. Periodic wave components in the input signal are at discrete frequencies. It means that the n^{th} component has a wave number $k_n = \frac{2\pi}{L_n}$ and a frequency $\omega_n = \frac{2\pi}{T_n}$, where L_n and T_n are the wavelength and the period respectively. It is assumed that focusing occurs at the focal point $x_f = 0$, thus the surface elevation of the wave at the focal location is given by:

$$\eta(x_p, t) = \sum_{n=1}^N a_n \cos(\omega_n t_f) \quad (3.4)$$

where N is the total number of wave components and a_n is the amplitude of the n^{th} component. It means, that all wave components are in phase and are focused at $t_f = 0$. If the location of the wavemaker is $x = x_p$, the following equation for the surface elevation at the wave board implies:

$$\eta(x_p, t) = \sum_{n=1}^N a_n \cos(\omega_n t - k_n x_p) \quad (3.5)$$

This equation is then used to generate a numerical input signal for the wavemaker.

With the aim to control the relation between this signal and the wave elevation at the focal position, Baldock has introduced a first-order transfer function under the assumption that no higher-order harmonics is produced by the motion of the wave paddle (Hemming, 1996). The transfer function was determined experimentally and was documented to be very stable and to produce a very small error.

The *reverse dispersion method* assumes that the surface elevation of the wave, taken at a certain location, can be used in order to derive the input signal for the wave paddle (Mansard and Funke, 1982). Under the assumption that the linear dispersion relation represents a valid approximation to calculate frequency components in wave trains, the wave train calculated or measured at the desired spatial location is hindcasted in terms of its Fourier transform at the wave board. The inverse Fourier transform of the hindcasted data can then be used to derive a time series for the wavemaker input.

The *group celerity method* is based on the assumption that the speed of energy propagation is related to the group velocity of the waves leaving the wavemaker. Thus, given the dispersive nature of gravity waves, energy can be concentrated at the required location in the wave flume. This can be achieved if the numerical input signal for the wavemaker has a linearly decreasing frequency.

All the methods described are based on the linear wave theory, thus provide certain limitations. Accuracy, convergence and overall reliability of iterative focussing techniques is difficult to obtain and reduce considerably with increasing nonlinearity of the wave, which is normally represented by its steepness. Hence, empirical investigation of these

techniques is very important, therefore precursor studies are represented by Longuet-Higgins (1988) and Melville and Rapp (1988) on the generation in laboratory of different types of breakers, from which followed Su et al. (1982), Rapp and Melville (1990), Griffin et al. (1996) and Perlin et al. (2013), just to name a few.

The large development of computational fluid dynamics models in the last decades makes it possible to investigate the breaking onset process in the more controlled environment of a numerical wave flume. Many studies were conducted reproducing the input wave by means of the focusing technique, with the further purpose of validating CFD programmes; as for examples Babanin et al. (2010), Chella et al. (2016) and Paulsen et al., 2014a.

3.2.1 Wave focusing generation in the wave flume

Focusing waves at the wave flume of the Hydrodynamics Laboratory of the University of Oslo, where the experimental campaign of this study was conducted, are generated by using the group celerity method. The implementation of this technique for generating the input signal for the wave board was provided by Osyka (2016).

The same approach was also used in Brown and Jensen (2001), in which the authors investigated the limitations of the linear theory by comparing the surface elevation predicted by the linear theory and the measured surface elevation of the gravity wave at the focal location.

The input signal for the wavemaker is given by the following function:

$$V(t) = b(t) \sin(\phi(t)) \quad (3.6)$$

where $\phi(t)$ is a phase function which is given by.

$$\phi(t) = 2\pi f_0 t \left(1 - \alpha \frac{t}{t_s}\right) \quad (3.7)$$

$$0 \leq t \leq t_s$$

in which t_s is the time the wave paddle stops.

After testing the input signals with different parameters, Osyka (2016) observed that generation of the breaking wave at the focal point was much easier to achieve by setting $b(t)$ as constant in Equation 3.3. The choice of a variable amplitude, given by Equation 3.5, resulted most often in a steep, non-breaking wave at the focus point.

$$b(t) = \frac{256V_0}{27t_s^4} t^3(t_s - t) \quad (3.8)$$

From the equation above, it is straightforward to verify that for deep-water conditions perfect focus is produced at:

$$x_f = \frac{gt_s}{8\pi\alpha f_0} \quad (3.9)$$

The group celerity method and basically all methods for wave focusing are founded on the linear dispersion theory, which states that individual components of wave train all propagate at their own phase velocities. In turn, phase velocity is a function of both water depth and wave period. Therefore for deep and intermediate water conditions the high frequency waves propagate slower than low frequency waves, which actually enables focusing at the desired position by in phase wave component superposition.

However, the frequency-focusing technique neglects the nonlinearities of the wave components and their interaction, as well as nonlinearities in the motion of the paddle. Therefore, small changes to the numerical input signal may result in unpredictable events, as shown by and Chaplin et al. (1997) . As a result, the actual focal point x_f is somewhat different from what is predicted by Equation 3.4.

To achieve focusing of the wave crest at the desired position, which is assumed to be just in front of the cylinder, different series of focusing waves have been implemented. In detail, Osyka (2016) describes the general procedure for the determination of a good crest focusing at the cylinder is made of: (1) the generation and execution of the numerical input signal for the paddle identifying the wave event; (2) the observation and estimation of the difference between the theoretical focal point and the real one; (3) the rewriting of the input signal by varying the parameters in Equation 3.4, improving the sampling rate of the data acquisition; (4) the verification of the occurrence of focusing at the desired position

and, finally, (5) the subsequent variation of the amplitude of the signal V_0 , paying attention that no-breaking ahead the focal point occurs.

The experimental implementation of the approach and the code for generation of input signals can be found in Osyka (2016).

3.3 Vortices and Coherent Structures

Any form of spatially coherent and temporally evolving vortical motions dominating a turbulent shear flow can be referred to as a coherent structure (Jeong and Hussain, 1995). This means that a portion of the fluid, identified as a coherent structure, remains roughly together while moving in the fluid.

Frequently, coherent structures in turbulent flows are regarded as vortices, due to the that vortices lack a strict definition.

For instance, Lugt (1979) defined a vortex as a “*multitude of material particles rotating around a common centre*”. According to Chong et al. (1990), a vortex is “*a region of complex eigenvalues of the velocity gradient tensor*”, while Hunt et al. (1988) identify a vortex as a region containing both positive second invariant of the velocity gradient tensor and low pressure.

It is broadly agreed that vortices are concentrated in regions of high vorticity and that they are viewed as evolving domains with a high degree of material invariance. It is indeed intuitive to associate a vortex with the presence of some form of particle rotation around a common coreline that describes closed or spiralling streamlines, as well as with the pressure minimum, so identifying the vortex core. Also, the concept of high vorticity magnitude can be easily associated with the presence of a vortex.

However, the criteria to be used to evaluate the extension of a vortex from its centre of rotation is still on debate in the scientific community. Furthermore, interaction between structures may complicate the evaluation.

Starting from the above-mentioned indicators, i.e. closed or spiralling streamlines and pathlines, pressure minimum and vorticity magnitude, many attempts were conducted to provide a criterion for an objective identification and definition of a vortex.

From the two different Galilean-invariant definitions of a vortex using invariants of the velocity gradient tensor proposed by Chong et al. (1990) and Hunt et al. (1988), several criteria were developed and are described in the following. More recently, approaches based on seeking vortex boundaries as maximal material tubes were provided by Farazmand and Haller (2015) and Haller et al. (2016). Recently, Haller et al. (2016) proposed an approach based on the decomposition of the deformation gradient into a purely straining flow and a purely rotational flow.

3.3.1 Vortex identification criteria

A brief summary of the main vortex identification criteria is provided by Holmèn (2012) and this treatise is reported for need of clarity.

Some methods are available in the literature on identification of vortex, which are based on the velocity gradient tensor. The velocity gradient tensor \bar{D} can be written as $D_{ij} = \partial u_i / \partial x_j$, decomposed into a symmetric and a skew-symmetric part:

$$D_{ij} = S_{ij} + \Omega_{ij} \quad (3.10)$$

where $S_{ij} = \frac{1}{2} \left(\frac{\partial u_i}{\partial x_j} + \frac{\partial u_j}{\partial x_i} \right)$ is the rate-of-strain tensor, and $\Omega_{ij} = \frac{1}{2} \left(\frac{\partial u_i}{\partial x_j} - \frac{\partial u_j}{\partial x_i} \right)$ is the vorticity tensor. The characteristic equation for \bar{D} is given by

$$\lambda^3 + P\lambda^2 + Q\lambda + R = 0 \quad (3.11)$$

where P , Q and R are the three invariants of the velocity gradient tensor, which decomposed into symmetric and anti-symmetric parts can be expressed as follows.

$$\begin{aligned}
P &= -tr(\bar{D}) \\
Q &= \frac{1}{2}(tr(\bar{D})^2 - tr(\bar{D}^2)) = \frac{1}{2}[|\Omega|^2 - |S|^2] \\
R &= -det(\bar{D})
\end{aligned} \tag{3.12}$$

Hunt et al. (1988) elaborated the *Q-criterion*, based on Equation 3.10, which defines a vortex as a special region where $Q > 0$. This criterion requires that the pressure be lower than the ambient pressure in the vortex. Q represents the local balance between the shear strain rate and the vorticity magnitude, defining vortices as areas where the vorticity magnitude is larger than the magnitude of the rate-of-strain.

For two-dimensional flows, this criterion has been known as the *Okubo-Weiss* criterion, derived by Okubo (1970) and Weiss (1991). Later, Hua and Klein (1998) provided a correction to the Okubo-Weiss criterion by including acceleration terms.

Δ -*criterion* of Chong et al. (1990) considers vortices as regions where the eigenvalues of the velocity gradient tensor are complex and the streamline pattern is spiralling or closed. This definition is valid for incompressible flows where $P = 0$. The streamlines are closed or spiralling if two of the eigenvalues form a complex conjugate pairs where the discriminant of the characteristic equation is:

$$\Delta = \left(\frac{Q}{3}\right)^3 + \left(\frac{R}{2}\right)^2 > 0 \tag{3.13}$$

The λ_2 -*criterion* of Jeong and Hussain (1995) looks for a pressure minimum but removes the effects of unsteady straining and viscosity by discarding these terms. Therefore, only $S^2 + \Omega^2$ is used to determine if there is a local pressure minimum that entails a vortex. The criterion requires that:

$$\lambda_2(S^2 + \Omega^2) < 0 \tag{3.14}$$

The *Swirling Strength Criterion* uses the imaginary part of the complex eigenvalues of the velocity gradient tensor to visualise vortices. It is based on the idea that the velocity gradient tensor in Cartesian coordinates can be decomposed as:

$$\bar{D} = [\bar{v}_r \quad \bar{v}_{cr} \quad \bar{v}_{ci}] \begin{bmatrix} \lambda_r & 0 & 0 \\ 0 & \lambda_{cr} & \lambda_{ci} \\ 0 & -\lambda_{ci} & \lambda_{cr} \end{bmatrix} [\bar{v}_r \quad \bar{v}_{cr} \quad \bar{v}_{ci}]^T \quad (3.15)$$

where λ_r is the real eigenvalue with corresponding eigenvector \bar{v}_r and the complex conjugate pair of complex eigenvalues is $\lambda_{cr} \pm i\lambda_{ci}$ with corresponding eigenvectors $\bar{v}_{cr} \pm i\bar{v}_{ci}$. By expressing the local streamlines in a coordinate system spanned by the three vectors $(\bar{v}_r \quad \bar{v}_{cr} \quad \bar{v}_{ci})$, the local flow is either stretched or compressed along the \bar{v}_r axis, while on the plane spanned by the vectors \bar{v}_{cr} and \bar{v}_{ci} , the flow is swirling. The strength of this swirling motion can be quantified by λ_{ci} , called the *local swirling strength* of the vortex. The criterion is therefore $\lambda_{ci} \geq \varepsilon > 0$ (Zhou et al., 1999).

Finally, definition of *vorticity* is also given. Vorticity is defined as the curl of the velocity, $\omega = \nabla \times U$ and it is equal to twice the rotation of the fluid at (x, t) . Thus, the vorticity can be used directly to identify vortices, but it cannot distinguish between swirling motions and shearing motions.

Vorticity can be readily visualised by plotting isosurfaces of $|\omega|$. This can be problematic since different thresholds can result in different geometrical structures. Vorticity is a vector field and therefore has integral curves obtained by solving

$$\frac{dx}{ds} = \frac{\omega}{|\omega|} \quad (3.16)$$

where s is the distance along the vortex line. In order to get useful results using this method, the choice of the starting point is very important. The structures have to be visualised have to be identified before drawing the lines. This represents a method to visualise vortices, not to identify them.

Chapter 4

LABORATORY EXPERIMENTS

4.1 The wave flume

The experiments were performed in the medium-size wave flume of the Hydrodynamics Laboratory, Department of Mathematics, at the University of Oslo (Norway).

The wave flume, having a length of 25 m and a width of 0.5 m (Figure 12), is characterized by glassed sidewalls and bottom, this allowing to carry out optical measurements. At one end of the wave tank, an hydraulic piston-type wavemaker, with movements controlled by pre-set voltage time series based on linear wavemaker theory, is located (Figure 12, top right panel). At the opposite end, a passive absorbing beach (Figure 12, bottom right panel) damps the wave reflection down to 3% of the amplitude of the incoming wave (see, Brown and Jensen, 2001; Grue et al., 2003).

4.2 Experimental overview

The experiments have been undertaken with the aim to investigate the hydrodynamics around a slender vertical cylinder forced by steep waves. Several measurements were recorded, in order to collect a comprehensive amount of information to cover several dynamics of interest.

For this purpose, two setup configurations of the physical model were built.

The first configuration (Setup1) was aimed at the investigation of the vertical velocity field near the crest of the incoming wave approaching the cylinder. Particle Image Velocimetry

(PIV) was used by collecting images of a 15×10 cm field of view of the seeded flow close to the wave crest. At the same time, pressure measurements on the upstream side of the cylinder were recorded.

The main focus of the experimental campaign was the visualization of the flow on the downstream side of the cylinder, on horizontal sheets at different vertical positions. The interest was in detecting the flow separation and the formation of vortical structures. This has been carried out building a second setup (Setup2) of the physical model. Also for these experiments PIV was used to obtain images of a 10×10 cm FOV of the seeded flow attached to the backside of the cylinder.

For both configurations the water surface was monitored by wave gauges along the flume, with particular attention to the area close to the cylinder. Force measurements, synchronized with the signals collected by all the other instruments, were carried out.

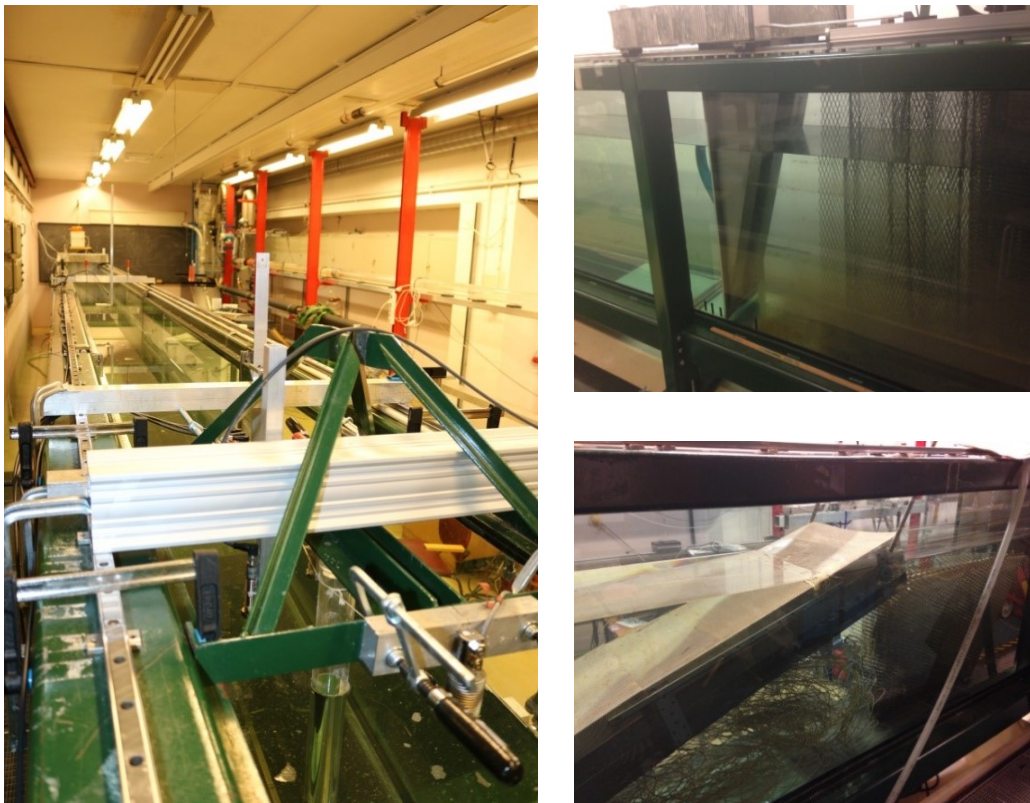


Figure 12. The medium-size wave flume of the Hydrodynamics Laboratory (left panel). Details of the wavemaker (top right panel) and of the absorbed beach (bottom right panel).

4.2.1 Physical model

The experimental setup was based on Osyka (2016) and it is the same one also reported by (Riise et al., 2018a, 2018b).

The physical model was built at a distance of 10.90 m from the wavemaker in order to preserve undisturbed flow conditions in the measurement area.

The model (sketched in Figure 13) consists in a clear acrylic vertical circular surface-piercing cylinder with a diameter $D=0.06$ m, installed on the centreline of the tank and pivoted at the bottom by a low friction hinge.

On the top the cylinder was fixed and rigidly connected by pre-tensed ropes to a system of load cells for the measurement of the force acting on it. The bearing point of the cylinder was at 2 cm above the tank bottom, so some disturbances at the bottom were possible. However, the specific configuration of the hinge was designed to allow for the rotation of the cylinder around its vertical axis and, furthermore, to easily replace the cylinders without removing the hinge when the setup configuration had to be changed.

The tank was filled with a constant water depth of 0.72 m for both the configurations, to guarantee that waves would propagate in deep waters conditions.

During the experiments, the measurement of the incident wave elevation and the evaluation of the type of breaker were provided by four wave gauges. Two of them (WG1 and WG2) were placed to monitor the wave surface, respectively at 9m and 15m from the wave paddle. WG3 and WG4, respectively located at 0.06 m upstream the cylinder and at 0.11 m laterally to the cylinder, were used to detect the incoming wave at the cylinder and thus to obtain information on impact of the waves onto the cylinder, in terms of breaking point location and breaker type.

The high accuracy of the instrumentations was underlined also by Riise et al. (2018a), which reports an error lower than 0.01 Nm for the load cells and lower than 1 mm for the wave probes.

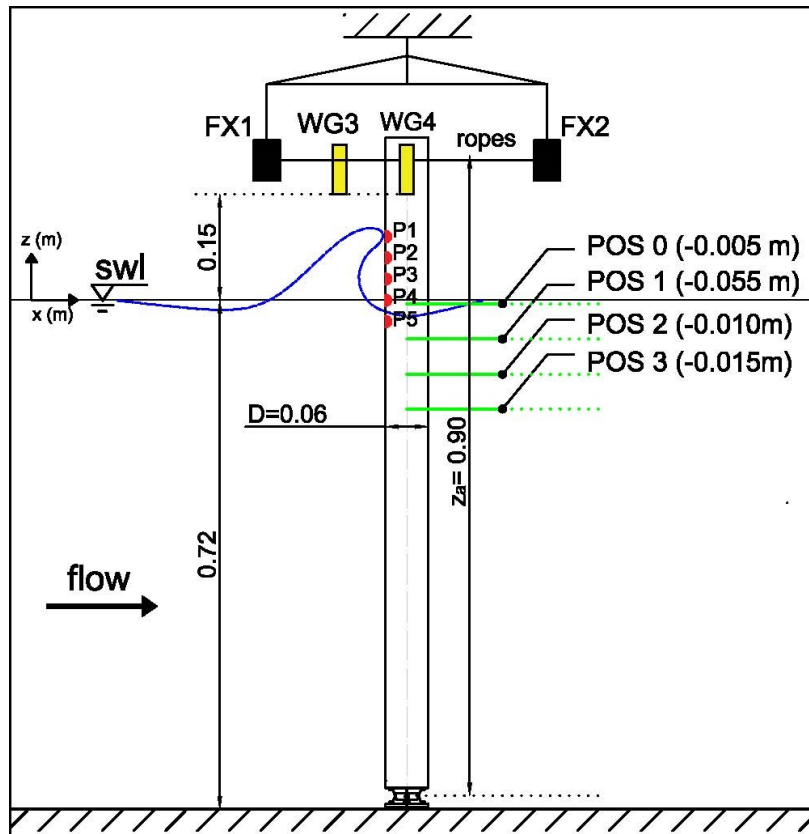


Figure 13. Global sketch of the experimental setups. The cylinder reports all instruments in use: wave gauges close to the cylinder (WG3, WG4, in yellow) and force measurements system (FX1, FX2, in black) common to both configurations; pressure transducers (P1-P5, red dots) relative to Setup1 and horizontal sheets (POS0-POS4, green lines) relative to Setup2. Dimensions are expressed in m.

4.2.2 Instrumentation

A general overview of the instruments is herein described, in terms of their functioning and employment during the experimental campaign.

4.2.2.1 Wave surface elevation measurements

The *UltraLab ULS Advanced Ultrasound* system was used to keep track of the water level and to measure and record the surface elevation of the incoming waves. The system includes the following devices:

- USS02/HFP, IP 65, M18×1.0, advanced gauges (Figure 14, left panel);

- 1 ultrasound sensor of the type REF-300 for precise sound velocity measurements;
- 1 Ultralab Advanced controller (Figure 14, right panel);
- a computer with installed Ultralab software interface to manage the signal measurements.

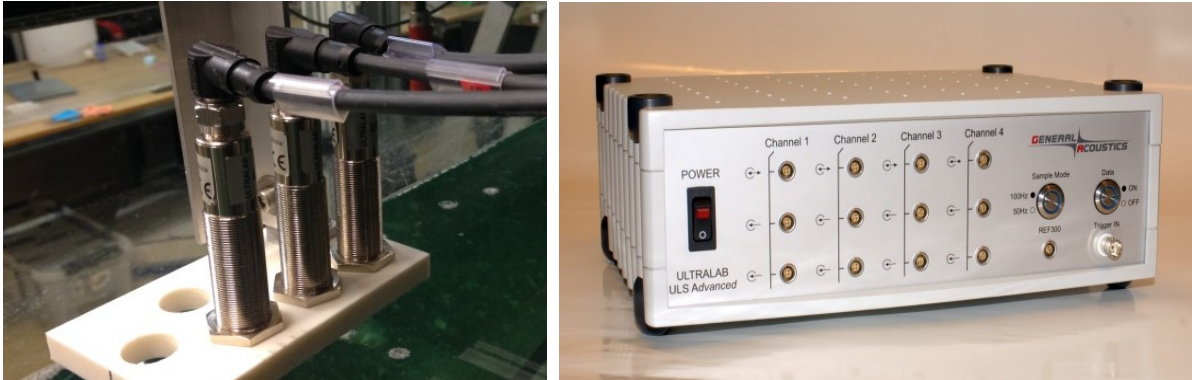


Figure 14. Acoustic wave gauges system for measurements of the water level. Left panel: in-line arrangement of acoustic wave gauge. Right panel: acquisition controller box.

Ultralab gauges have a measuring range from 30 mm up to 250 mm and technical resolution of 0.18 mm. The software enables the visualization and the recording of the data in real time. It is possible to choose between two sampling frequencies: at 125 Hz (low frequency) and at 250 Hz (high frequency).

The main advantage with this measuring system is that one can use several gauges to measure the elevation at one single place. As an example, an in-line setup of three sensors could be chosen for the wave measurement near the cylinder. The transmitting sensor was placed in front of the incoming wave, closer to the wavemaker, whereas the two others were placed behind the transmitting sensors. The signal reflected from the surface was received by all sensors, which enabled both high resolution and precision of the measured elevation. This was particularly useful when the elevation of steep and fast moving waves had to be measured.

4.2.2.2 Force measurements

The general purpose of measuring the total moment of the cylinder forced by waves was pursued.

On the top, at a distance of $z_a=0.90$ m from the bearing, the cylinder, was kept in an equilibrium condition by a symmetrical system of pre-tensed ropes that connected it to the load cell system. Two unidirectional load cells (namely FX1 and FX2), arranged in-line, one upstream and the other one downstream at the same distance from the cylinder, measured the force from which the wave-exciting moment was determined. The system is reported in Figure 15 (left panel).

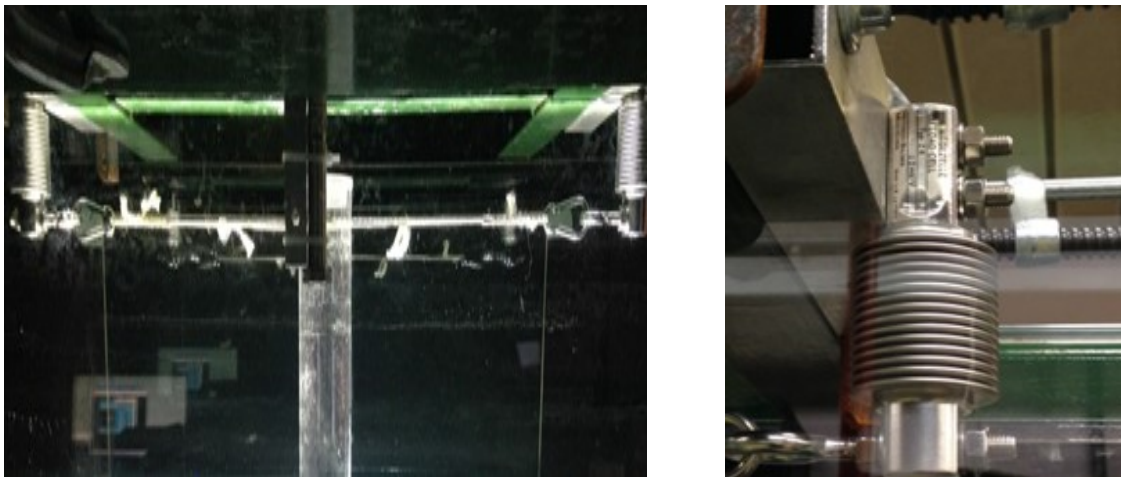


Figure 15. Force measurement system arrangement. Left panel: general view. Right panel: detail of load cell.

Hottinger Baldwin Messtechnik Z6C2 load cells (Figure 15, right panel) were used to record the force on the cylinder. The experimental setup was designed to measure the total moment of the cylinder above the bottom. Thus, the measured force from the transducers has to be multiplied by the arm z_a (the distance from the mounting point to the measuring point).

It is also assumed that for this hinge set-up both top attachment (rope) and bottom attachments (bearing) are moment-free and, therefore, do not contribute to the total moment.

As previously mentioned, the bending beam load cell is the primary weighing component. It is extremely accurate and according to the technical specification has an accuracy class of OIML R60 (more information available in the HBM datasheet (HBM website, 2018)).

The approach at the basis of the transducers functioning relies on the Wheatstone bridge. When a force is transferred to the sensor, one of the resistors in the bridge gets bent, which leads to a change in its resistance. This causes a change in the potential of the electrical

circuit. The change in the resistance is further sent through the amplifier to a data acquisition system (DAQ). The *Catman Easy* software enables one to visualize and record the measured force. The software must be configured by specifying both properties and parameters of the force transducers. After a correct configuration is made, the data can be visualized and recorded. The possible sampling frequency of the data acquisition reaches 9600 Hz and the maximum load on the beam is ~100 N.

4.2.2.3 Pressure measurements

Kulite XTL-190 M sensors (Figure 16) were installed on the cylinder used for Setup1. These are miniature ruggedized pressure transducer and were particularly suitable in view of the need to insert them into a cylinder of very small diameter (6 cm). Their length is of 3.5 cm, for a total length of 4.5 cm, if considering also the space occupied for the cable curvature, and the region that senses the pressure on the cylinder surface is circular with diameter of 0.5cm.



Figure 16. Miniaturized pressure transducer.

Two different ranges of measurement were chosen. Pressure transducers with maximum pressure of 3.5 bar (50 Psi) were selected for the measurements at the upper levels, in correspondence of the wave crest (P1-P3 in Figure 13). At these elevations, the pressures are expected to be the largest possible due to the impulsivity of the breaking event or the impact of the steep wave front and the role of the air entrapment. Differently, sensors with top pressure of 0.7 bar (10 Psi) was chosen for measurements at the lower elevations (P4-P5 in Figure 13).

Differential operational mode pressure transducers have been preferred because of their high accuracy in measurement. A high precision is guaranteed by the manufacturer, reporting a tolerance of $\pm 0.1\%$ FSO BFSL (Typical), $\pm 0.5\%$ FSO (Maximum); more details available in the Kulite XTL-190 datasheet (Kulite website, 2018).

4.2.2.4 PIV arrangements

A general PIV arrangement is constituted by an illuminating source, a fast camera and tracers with which the water flow is seeded.

Two different PIV systems were used in this experimental campaign, different for: i) the investigation of the flow on the centreline vertical plane upstream the cylinder and ii) the flow on horizontal sheets at the lee side of the cylinder.

For Setup1, the PIV system was composed by a LED light in-line illuminator device, a CCD camera running at 100 Hz. Differently, for Setup2, the PIV system was constituted by a laser source and a CCD fast camera at 1000 Hz. Synchronizer systems have been built for timing the instruments accordingly to the need of each setup.

In the following, a description of the characteristics of the all instrumentation used and their operative mode is provided.

Illumination devices

For Setup1, the *VLX LED Line* lightning delivered by *Gardasoft Vision* with maximum intensity of 2.3×10^6 Lux was used as light source. The intensity of the lamp is in the range 0% to 140% equals to the maximum intensity of the light source. The *Tera Term* software was used to control the intensity, i.e. by sending simple commands through the Tera Term terminal, the intensity of the LED source was adjusted. These high values of light intensity were made possible thanks to a liquid cooler system of the lamp.

Differently, for Setup2, a Nd:YLF pulsed laser source (*Quantronix Darwin Duo* 15mJ@3000 Hz) was employed. The need was to create a light sheet as thin and homogenous as possible, to avoid disturbances due to bubbles, light reflections, and others, from the neighbouring planes.

While in the case of the LED lamp, the light sheet was directly obtained by the in-line arrangement of the LED light, for the laser: the beam was deviated to reach the desired position by means mirrors, and then it was spread into a light sheet through the passage inside an optics.



Figure 17. Light sources: LED line (left panel) and laser (right panel).

Cameras

In view of the impulsive nature of the phenomenon, fast CCD cameras were used to capture images of the field of view of the interest at high frame rates.

The *DALSA Teledyne Falcon2 4M* (Figure 18, left panel) was used for image sampling and visualization of the extreme wave events collected during the experiments of Setup1. This camera worked with acquisition frame rate up to 168 fps at the megapixel resolution of 2432×1728 ; more information available at the DALSA Teledyne Falcon2 4m datasheet, (Teledyne Dalsa website, 2018).

The camera setting was made using the *Sapera Cam Expert* software suite through which framerate, exposure time, gain and image format could be established. The software was also able to control the image acquisition with respect to an external trigger.

The *Stream Pix* software was used to define the image acquisition plan, i.e. recording rate and the stop conditions, which could be set either at the reaching of a number of acquired frame or at a pre-set past time.

A high-speed CCD camera, *Photron FASTCAM SA5 1000K-M2* (Figure 18, right panel) acquired images for experiments of Setup2. The camera provided with up to 7500 fps at a maximum resolution of 1024×1024 Megapixel (more details available at the FASTCAM SA5 Datasheet (Photron website, 2018).

The image acquisition was controlled by the camera interface software *Photron FASTCAM Viewer*, provided by the manufacturer, through which, in addition to the camera

parameters, also the synchronization with the other instruments could be controlled, with the perspective to obtain images of the sequence of interest.

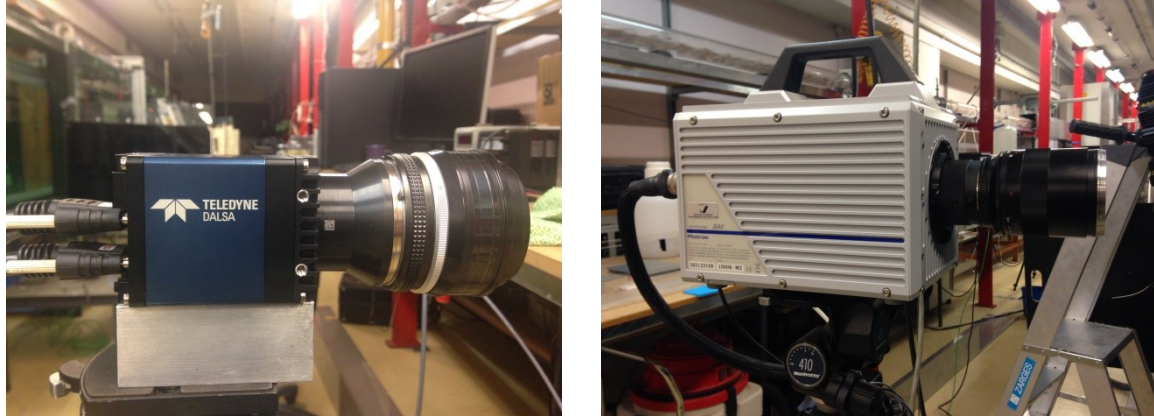


Figure 18. CCD cameras. Left panel: Teledyne DALSA. Right panel: Photron FASTCAM SA5.

Seeding particles

The flow was seeded with neutrally-buoyant polyamide particles (PSP) of the diameter of approximately $50\ \mu\text{m}$ (Figure 19). The tracking particles were tested to faithfully follow the fluid.

The seeding of the flow is a fundamental phase of the PIV measurements, because a very homogeneous seeded flow field is at the base of an accurate measurement of the flow quantities.



Figure 19. Seeding particles.

4.2.3 Synchronization system

Timing and synchronization of all the instruments were achieved using the paddle trigger signal as external input signal for both experimental setups. A triggered acquisition provides two key benefits to the user: it times the input signal relative to the trigger event, so that the user captures the signal only in the region of interest, and conserves hardware bandwidth and memory.

With reference to Setup1, an analogic trigger circuitry (ATC) on the DAQ hardware continuously monitored the analogic signal to determine if it satisfied the trigger condition. When the trigger conditions were met, the ATC generated an internal trigger signal to start the acquisition. In details, a trigger box was used to control the camera. Instructions about the trigger for the camera was managed by means of *Sapera Cam Expert*, setting the external triggering on and the trigger source. A self-made *LabView* program, called *Trigger Pulse*, was written to generate the internal trigger for the instrumentations on the basis of pre-set features, such as exposure time and delay in imaging acquisition after the paddle start. With this system, the recording of measurements was controlled by the external trigger signal from the paddle. A delay of 10 sec from the paddle start was imposed for the measurements of wave gauges, force transducers, pressure sensor and images. An additional delay was set for the camera acquisition start in the *Trigger Pulse* programme, caused by the different impact time typical of each wave condition run. A ten-second sequence of images, in correspondence of the wave impacts on the cylinder, was recorded for each test.

More complexity was added by the laser synchronization in the case of Setup2. Starting from the same system previously mentioned to control the external trigger input from the paddle and the instruments, another *LabView* programme, called *LaserSync*, was coded, which added the synchronization between the laser and the camera. It was needed in view of the double-pulsed nature of the beam of the laser. It was fundamental to have the laser pulses within the exposure time of the camera, otherwise black images would have been recorded.

More in detail, a DAQ system matched the external trigger input signal from the paddle (with respect to which all the instruments were controlled) with both the programmed

delay (evaluated on the basis of video-records of the waves) and the duration of the camera exposure coming from a programmable pc. In summary, the DAQ system sent both a trigger input signal to the camera for recording and the synchronization signal to the camera and the laser, at the same time. The camera control pulses were generated by the system synchronizer, which received a synchronization pulse from the scanner delayed of 200 ms with respect to the camera, in order to ensure that the laser light pulses occurred during the exposure time of the camera. The timing diagram is reported in Figure 20.

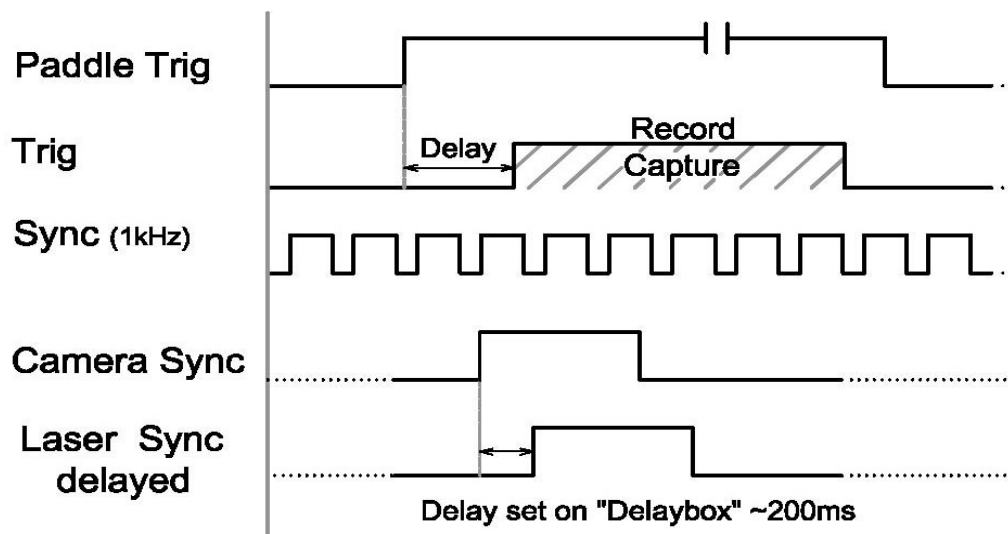


Figure 20. Timing diagram of the synchronization system related to the Setup 2.

4.3 Experimental investigation of the flow upstream the cylinder: Setup1.

Setup1 consisted in a single cylinder, configured as mentioned in section 4.2.1, built to collect measurements both of the pressure on the upper part of the cylinder and of the force acting on the cylinder. In addition, the flow on the centreline vertical plane upstream the cylinder was investigated by the PIV technique.

For the installation of pressure transducers, the cylinder was longitudinally cut and screwed holes were made along the centreline of a half part of it, with the aim to create allocations for the pressure transducers. A perforated bar in polyethylene was printed for the scope and glued in correspondence of the holes to help reach perfectly perpendicular screwed instruments and have their face aligned with the external surface of the cylinder.

Five pressure transducers were placed, vertically aligned along the frontline of the cylinder at a constant distance of 3 cm from each other (see Figure 21, left panel). Three of them (P1-P2-P3), of range of 3.5 bars, were placed above the still water level (swl), covering a total length of 9cm from the swl, to capture the pressure caused by the wave front. The remaining ones (P4 and P5), with a measuring range up to 0.7 bars, were located in correspondence of the swl and 3 cm below, respectively.

The two half parts of the cylinder were then glued together to reassemble the cylinder to be plugged on the hinge. After the above activities the cylinder surface was not perfectly smooth, thus pressure measurements over $\pm 45^\circ$ were not made possible.

The cylinder was connected to the hinge and fixed at its top to the force measurement system previously described. Additionally to the measurements along the frontline of the cylinder, in the range +9 to -3cm from the swl, the cylinder was rotated around its vertical axis of 15° at a time up to $\pm 45^\circ$, thus obtaining pressure measurements around the cylinder cross-sections at the previously-mentioned elevations (Figure 21, right panel, as an example).

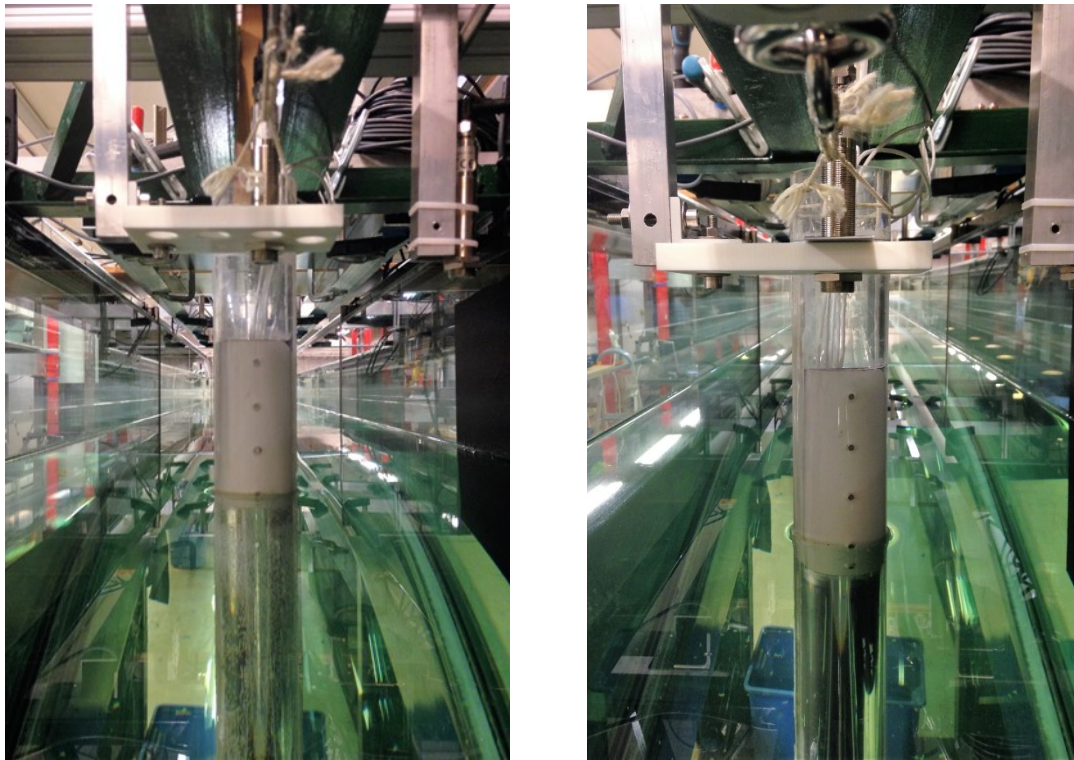


Figure 21. Setup1. Configuration of pressure transducers, namely P1 to P5, from top to bottom. Left panel: cylinder with pressure transducers at the frontline, i.e. the rotation of the cylinder is equal to 0° . Right panel: counterclockwise rotation of 15° of the cylinder with pressure transducers.

An sample view of Setup1 object is reported in Figure 22, related to an instant soon after the seeding of particles. At least 10 minutes had to be waited after the seeding to reach a homogenous dispersion of particles and at least 20 minutes between a test and another to ensure the calm condition of the water.

The water was seeded as homogenously as possible with PSP particles. The LED lamp, was used at 140% of its intensity, exploiting the benefits of the liquid cooler system of the lamp. It was placed below the tank bottom, facing upwards, aligned with the longitudinal centreline of the tank, straddling the cylinder. A vertical white light sheet was then obtained. The *Falcon* camera was placed outside the cylinder, on the side, framing a field of view that included 15 cm of flow below the swl, the swl and 10 cm above the swl, in order to capture the wave front in all cases. The *Falcon* camera was configured to record at the maximum resolution of 2432×1728 and at 100 Hz of frequency. A sequence of 10 seconds of the wave impact event was recorded for all the wave cases tested.

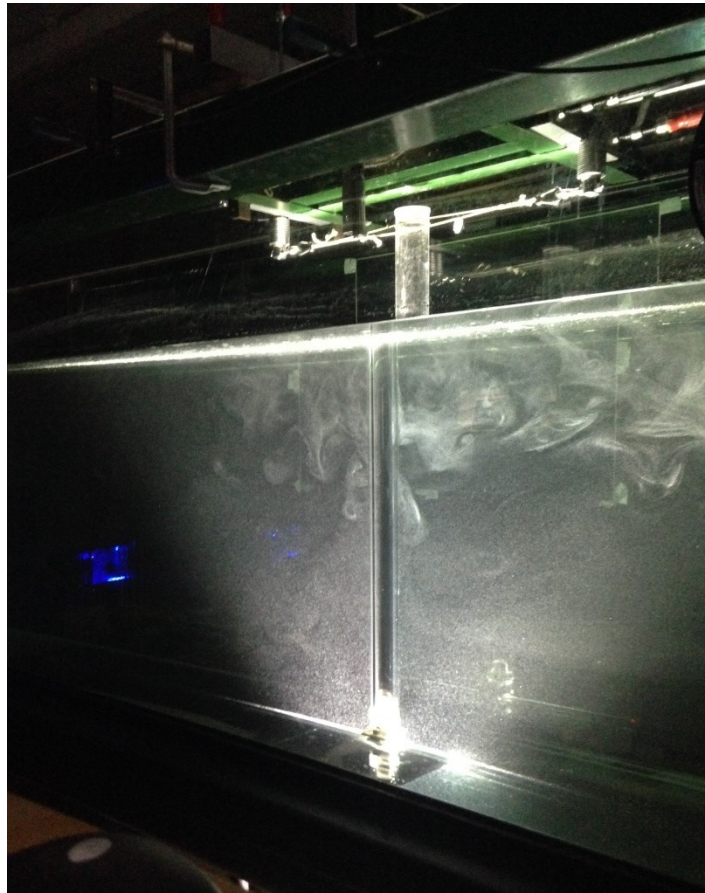


Figure 22. View of the final configuration of Setup1, right after the seeding with particles.

4.4 Experimental investigation of the flow downstream the cylinder: Setup2.

The investigation of the two-dimensional flow evolving on horizontal planes at the lee side of the cylinder was the main goal of Setup2. In this framework, a perfectly intact cylinder replaced the one of Setup2. It was located at the same position in the tank and fixed at the force system in the same way previously explained.

The PIV system, consisting in a camera and a laser beam as illumination source, was configured as follows (see also Figure 23). A Nd:YLF pulsed laser source (*Quantronix Darwin Duo 15mJ@3000 Hz*) was placed laterally to the tank. The longitudinal beam was firstly deviated by a system of mirrors to reach in elevation the position of the field to be

investigated and, then, it was spread by an optics into a horizontal homogeneous light sheet illuminating the backside of the cylinder.

The *Photron FASTCAM SA5 1000K-M2* high-speed CCD camera was located under the tank and facing upwards normally to the light sheet. It captured images of a field of view of 10cm×10cm, including part of the cylinder backside (it was less than half cylinder because the hinge at the bottom obstructed its complete view) and of the flow. The camera was set to record a sequence of 10000 frames starting from a pre-established delay in function of the wave, with a resolution of 1024×1024 and at a frequency of 1000 Hz.

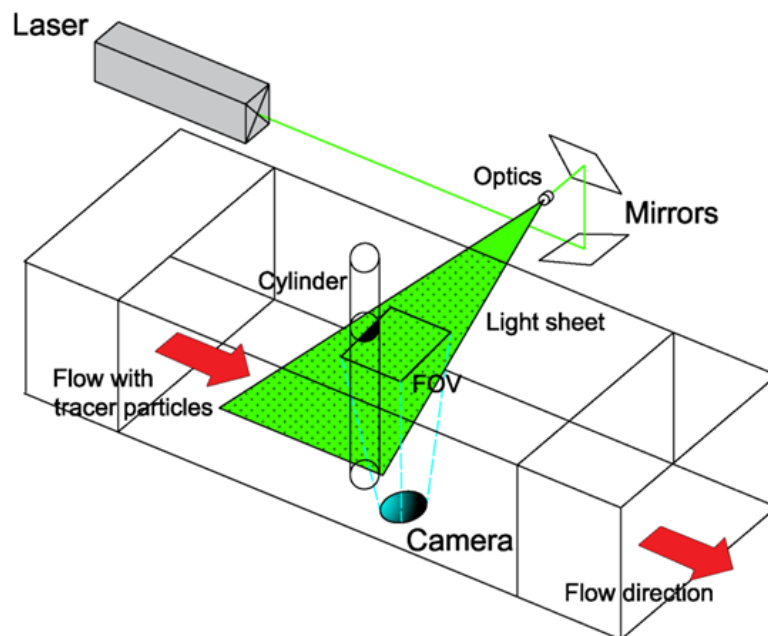


Figure 23. Sketch of the PIV arrangement for Setup2.

Four horizontal planes (POS0-POS3), parallel to the tank bottom, were investigated, as indicated in Figure 13 and reported in Table 1, shifting down the light sheet from the swl of about at a time (the numbering follows the ascending order with respect to the swl). This operation implied the movement of the system of mirrors and optics, as well as of the target used to check the correct position of the light sheet, so that was not a trivial task.

Position	Level	
POS 0	-0.005 m swl	+0.715 m bottom
POS 1	-0.055 m swl	+0.665 m bottom
POS 2	-0.105 m swl	+0.615 m bottom
POS 3	-0.155 m swl	+0.565 m bottom

Table 1. Position of the investigated horizontal light sheets on the backside of the cylinder.

A sample view of Setup2 object is reported in Figure 24.

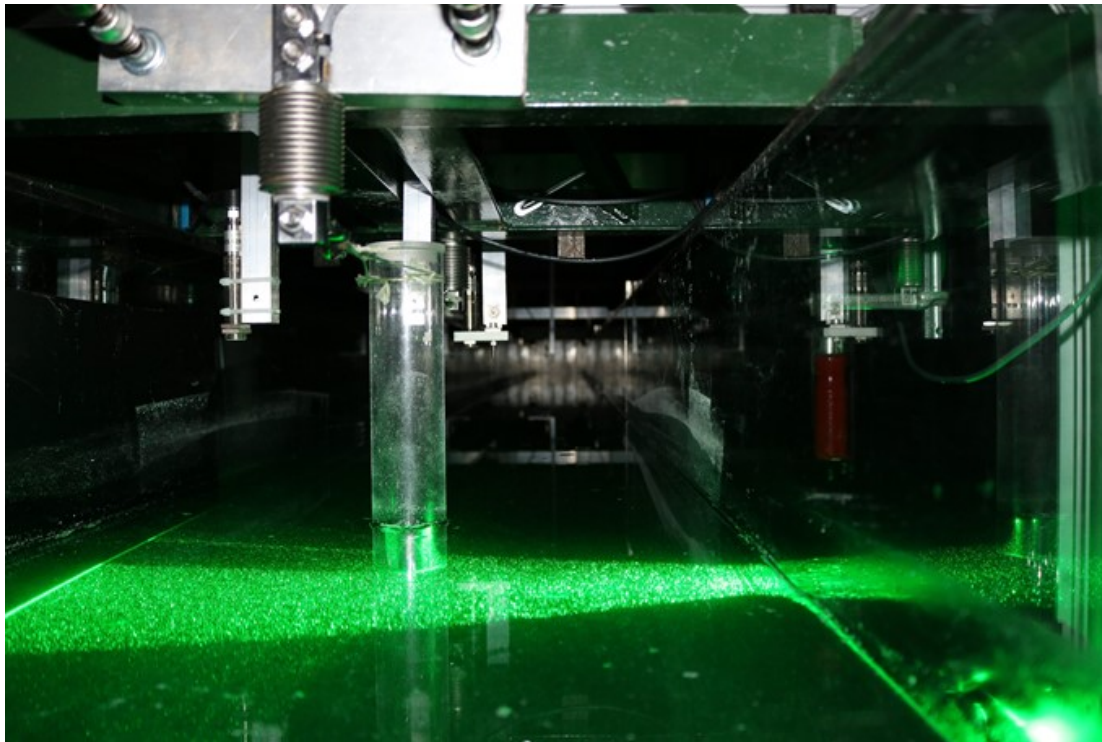


Figure 24. View of the final configuration of Setup2, during a PIV acquisition.

4.5 Wave generation

A constant water depth of $h = 0.72$ m was used for all the runs of the reported experiments, representing deep-water conditions ($kh > 1.6$) for the tested waves.

With the aim of generating steep, breaking and near-breaking, waves at the cylinder, the wave frequency-focusing technique was employed, this being recognized as the most suitable method to simulate the natural mechanism of generation of breaking waves in deep water Chaplin (1996).

This technique, based on the linear dispersion theory, led to design a wave packet that converged up to the desired time and spatial location, generating a single large wave. The technique was implemented and used in the tank by Brown and Jensen (2001). The reliability of the wave generation has been object of investigation of several previous works by Huseby and Grue (2000) for Stokes waves and by Jensen et al. (2001) and Jensen and Grue (2002) for focusing wave groups.

A third-order Stokes wave provided the reference for the experiments (for more details, see Grue et al., 2003; Jensen et al., 2001).

4.6 Wave characteristics

Seven different deep-water waves, achieved by varying the amplitude and frequency of the wave packets, were tested (see, Table 2).

Among these, six cases have been selected basing upon the results by Osyka (2016), while an extreme case was added, leading to four different scenarios of impact:

- i) impact of strong spilling breakers,
- ii) impact of weak spilling breakers,
- iii) impact of very steep, non-breaking waves,
- iv) impact of plunging breakers.

Wave parameters are summarized in Table 2. A single wave event was defined by the crest height η_c and the through-to-through period T_u identified from the mean over three

repetitions of the surface elevation time-histories recorded at WG4 in undisturbed conditions. The zero-up crossing period T_f was also calculated and reported in the same table, as alternative way to estimate the period. The mean value between the two calculated periods T_u and T_f provided the averaged period T_{av} .

The wave number k and the wave slope ε can be obtained by solving numerically the system of equations:

$$\begin{aligned}\frac{\omega^2}{gk} &= 1 + \varepsilon^2 \\ \eta_c &= \varepsilon + \frac{1}{2}\varepsilon^2 + \frac{1}{2}\varepsilon^3\end{aligned}\tag{4.1}$$

where $\omega=2\pi/T_u$, resulting from the third-order Stokes wave theory.

Further wave parameters, important for the interpretation of the results (previously presented in section 2), are, thus, derived and here reported. In particular, with regards to the flow field, the Keulegan-Carpenter number, denoted with $KC= U_c T_{av}/D$ and taken to measure the flow separation effects, and the Reynolds number $Re=U_c D/\nu$, taken to measure the relative role of inertia to viscosity, were computed with reference to the crest assuming the approximated flow velocity $U_c=2\pi\eta_c/T_u$. In addition, the Froude number expressed by $Fr=U_c/\sqrt{g/D}$ (where g is the acceleration due to gravity) is of support to interpret the connection between the wave-induced force and the occurrence of flow separation.

All the wave events reported in Table 2 were tested on the configuration of the main experiments, i.e. on the Setup 2. Wave case 4.1, instead, is lacking in the laboratory experiments conducted on the secondary setup, i.e. on the Setup1.

Cases	Description	η_c (cm)	T_t (s)	T_f (s)	T_{av} (s)	$k\eta_c$	kR	KC	$Re \times 10^4$	Fr
1.1	Strong spilling br.	7.98	0.992	1.023	1.008	0.297	0.112	9.39	3.35	0.729
1.2	Strong spilling br.	7.63	1.068	1.076	1.078	0.252	0.099	8.84	2.95	0.641
2.1	Weak spilling br.	4.70	0.588	0.629	0.609	0.452	0.289	5.27	3.46	0.752
2.2	Weak spilling br.	4.30	0.608	0.625	0.617	0.409	0.286	5.86	3.07	0.668
3.1	Very steep non-br.	9.21	1.124	1.202	1.163	0.260	0.085	10.7	3.31	0.720
3.3	Mildly steep non-br.	5.39	1.236	1.275	1.271	0.132	0.074	5.98	1.69	0.368
4.1	Plunging br.	11.30	0.980	1.024	1.024	0.393	0.104	13.8	4.84	1.05

Table 2. Parameters of the tested waves: η_c surface elevation at the crest measured by WG4, T_t trough-to-trough period, T_f zero up-crossing period of the force history, $T_{av}=(T_t+T_f)/2$ average period, L wave length, k wave number, $k\eta_c$ wave slope, kR dimensionless wave number with respect to the cylinder radius, Re Reynolds number, KC Keulegan-Carpenter number and Fr Froude number.

Chapter 5

RESULTS AND DISCUSSION

5.1 Overview of the acquired data

The main aim of the present study was to investigate the secondary load cycle onto a vertical cylinder exposed to steep waves in deep waters, in the attempt to clarify the causes of occurrence and, eventually, to relate the secondary load cycle to the ringing response. In this perspective, the investigation by PIV of the flow downstream the cylinder was also conducted, measuring the flow over horizontal planes at different vertical elevations.

Within the broader framework of the collected experimental data, the measurements acquired on Setup2 are herein reported and discussed.

The experiments performed on the cylinder configuration Setup2 covered all the wave cases reported in Table 2. Three realizations of the test were carried out for each wave, resulting in a total of 84 tests performed. Each run provided the free surface wave profile at four positions along the channel (as described in paragraph 4.2.1), among them particular interest is in the incident wave elevation at the cylinder recorded by gauge WG4, and the total force acting on the cylinder. In addition, a sequence of 10000 frames of a 10cm×10cm field of view on the lee side of the cylinder was collected for each of the four investigated levels of each test wave. All measurements were synchronized.

The force signal is analysed to identify the presence of the secondary load cycle, in concurrence with the elevation signal close to the cylinder, i.e. at WG4. PIV data are analysed to obtain the flow velocity fields and, then, post-processed to visualize flow separation and vortex generation downstream the cylinder.

On the basis of an overall analysis of the above-mentioned data, a global and comparative description of the processes occurring in relation to each wave event is reported. General trends of occurrence of the secondary load cycle related to vortex regimes and wave conditions are recognized and a discussion of the results is presented in light of the state of the art and the recent developments of the research on this topic.

5.2 Data analysis

Force, elevation and PIV images data needed to be analysed before being used, to ensure a correct visualization and interpretation of the investigated phenomena.

Correction, elaboration and visualization of the data were mainly carried out by specifically coded *Matlab* routines. Furthermore, PIV dedicated software packages were used for the analysis of the raw images.

5.2.1 Elevation signals

Water surface elevation has been reconstructed from the acoustic wave gauge measurements.

Due to the operational mode of acoustic wave gauges, which is based on the estimation of a distance from the time passed between transmission and back reflection of an acoustic signal, the water surface is recorded as the distance from the probe. This means that the acquired signal must be manipulated to give the elevation as the distance from the still water level. Therefore, first the analysis dealt with this aspect. Elevation time-series were calculated by subtracting the wave gauge measurement in calm water conditions from the recorded signal.

Secondly, elevation profiles with data dropouts were re-constructed. For some wave cases, data dropouts in the measured surface elevation were observed at locations where the waves were particularly steep, i.e. between the trough and the crest of a steep wave. This effect occurs because, when the surface has an inclination angle larger than the maximum inclination angle of the probe, the transmitted signal is reflected outside the sensing range of the instrument. In correspondence of a data dropout a NaN value is reported in the data array containing the information on the surface elevation.

Holes in the water elevation signal were thus filled by a common reconstruction based on piecewise polynomial of a shape-preserving piecewise cubic Hermite interpolant (Figure 25), already demonstrated to be reliable for our data reconstruction by Osyka (2016).

Each recorded elevation timeseries was analysed by an in-house built *Matlab* routine. The final wave surface elevation profile was obtained as the ensemble average over the elevation signals from the three repetition of the test.

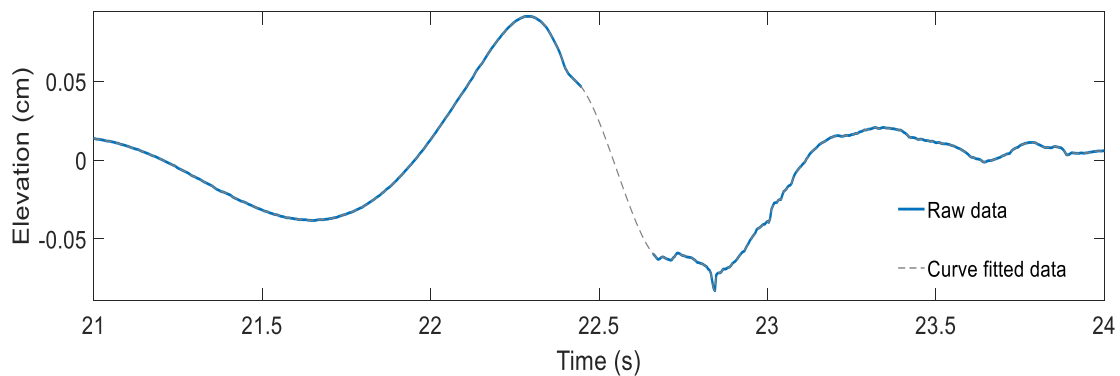


Figure 25. Example of curve fitting on wave 3.1.

5.2.2 Force signals

The force acting on the cylinder at the passage of the wave was recorded by the system of force measurements from the load cells described in paragraph 4.2.2.2

The force timeseries was obtained by the acquisition software as the difference of the force values recorded by each load cell. Different types of noise can, however, affect the force signal. The first is a high-frequency electric noise that comes from connections of the system not sufficiently grounded. Another one is due to the motion of the wavemaker; but for most of the tests the wavemaker was still during the measurement period. Finally, in some experiments, especially when slamming on the cylinder occurred, a response of the cylinder at its natural frequency may occur. This response is only related to the physical properties of the structure and leads to larger values in force recording.

For this reason, the raw data were filtered using a lowpass Butterworth filter to remove the structural response contribution associated with the eigenfrequency of the cylinder, without altering the information. A Butterworth filter function of order 9 was used and the cutoff-frequency set to be around 20 Hz. This latter, which represents the natural frequency of the cylinder, was determined on the basis of the spectral analysis of the force signals recorded during the wave events. In all cases, a first small force peak, occurring before the passage of the wave crest, was recognized as the structural response of the system. The cut-off frequency was established on the basis of this value.

Figure 26 gives an example of the force time history before (grey line) and after (red line) filtering.

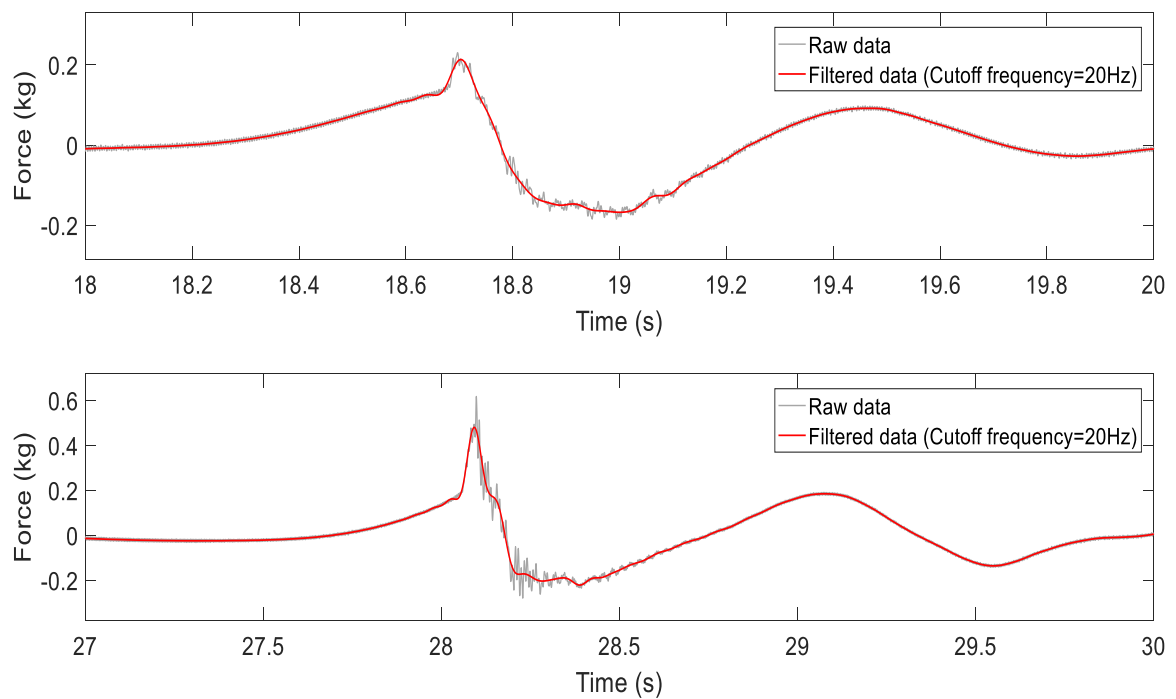


Figure 26. Example of filtering of a force signal: wave 1.1 (top panel) and 4.1 (bottom panel).

5.2.3 PIV images analysis

The Eulerian velocity fields have been obtained by analysing the raw images through two different PIV pieces of software, i.e. *Digiflow* and *ProVision XS*. However, only the analysis conducted by means of the *ProVision XS* software is reported and used for the discussion.

The procedure of the analysis was very similar for the two different pieces of software. First, it was useful to mask out the portion of the raw images occupied by the cylinder, in order to exclude it from the analysis. Removing unwanted areas reduces the computational effort and makes the analysis faster. The mask was, in general, implemented directly from the software and set to zero the pixels included in the areas to be masked and to one all the others.

Then, a coordinate transformation was generated to convert the output in physical quantities. The transformation from camera coordinate (pixels) to real coordinates (world) was possible by introducing some reference points of known positions. In this case, a frame of the same investigated FOV capturing a target of points 2 cm apart was used. The PIV software generated the transformation function from the position of those points in pixels and their real distances set by the user, thus calculating how large each pixel is in the images.

At this stage, the starting parameters of the PIV analysis had to be set. For these analyses, the images were divided into a regular grid of 32pixel×32 pixel subwindows with 50% overlap, while the function of subwindows automatic resizing was optioned when needed. The search range was set to go from -16 pixels to 16 pixels, following the general rule that it should be at least half the subwindow size.

The analysis was conducted according to the principles the procedures described in section 3.1.1. The cross-correlation is typically used to find the optimal match of the displacements between particles. Finally, noise filters and the detection and replacing of outlier vectors were applied. The latter consisted in the identification of vectors outliers in the weighted least square sense, matching it with the neighbourhood vectors. An outlier

reconstruction was made on the basis of the evaluation algorithm used, i.e. by fitted B-spline.

The analysis gave as output the velocity field of the flow in the investigated FOV in real coordinates. An example of an instantaneous velocity field obtained from PIV analysis is reported in Figure 27.

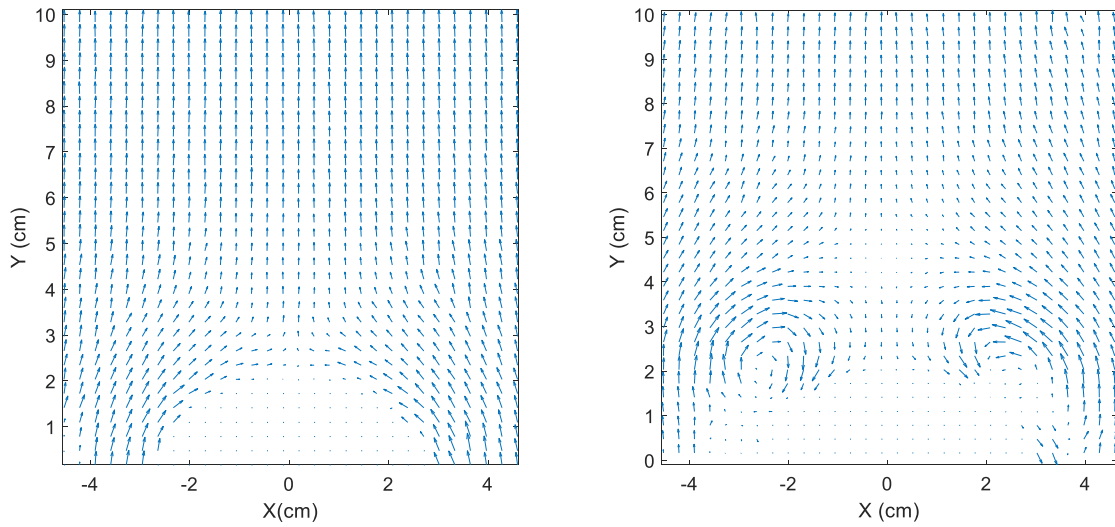


Figure 27 Example of instantaneous velocity field from PIV analysis: case 1.1 (left panel) and case 3.1 (right panel), at different times subsequent to the wave passage, with incident flow from bottom to top.

5.2.4 PIV post-processing: vorticity analysis

Post-processing of the velocity fields was conducted, to determine the vorticity fields.

The vorticity component orthogonal to the plane of motion is defined as:

$$\omega = \nabla \times \mathbf{V} = \frac{\partial u}{\partial y} - \frac{\partial v}{\partial x} \quad (5.1)$$

where (u, v) are the horizontal and vertical components of the velocity vector V .

Alternatively, like in this case, the calculation of the vorticity can be performed by using the circulation, i.e. the value of the line integral around a closed curve of the velocity field.

$$\Gamma = \oint V \cdot ds \quad (5.2)$$

with ds differential length.

The circulation is related to the vorticity as:

$$\Gamma = \oint_{\partial S} V \cdot ds = \iint_S \omega \cdot dS \quad (5.3)$$

only if the integration path is a boundary (indicated by ∂S) of a closed surface S of a vortex tube, not just a closed curve. Thus, the vorticity is the circulation per unit area, taken around an infinitesimal loop. Correspondingly, the flux of vorticity is the circulation.

In this perspective, calculation of vorticity at a point was made by considering the closed curve defined by the velocity components of neighbouring points.

5.3 Vortex generation and evolution

Vorticity maps superposed to the relative velocity fields have been produced as a means of comparison between the tested wave events.

A description of the formation and evolution of vortices is provided. In particular, only cases more representative of a specific vortex evolution are reported. For each of these cases, some significant times were selected to better capture the evolution of the vortex formation.

In particular, the characteristics of the evolution of vortices can be described with reference to the following phases:

- The beginning of vortex roll-up from the wall boundary layer, phase A;
- The time at which the vortex roll-up is completely developed, phase B;
- The beginning of the vortex shedding, phase C;
- The time at which vortices reach their maximum dimension and intensity, phase D.

The representation is in the form of maps of vorticity and relative velocity fields for the times (A-D) individuated from the elevation timeseries at different elevations, from -5.5 to -15.5 cm from swl, corresponding to the investigated horizontal planes (POS1-POS3). Maps related to POS0 (at swl) were not reported because not meaningful for all cases, due to the fact that in some instants the light sheet crosses the trough and the flow is not visible.

All lengths, such as the x and y dimensions of the FOV and the free surface elevation η have been normalized by the cylinder diameter D . The time t has been normalized by $\sqrt{g/D}$.

Case 1.1, representing a strong spilling wave, is reported as representative also of case 1.2. Vortex formation and its evolution are very similar for these two cases, whose wave parameters are similar (see Table 2). The observation of the whole sequence of analysed images capturing the wave event, led to select time instants A-D in Figure 28, consistent with the physical description of the vortex evolution phases previously adopted.

The vorticity maps show the formation of small vortices close to the cylinder surface after the crest passage. In the descending part of the wave, between the crest and the following trough, vortices evolved a little in size, up to reach their maximum dimension at instant D , soon after flow inversion. The vertical structure of the vortices, from the upper to the lower plane, is such that moving downward the vortices decrease in size and intensity, almost disappearing in correspondence of POS3. This suggests that the vortices that remain very close to the cylinder have a funnel shape with minimum size at the lowermost location (POS3).

A completely different scenario characterizes case 3.1, related to a very steep non-breaking event (Figure 29). Here, vortices arise just before the wave crest in the form of small coupled vortices attached laterally to the cylinder and with stronger intensity at the lowest plane POS3. Only at time B, vortex pairs of similar intensity of those of POS3 appear also in the upper layers (POS1-POS2). Vortices are seen to converge, moving by self-induction along the cylinder wall, to the cylinder centreline location and from there pair with oppositely-signed vortices and migrate, by mutual induction, away from the cylinder along a diagonal path. Similarly occurs at time C, but with vortices and vortex pairs of stronger

intensity. The largest and most intense vortices are found at time D, i.e. just prior to flow inversion. These have comparable size and intensity over the water column and do not seem to foster any pairing and migration by mutual induction, rather they remain quite attached to the cylinder.

A weak vortex formation is observed in case of the mildly steep, non-breaking wave 3.3 (Figure 30). Although less clearly distinguishable than in the previous cases, small and weak vortices are seen to evolve in a way similar to case 3.1. In fact, vorticity is more generated during the elevation decay stages, i.e. soon after the crest, and the shape and location of vortices recalls what observed in the previous case 3.1. Both of them are non-breaking events, but they are characterized by very different wave parameters, especially in terms of KC.

Finally, case 4.1 of a plunging breaker is reported (Figure 31). In this case, no vortex formation is induced by the passage of the wave crest, neither at the stages of the wave trough. Vortex formation only appears as associated to the secondary wave, probably product of the convergence of some in-wave components or run-up. In the time interval identified by A-D, the vortex formation looks very similar to that of case 1.1 (Figure 28) in shape and location, even if in this case the vortex activity seems more intense. This may be justified by the fact that case 4.1 represents a much stronger event than case 1.1.

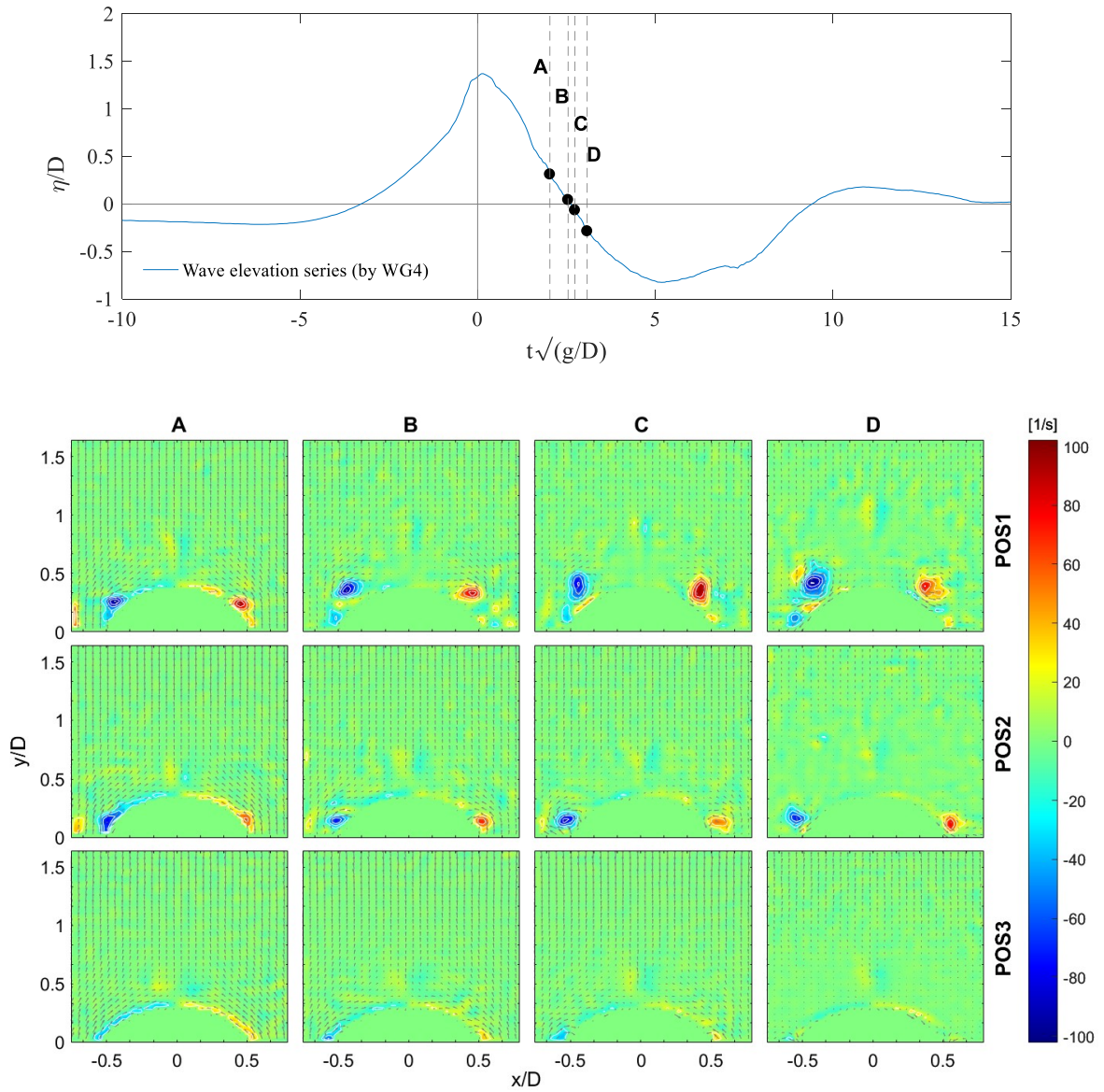


Figure 28. Vortex evolution for case 1.1. Top panel: Time history of the wave elevation. Bottom panel: Vorticity maps at times (A-D) and at horizontal planes (POS1-POS3). Incident flow from bottom to top.

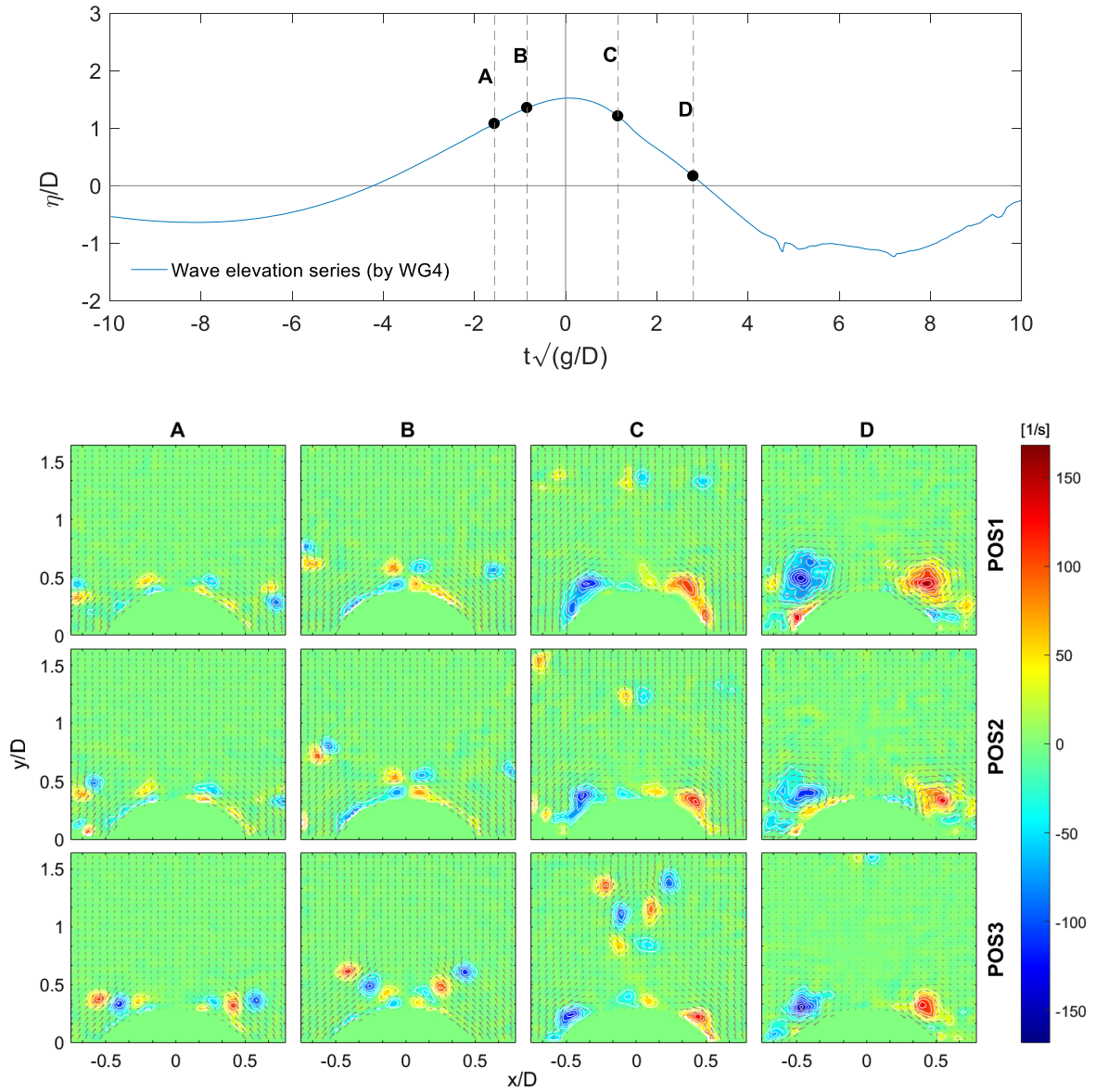


Figure 29. Vortex evolution for case 3.1. Top panel: Time history of the wave elevation. Bottom panel: Vorticity maps at times (A-D) and at horizontal planes (POS1-POS3). Incident flow from bottom to top.

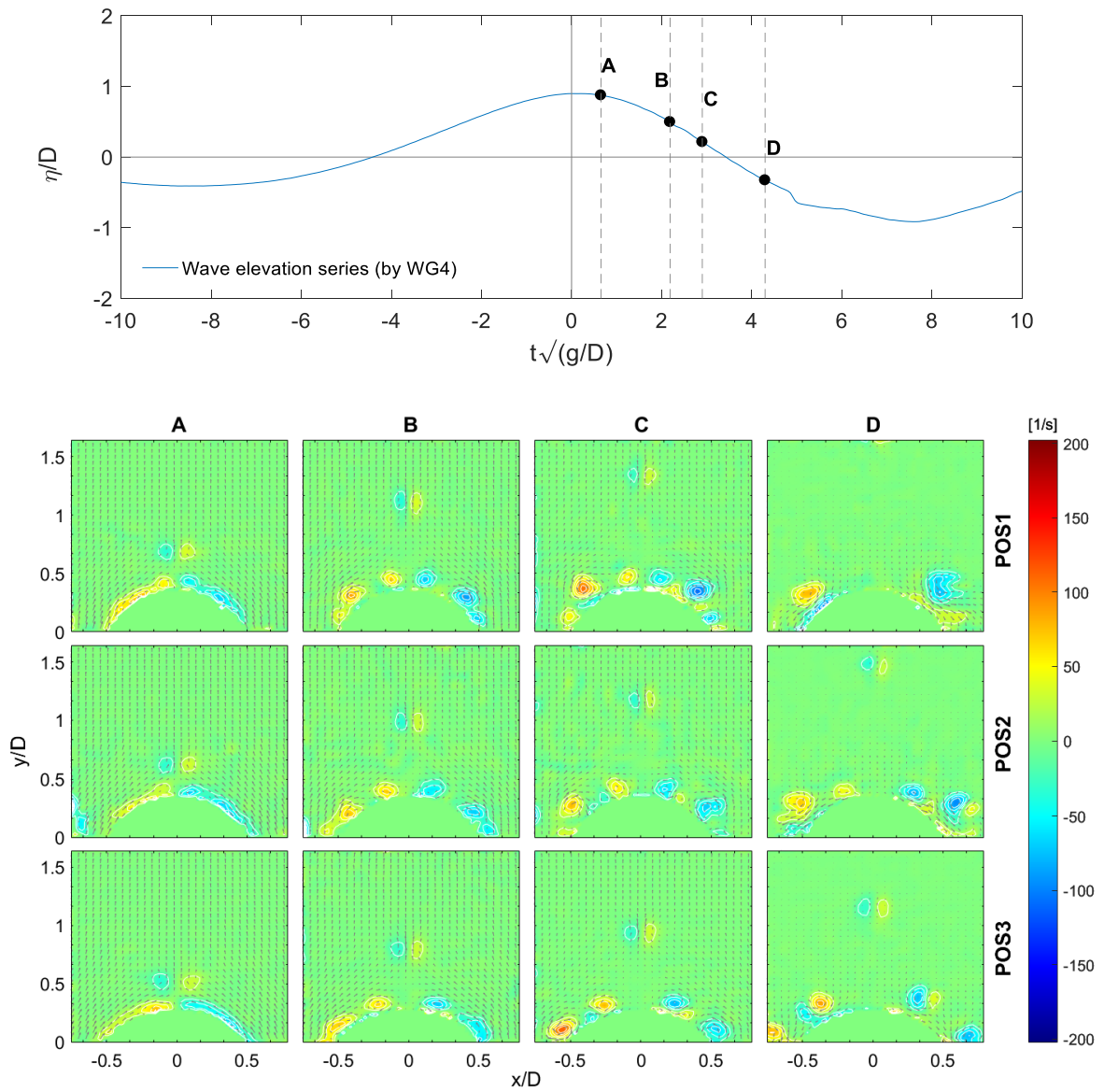


Figure 30. Vortex evolution for case 3.3. Top panel: Time history of the wave elevation. Bottom panel: Vorticity maps at times (A-D) and at horizontal planes (POS1-POS3). Incident flow from bottom to top.

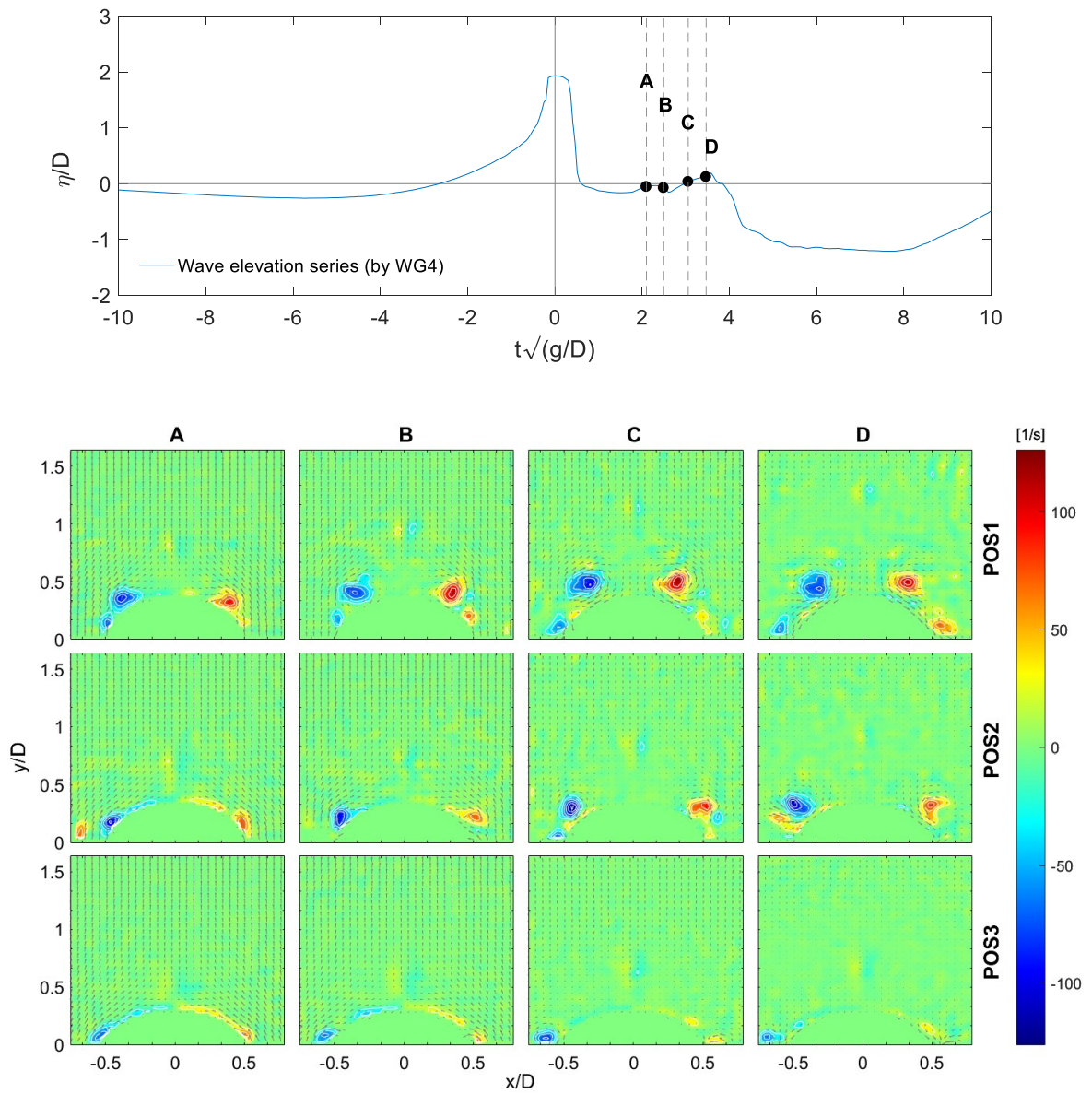


Figure 31. Vortex evolution for case 4.1. Top panel: Time history of the wave elevation. Bottom panel: Vorticity maps at times (A-D) and at horizontal planes (POS1-POS3). Incident flow from bottom to top.

5.4 Secondary load cycle dynamics

A second analysis is aimed at the interpretation of the role played by the observed vortices in the evolution of the secondary load cycle that characterizes the force time history.

The presence of a secondary load cycle was recognized for cases 1.1, 1.2, 2.1, 2.3, 3.1 and 4.1. According to the criteria previously used, only one representative case among similar ones is reported, for the sake of brevity. Thus, cases 1.1 and 2.1 were chosen as representative also of cases 1.2 and 2.3, respectively.

With the aim to characterize the dynamics of the secondary load cycle, the wave-exciting moment has been investigated, and related to the free surface elevation. The moment M has been normalized with $\rho g z_a D^3$.

Some significant times have been used, around the time of the secondary load cycle and following according Liu et al. (2019), to investigate the dynamics in conjunction with the evolution of coherent vortices. It is noted that these times are different from those used in the previous analysis (paragraph 5.3) to describe the vortex evolution.

In particular, the characteristics of the secondary load may be described by:

- The time corresponding to the crest of the wave-exciting moment, A’;
- The starting time of the secondary wave load, B’;
- The time corresponding to the peak of the secondary load cycle, C’;
- The end time of the secondary load cycle, D’.

For these times, the SLC ratio, giving information on SLC intensity, has been calculated (as reported in paragraph 2.3.2.1).

An overall reading of the vorticity evolution in correspondence with the SLC is thus provided.

For the case of strong spilling breaker 1.1, a SLC is visible (Figure 32). The moment series (Figure 32, top panel, red line), in fact, display a clear second wave load after the main one, right before the minimum loading.

At time A', in correspondence of the crest, no vorticity appears at all the investigated horizontal levels (POS1-POS3). It is just after the crest (time B') that some vorticity is formed rolling up to generate small symmetrical vortices placed quite laterally, close to the cylinder.

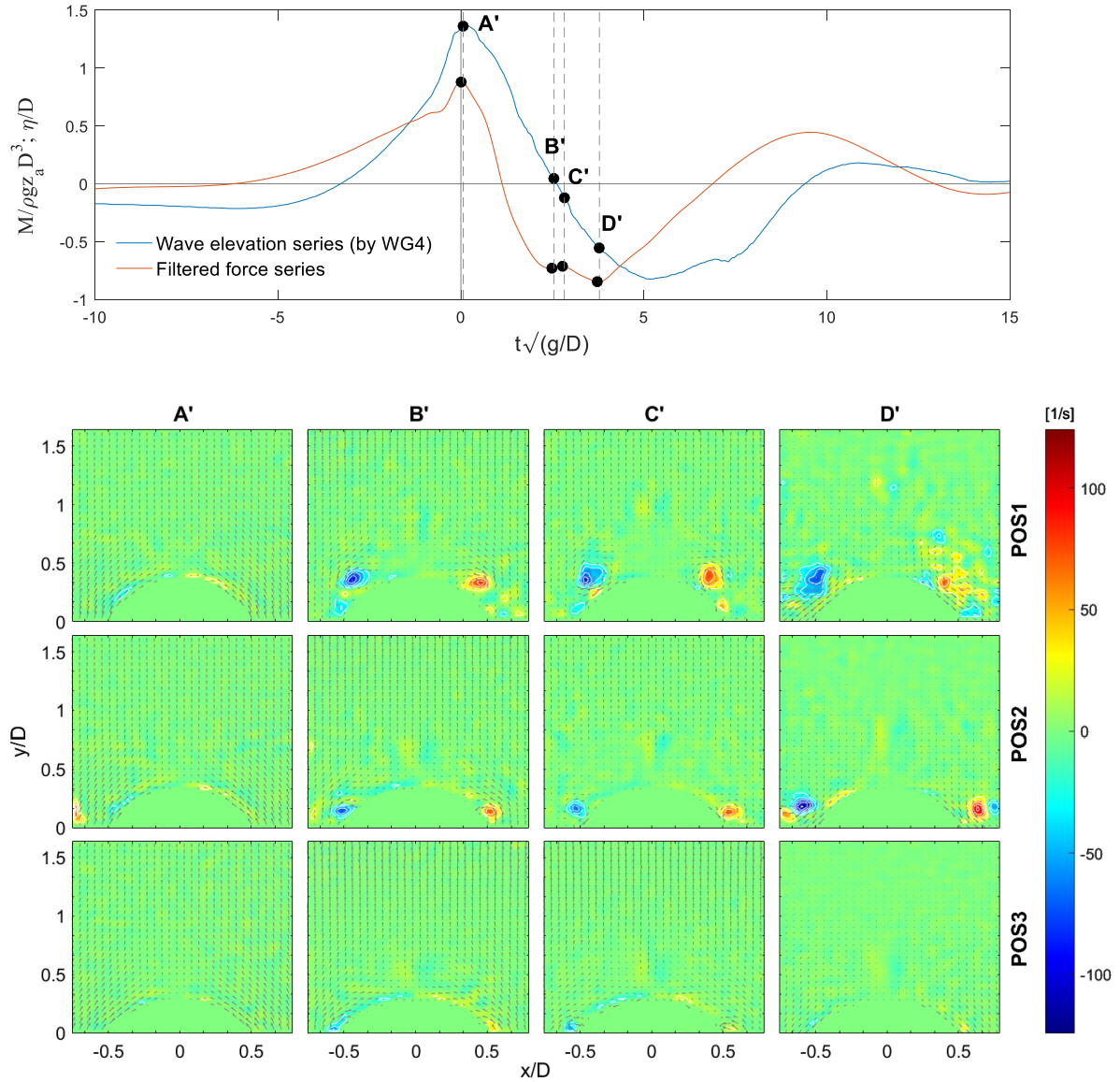


Figure 32. SLC dynamics for case 1.1. Top panel: Time histories of wave elevation (in blue) and wave-exciting moment (in red). Bottom panel: Evolution of the vorticity at times (A'-D') significant for the SLC, and at horizontal planes (POS1-POS3). Incident flow from bottom to top.

These vortices increase in dimension achieving their maximum size in correspondence of the instant C', which identifies the peak of the SLC. From D', vortices tend to break-up, due to the inversion of the flow. The same trend is recognized also at level POS2, but the vortices appear weaker and smaller. No significant vorticity is observed, instead, at level POS3. The overall behaviour here observed confirms what already seen when inspecting the vortex dynamics alone as reported in Figure 28 and related text.

With reference to case 2.1, representing a weak spilling breaking wave event, a SLC is recognized, but no vortices of some importance are generated by this flow (Figure 33).

A weaker SLC occurs for the case of the very steep, non-breaking wave of case 3.1 (Figure 34). In correspondence of the wave-exciting moment peak (A'), only weak vortices are generated, mainly at level POS3, where a pair of small vortices is generated symmetrically at the sides of the cylinder. Vorticity develops gradually after the crest and appears large and intense already at time B'. Its maximum intensity is reached at the peak (C), which coincides with time D' of Figure 34, while at stage D' vortices are disrupted. Noticeable is the fact that the vortex-shedding stages, visible in Figure 34 occur between the wave-exciting moment peak and the peak of the secondary load.

More complicated is the discussion of case 4.1 (plunging breaking wave), reported in Figure 35. Here, the identification of the SLC is not trivial, because of the many oscillations in the wave-exciting moment signal after the crest. On the basis of the selected event, identified in Figure 35, no vortex formation is detected anywhere (POS1-POS3), except at instants C' and D' of the two upper levels (POS1-POS2). At C', corresponding to the SLC peak, the formation begins and at D' it is just developed. This observation, which together with the results of Figure 35 clearly suggest a weak to no influence of the vortex dynamics on the SLC dynamics, seems to be in contrast with the more important role of vortical structures on the SLC evolution observed for the other cases (also in view of the intense breaking caused by the plunger). However, it may be possible that the actual SLC has not been properly detected and could be much posticipated to times $2 < t\sqrt{g/D} < 4$. In this case, the associated vorticity formation would be that described by the maps of Figure 31.

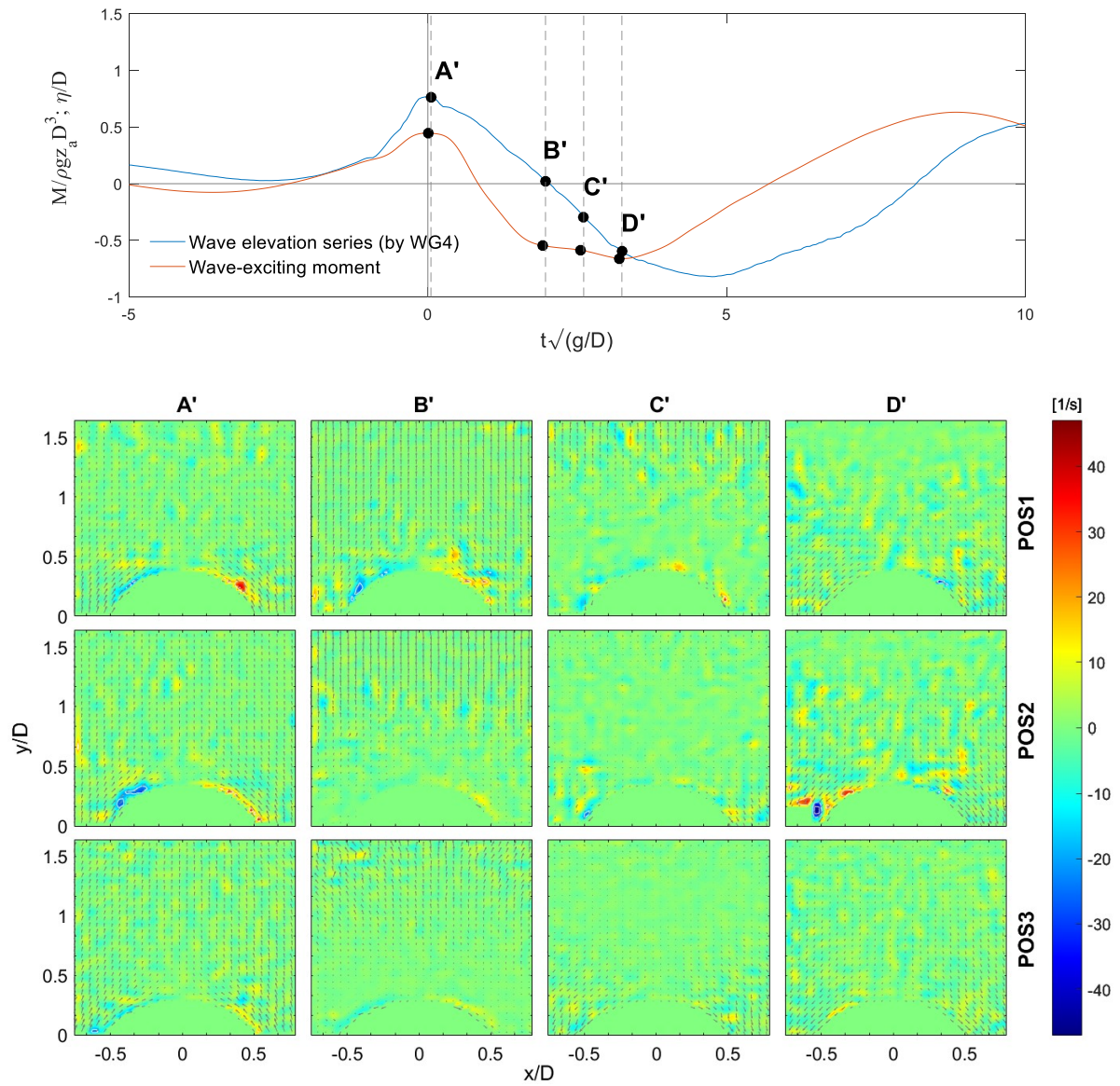


Figure 33. SLC dynamics for case 2.1. Top panel: Time histories of wave elevation (in blue) and wave-exciting moment (in red). Bottom panel: Evolution of the vorticity at times (A'-D') significant for the SLC, and at horizontal planes (POS1-POS3). Incident flow from bottom to top.

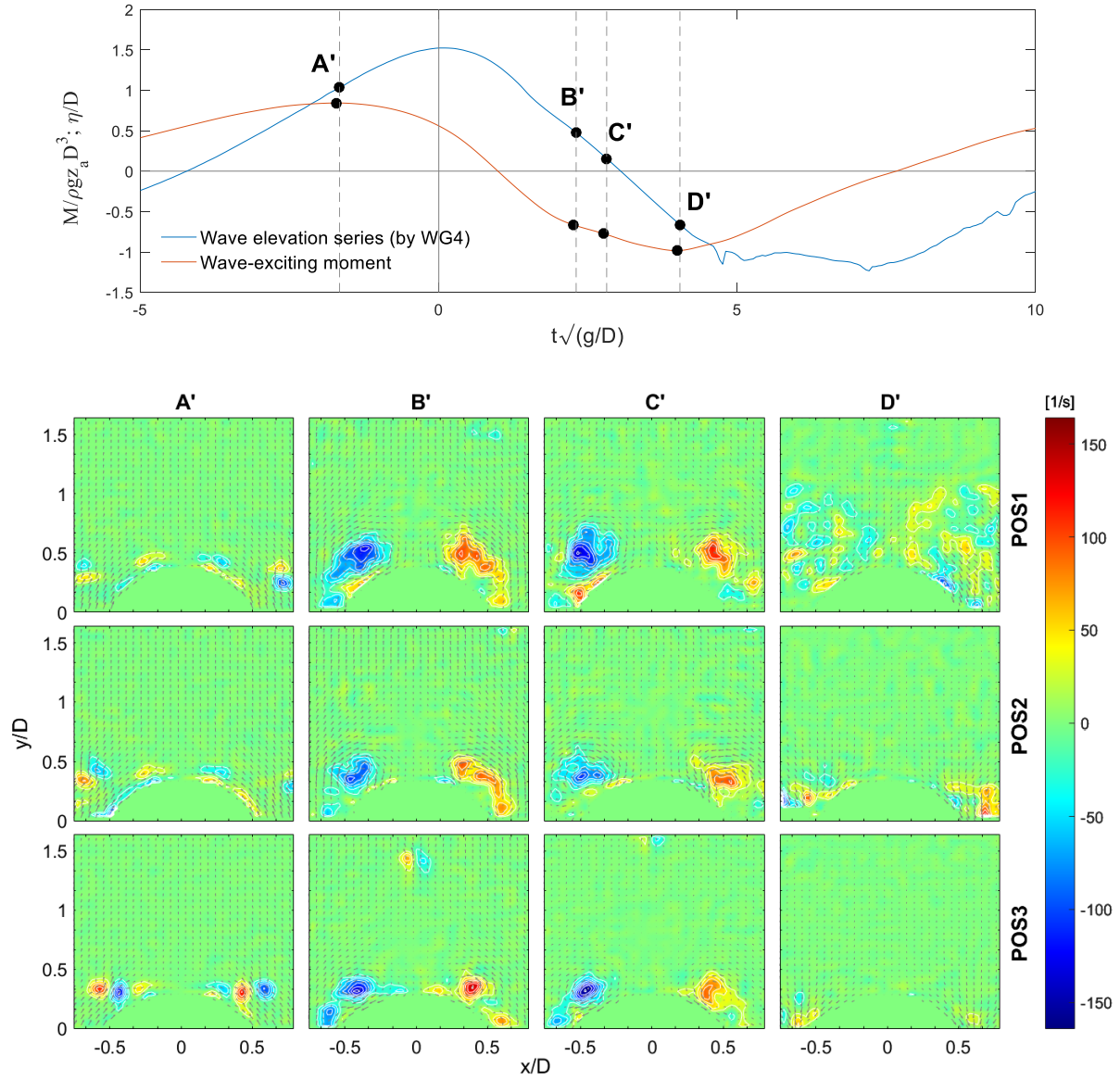


Figure 34. SLC dynamics for case 3.1. Top panel: Time histories of wave elevation (in blue) and wave-exciting moment (in red). Bottom panel: Evolution of the vorticity at times (A'-D') significant for the SLC, and at horizontal planes (POS1-POS3). Incident flow from bottom to top.

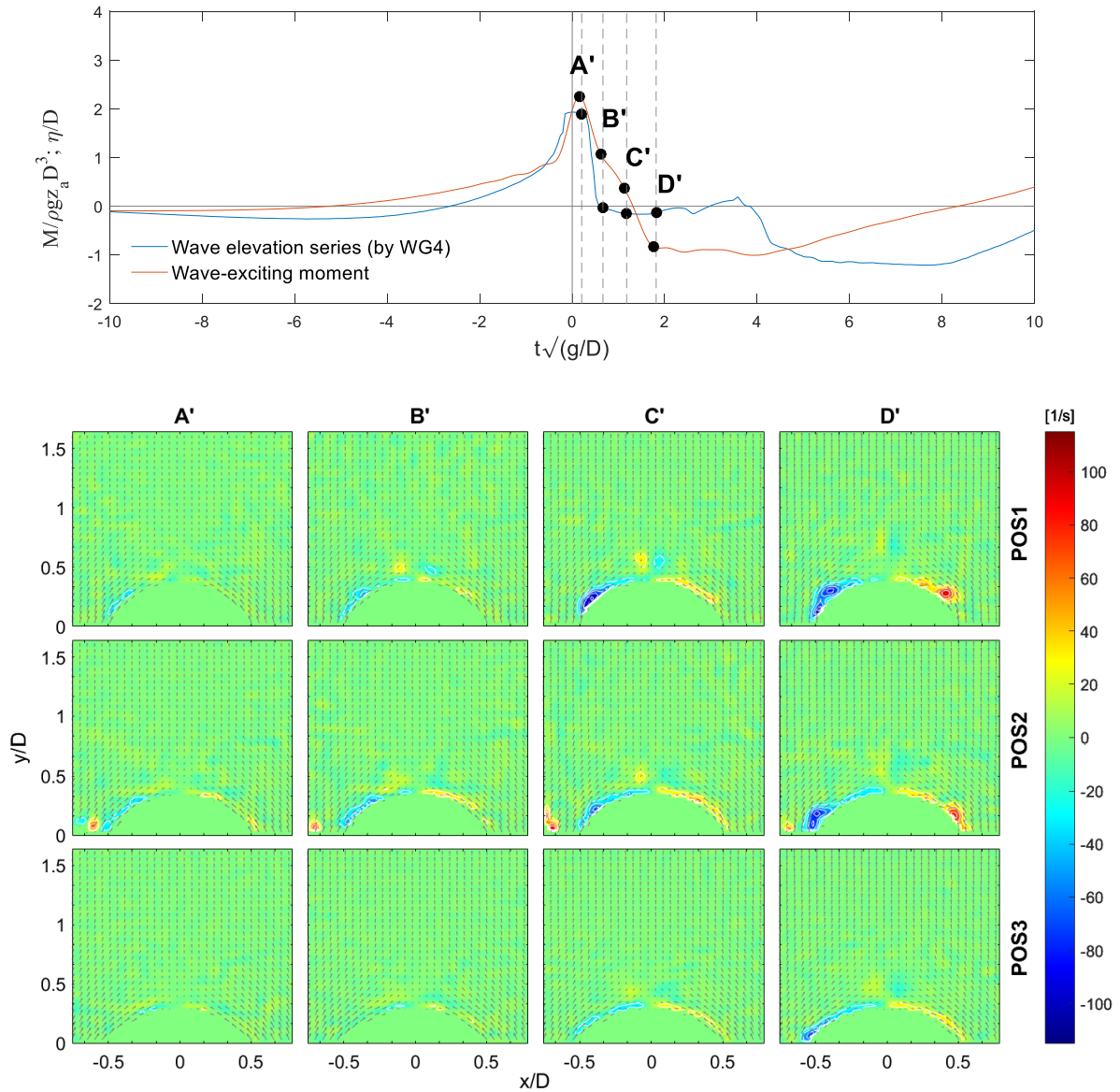


Figure 35.. SLC dynamics for case 4.1. Top panel: Time histories of wave elevation (in blue) and wave-exciting moment (in red). Bottom panel: Evolution of the vorticity at times (A'-D') significant for the SLC, and at horizontal planes (POS1-POS3). Incident flow from bottom to top.

5.5 Vortex-induced force evaluation

To provide better insights into the relationship between the SLC occurrence and the various forms of vorticity patterns observed at its rear side, a further analysis has been conducted. Analytical formulations typically used within the bluff-body Vortex-Induced-Vibration (VIV) community have been applied to evaluate the instantaneous force directly exerted by the fluid, in particular in the form of vortical structures, on the cylinder.

The goal is to compute the force from the vorticity fields derived by PIV images and compare it with the size of the SLC, to assess if vorticity may be responsible for the SLC.

The determination of the force induced by the rise of complex patterns of vortices surrounding a bluff body under oscillating flow commonly requires the knowledge of the pressure and shear stress on the surface of the body. However, these measurements are hard to be obtained experimentally, and also numerically the force estimation method based on the pressure is difficult to apply because of the need to resolve the boundary layers.

In the last decades, the advent and the increasing development of optical measurements techniques (Digital Particle Imaging Velocimetry, DPIV) drove the VIV-community to make many efforts to correlate the observed trajectories of vortices and the measured force on the body starting from velocity and vorticity fields. Among these, a pioneering work is that of Noca (1996) which, starting from the control-volume approach for momentum conservation and through some algebraic manipulations used to eliminate the pressure term, attained an exact formulation for the calculation of unsteady forces in incompressible, viscous and rotational flows, which relies only on the flow field in a finite, arbitrarily chosen region enclosing the body. The general formulation is composed by a volume integral and a surface integral, plus a third term describing the unsteady motion of the body surface:

$$\mathbf{F} = -\frac{1}{N-1} \frac{d}{dt} \int_V \mathbf{x} \times \boldsymbol{\omega} dV + \oint_S \mathbf{n} \cdot \boldsymbol{\Theta} dS - \frac{1}{N-1} \frac{d}{dt} \oint_{S_b} \mathbf{x} \times (\mathbf{x} \times \mathbf{u}) dS \quad (5.4)$$

where N is the dimension of the space under consideration ($N=2$ in a two-dimensional space), \mathbf{x} is the position vector and $\boldsymbol{\omega}$ is the vorticity field derived from PIV measurements, \mathbf{u} is the body velocity and $\boldsymbol{\Sigma}$ is the manipulated stress tensor where the viscous stress tensor appears (Noca et al., 1997). Assuming that the surface integral contribution is negligible (Lin and Rockwell, 1996) and the cylinder is fixed, for the present two-dimensional problem Equation (5.4) can be reduced to:

$$\mathbf{F} = -\frac{d}{dt} \int_V \mathbf{x} \times \boldsymbol{\omega} dV \quad (5.5)$$

where V has been here taken as the entire investigated field of view on which \mathbf{x} and $\boldsymbol{\omega}$ are respectively the coordinates and the vorticity field given on a regular grid with spacing $dx=dy=0.0016$ pixels, corresponding to 1.6mm, whose orientation can be seen in Figure 27. The time interval between frames is $dt=0.001$ sec, being the image acquisition frequency set to 1000 Hz.

Application of Equation (5.5) to the same time-sequences of images considered in the previous analysis, led to a highly fluctuating force signal. Fluctuations are likely due to the noise introduced by the time derivative term when considering the vorticity in the boundary layer, as recognized by Noca et al. (1997).

We overcame this problem by referring to the formulation, free of pressure term and of time derivation, proposed in the innovative work of Wu et al. (2007). Under the same assumptions of above and neglecting the surface integral terms, since the boundary integral was observed to decay quickly with the increase of the integration domain (Wu et al., 2007; Fiabane et al., 2011), the final force formulation reads in two dimensions:

$$\mathbf{F} = -\mu \int_V \mathbf{x} \times \nabla^2 \boldsymbol{\omega} dV \quad (5.6)$$

where μ is the fluid dynamic viscosity and $\nabla^2 \boldsymbol{\omega}$ is the Laplacian operator, that in two-dimensional space is expressed as:

$$\nabla^2 \boldsymbol{\omega} = \nabla \cdot \nabla \boldsymbol{\omega} = \left(\frac{\partial^2 \boldsymbol{\omega}}{\partial x^2} + \frac{\partial^2 \boldsymbol{\omega}}{\partial y^2} \right) \quad (5.7)$$

The recalculation of the force exerted by vorticity on the cylinder by using Equation (5.7) provided less fluctuating and more interpretable force timeseries. A ten-point moving average filter was further applied to screen fluctuations and to obtain a smoother force trend.

The evaluation of the vortex-induced force through Equation (5.7) has been performed for all wave cases, for the same positions whose were object of analysis in the previous paragraphs 0 and 5.4. The calculated force results decomposed on the two-dimensional domain in a transversal drag force component, F_{Dx} and an inline drag force component, F_{Dy} . These forces are put in comparison with the total force measured on the cylinder.

Some significant times have been selected, around the times at which peaks of the calculated force components are observed and around the times of the secondary load cycle occurring.

In particular, the characteristics of the vortex induced force timeseries be described by:

- The time, just prior the maximum measured force, at which first positive peak of the calculated force components is observed, A”;
- The time corresponding to the maximum measured force, B”;
- The time at which vortices start developing, C”;
- The time corresponding to the secondary load cycle, D”;
- The time of the flow inversion, E”.

It is noted that these times are different from the others used for the analysis in previous paragraphs 5.3 and 5.4. At these times, the related vorticity maps have been reported for a complete overview of the problem. Calculated force components and vorticity maps are shown for all the investigated positions (POS1-POS3), thus adding the information of the vertical distribution of the vorticity-exerted-force in relation to the pattern of vortices generating it.

The data provided in such form will help clarify if and when vortices may affect the global force acting on the cylinder, eventually giving rise to the SLC phenomenon, and under what vorticity patterns it occurs.

According to the criteria previously used, only one representative case among similar ones is reported, for the sake of brevity. Thus, again, cases 1.1 and 2.1 were chosen as representative also of cases 1.2 and 2.3, respectively. In the shown graphs, all forces F have been normalized by $\rho g D^3$, while the time t by $\sqrt{g/D}$.

An objective description of the calculated forces trend at the various positions together with the concurrent vorticity pattern is provided, also in comparison with measured force.

Case 1.1, of a strong spilling wave, represented a case in which both vortex generation and SLC occurred. For this wave event, and analogously for the case 1.2, the inline and transversal force components F_{Dx} and F_{Dy} present a first positive peak at time A'', corresponding to an instant just prior the maximum measured force, due to the incoming wave passage (Figure 36). This peak is observable at all horizontal levels, but no correlation with an organized form of vorticity is seen, being the vorticity very weak and limited to the cylinder boundary layer. After an interval of null values of force (except for POS2) nearby the maximum measured load (B''), the magnitude of both F_{Dx} and F_{Dy} starts rising again from time C'', at which some vorticity is clearly present in the boundary layer. The positive peaks of the inline and transversal force are reached at time D'', which identifies the peak of the SLC. At this stage, as also deeply investigated in section 5.4, the lateral symmetrical vortices, close to the cylinder, are completely developed and reach their maximum size. At POS1 and POS2 the concurrent magnitude of F_{Dx} and F_{Dy} is very similar, this meaning that the vortex-induced force acts equally in the two directions, likely due to the circular shape of the vortex. Differently, at POS3, no vortex is evident, the calculated inline force is about null whereas the transversal one assumes a positive magnitude comparable to that of the upper levels. Subsequently, F_{Dx} and F_{Dy} turn to negative values, as a result of the inversion of the flow, at which vortices break-up.

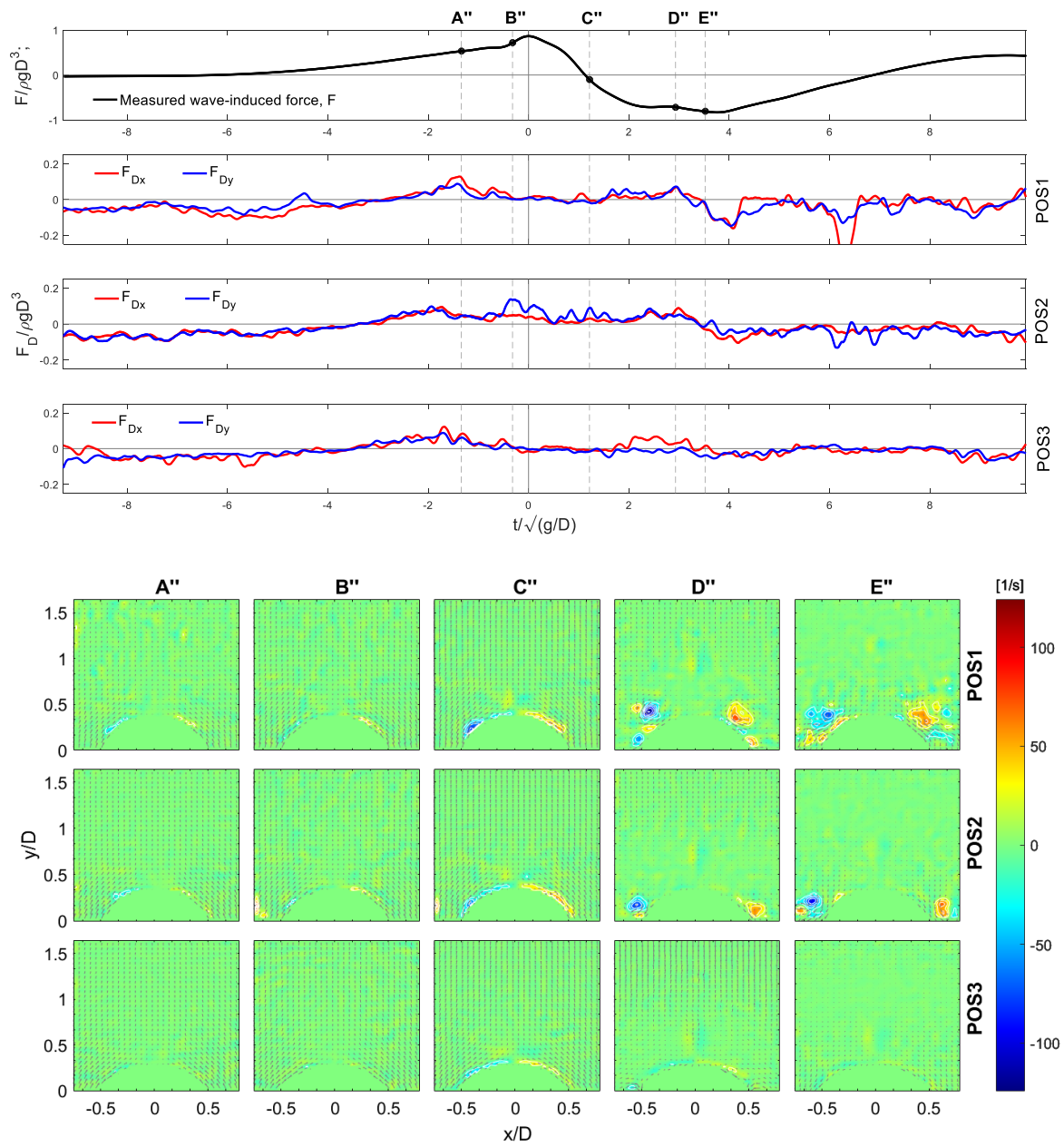


Figure 36. Vortex-induced force evaluation for case 1.1. Top panel: Time histories of measurement wave-induced force on the cylinder (in black) and calculated transversal (in red) and inline (in blue) drag force components induced by vorticity, at the elevations corresponding to horizontal planes (POS1-POS3). Bottom panel: evolution of the vorticity at significant times (A''-E''), and at horizontal planes (POS1-POS3). Incident flow from bottom to top.

The same description is valid also for case 4.1, representing the plunging breaking wave event (Figure 37), for which an evolution very similar to that of case 1.1 is found. However, the peak magnitude of the inline and transversal force contributions at the SLC stage is higher than in case 1.1. Furthermore, focusing on the vorticity maps D'' at POS3, some lateral vortices are partially visible, indicating that the vortices are driven upstream at this elevation. This might explain the positive values of F_{Dx} despite of the slightly negative of F_{Dy} , observed also for case 1.1.

A very similar trend is seen also for the case of very steep, non-breaking wave represented by case 3.1 (Figure 38). Although the calculated force timeseries present more oscillations than the previously discussed cases, clearly due to the more intense and complex vorticity patterns, completely different from the previous cases, most of the above-mentioned characteristics are recognized. A first positive peak of the inline and transversal force components occurs at time A'', always just prior to the maximum measured load, even if no vortices are seen at the different elevations. Positive values of F_{Dx} and F_{Dy} are found also at B, in correspondence of the maximum load, just at the POS2 level, for which significant positive values are found up to time D'', differently from what happens at the upper level where forces are very close to zero. However, vortices are clearly distinguishable at this stage, although differences in configuration and intensity of the vorticity are seen among levels (the intensity of vortices decays from lower to upper positions). The magnitude of F_{Dx} and F_{Dy} is generally significant (with reference to SLC scale), in particular at levels POS2 and POS3, as a reflection of the still strong intensity of the vortex formation at lower positions. A slight growth of F_{Dx} and F_{Dy} can be seen in correspondence of the SLC (E''), before turning to negative values at the complete inversion of the flow.

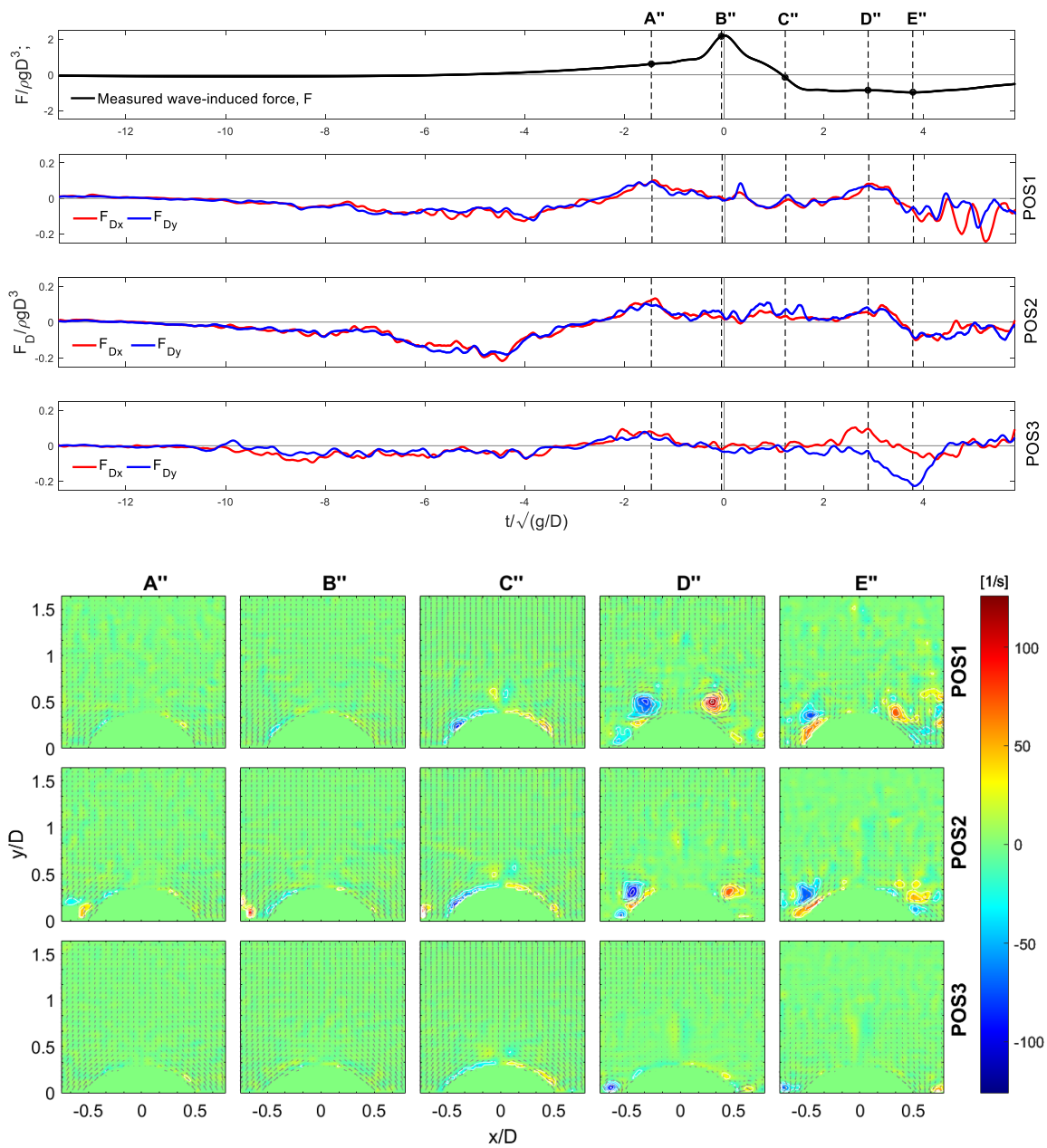


Figure 37. Vortex-induced force evaluation for case 4.1. Top panel: Time histories of measurement wave-induced force on the cylinder (in black) and calculated transversal (in red) and inline (in blue) drag force components induced by vorticity, at the elevations corresponding to horizontal planes (POS1-POS3). Bottom panel: evolution of the vorticity at significant times (A''-E''), and at horizontal planes (POS1-POS3). Incident flow from bottom to top.

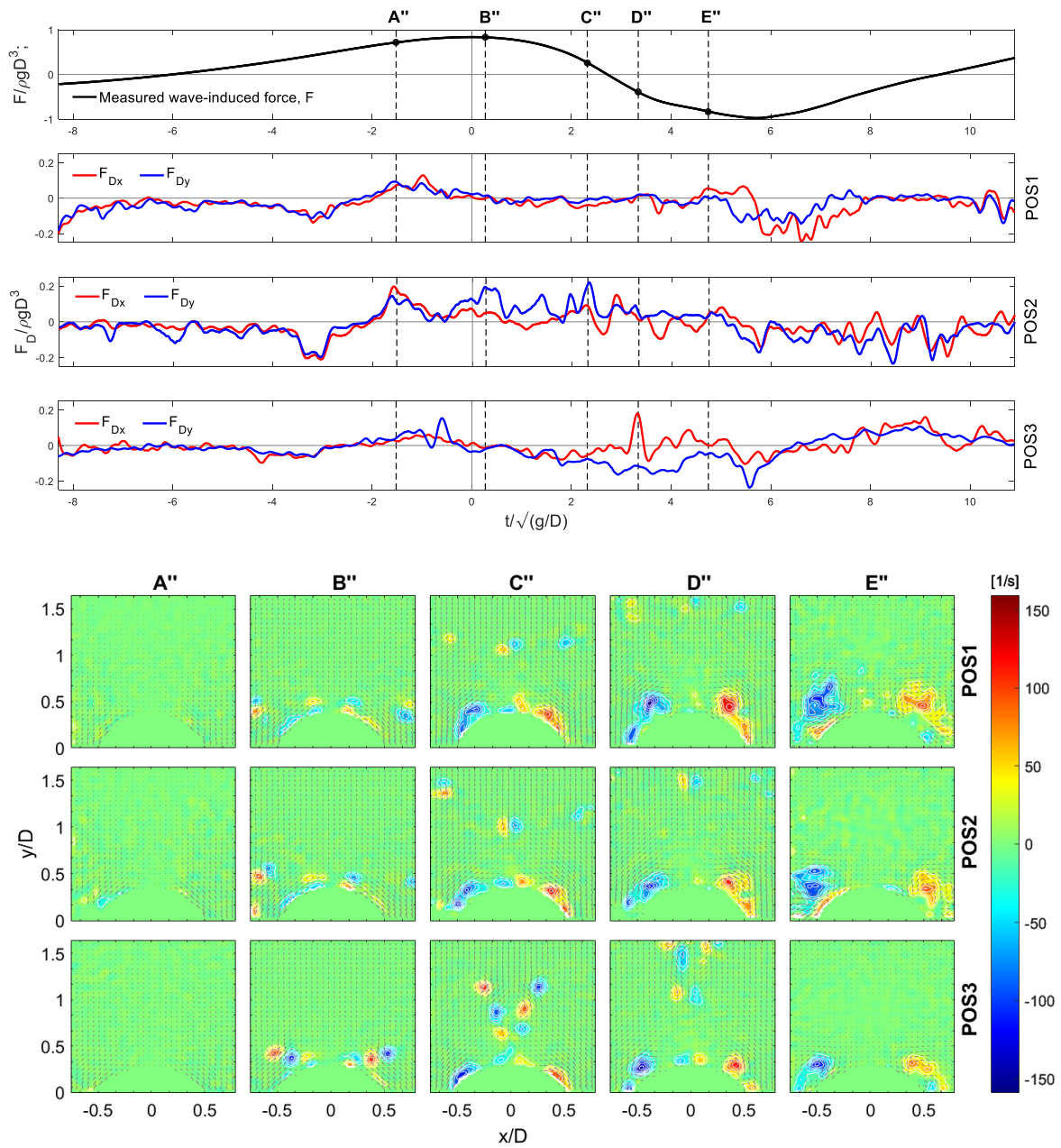


Figure 38. Vortex-induced force evaluation for case 3.1. Top panel: Time histories of measurement wave-induced force on the cylinder (in black) and calculated transversal (in red) and inline (in blue) drag force components induced by vorticity, at the elevations corresponding to horizontal planes (POS1-POS3). Bottom panel: evolution of the vorticity at significant times (A''-E''), and at horizontal planes (POS1-POS3). Incident flow from bottom to top.

Case 2.1, describing a weak spilling breaking wave, has been seen to present SLC and no vortex formation, as well as case 2.3. However, it is characterized by a trend similar to that of the previous cases, notwithstanding the absence of vortex generation. Positive values of the force components F_{Dx} and F_{Dy} are between time A'' and D'', recognizing evident peaks very close to the maximum measured force (A'') and at the SLC occurrence (D''). No distinct vortices are found at any positions, but high vorticity appears in the boundary layer, while some weaker vortical patterns are sparse over the entire domain.

At last, Case 3.3 (mildly steep non-breaking wave) presents positive magnitude of the inline and transversal force components both just before the peak of the measured force (A''), with exception of POS3, and just before the minimum load (D''), approximately where the SLC generally appears. However, a SLC was not observed in this case, although the drag force components reach magnitudes higher than the forces calculated for the other cases. From stage C'' to D'', in fact, vortices attached to the cylinder are clearly developed at all levels, recalling in shape and location what observed in case 3.1. Vortices break-up at the inversion of the flow, except at POS3 where are still visible at time E'', confirming higher intensity of vorticity at lower levels.

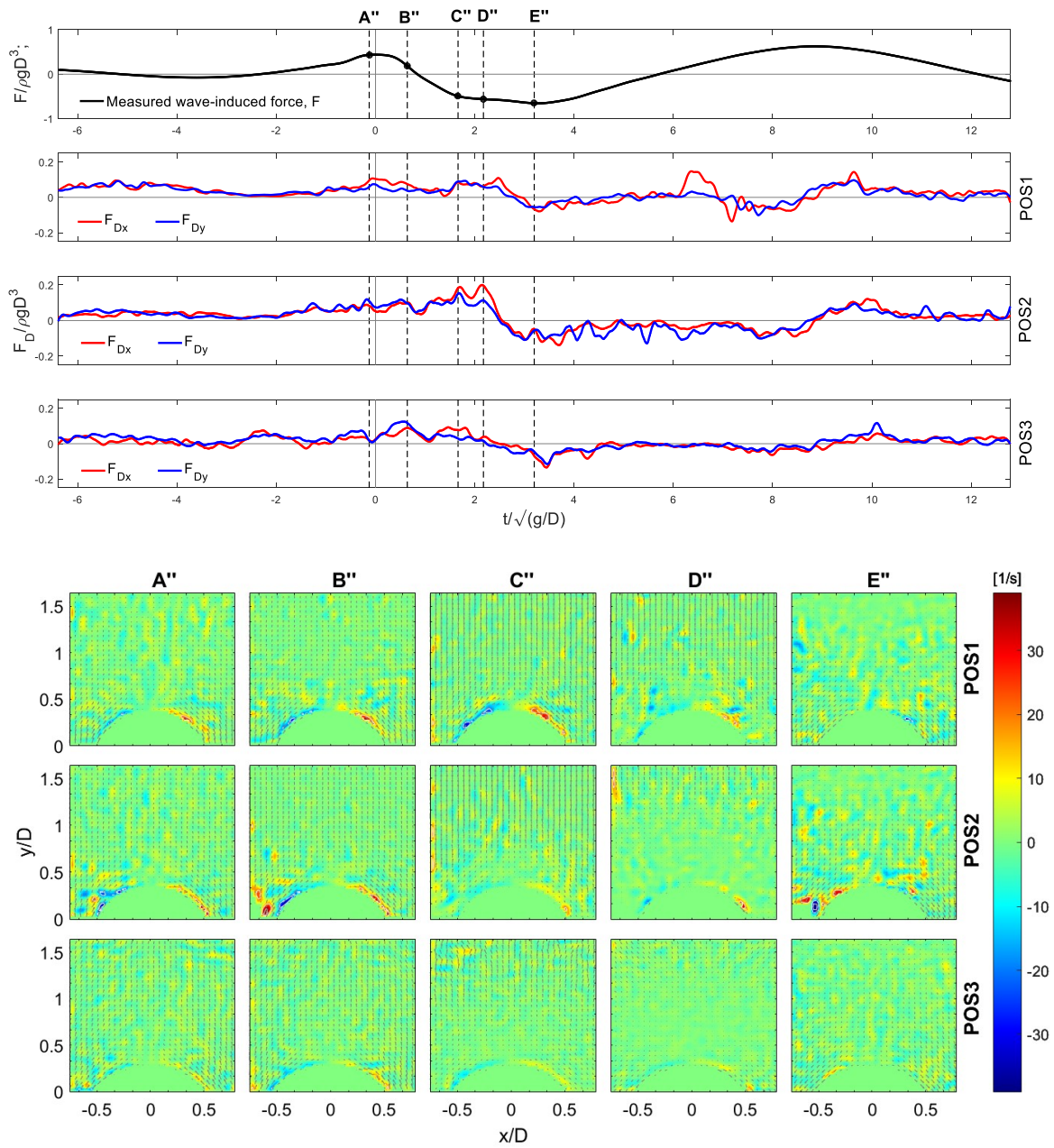


Figure 39. Vortex-induced force evaluation for case 2.1. Top panel: Time histories of measurement wave-induced force on the cylinder (in black) and calculated transversal (in red) and inline (in blue) drag force components induced by vorticity, at the elevations corresponding to horizontal planes (POS1-POS3). Bottom panel: evolution of the vorticity at significant times (A''-E''), and at horizontal planes (POS1-POS3). Incident flow from bottom to top.

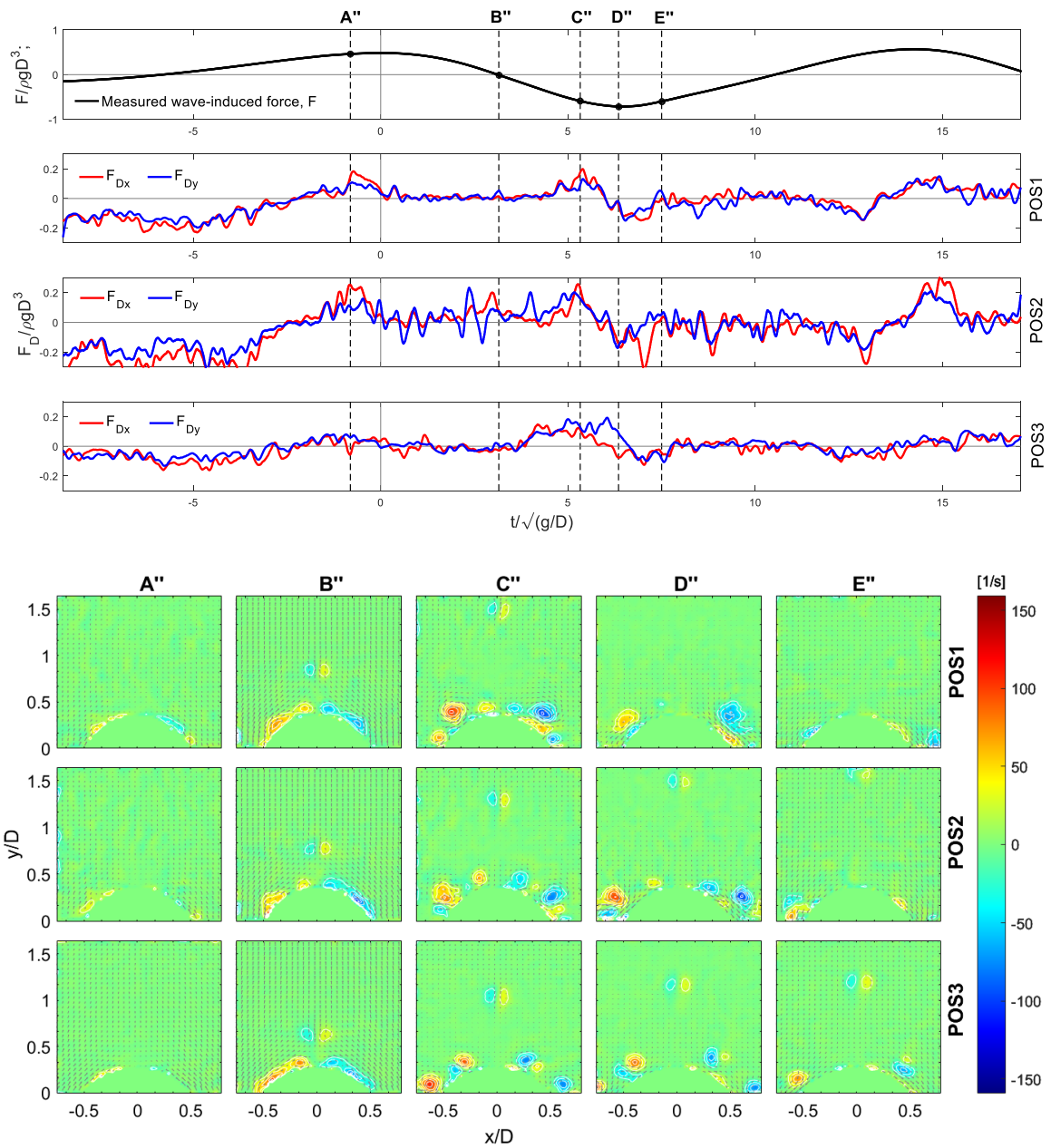


Figure 40 Vortex-induced force evaluation for case 3.3. Top panel: Time histories of measurement wave-induced force on the cylinder (in black) and calculated transversal (in red) and inline (in blue) drag force components induced by vorticity, at the elevations corresponding to horizontal planes (POS1-POS3). Bottom panel: evolution of the vorticity at significant times (A''-E''), and at horizontal planes (POS1-POS3). Incident flow from bottom to top.

5.6 Discussion

In light of the results above, the content of Table 2 has been re-organized into Table 3. Furthermore, the average period T_{av} has been expressed in the dimensionless form $T_{av}^* = T_{av} \sqrt{g/D}$ and columns *VG* and *SLC*, respectively Vortex Generation and Secondary Load Cycle, have been added to indicate the presence or absence of the two investigated phenomena.

Starting from the observation of the SLC, its identification has been provided from the measurements of some flow features, widely recognized in literature. For all the cases characterized by SLC, the typical time of occurrence at one quarter wave period later than the main peak and a duration evaluated as about 15% of the wave period was found, in agreement with Grue and Huseby (2002).

In our experiments, the SLC is observed for all the investigated cases, except one, case 3.3, which shows a very weak loading cycle. Considering some recognized governing parameters for the SLC and its effects (already reported in section 2.3.2.1), the SLC is found for waves characterized by a Froude number $Fr > 0.6$, a dimensionless wave slope $k\eta_c > 0.25$ and wave number $kR > 0.10$. The Keulegan-Carpenter number is in the range 5.3-13.8 for these tests, but it does not seem to govern solely the occurrence of phenomenon. These evidences are in agreement with the limits reported in literature of the observation of pronounced secondary cycle for $Fr > 0.4$ (and some weak events for $Fr \sim 0.35$) and for $k\eta_c > 0.3$ and kR in the range 0.1-0.33, as described by Grue and Huseby (2002), and further confirmed by other experiences (Chaplin et al., 1997; Suja-Thauvin et al., 2017; Riise et al., 2018b). In the present experiments, the SLC ratio spans over the range 0.03-0.05, related to case 3.1 (where it is less evident) and 1.1 (where it is more evident), respectively. These magnitudes are lower than what observed in other works, for which SLC values between 8-12% of the peak-to-peak load were estimated.

Vortical flow structures are seen to evolve for a Keulegan-Carpenter number (KC) in the range 6-14, while the Reynolds number (Re) is in the range $1.7-4.8 \times 10^4$ (as reported in Table 2). No vortex generation is observed for cases 2.3 and 2.1, characterized by $KC < 6$.

In the attempt to shed some light on the role of some wave parameters in the generation of vortices and in the eventual connection with the SLC occurrence we make some considerations based on the observation of the experimental results.

The appearance of vortical structures, where present, is left-right symmetrical and occurs approximately at an angle of ± 60 degrees of the wave propagation, in agreement with observations by Sumer and Fredsøe (2006). The symmetry of vortex formation for $KC > 6$ observed in the experiments seems to be in contrast with the limits for KC intervals reported in Sumer and Fredsøe (2006) for $Re = 10^3$, for which a loss in asymmetry of vortical structures should be observed already for $KC > 4$. This seems to suggest that an increase in Re leads to flow dynamics typical of a smaller KC number, i.e. more stable and with more coherent structures.

On the basis of the dimensionless average period, T_{av}^* , a new classification for the wave cases has been provided in Table 3. The observation of the test matrix suggests that waves of long period, that is T_{av}^* in the range 13-16, are characterized by vortex generation, whereas the shorter waves, represented by cases 2.1 and 2.3, for which $T_{av}^* \sim 0.8$, do not display vortex generation. Furthermore, the wave slope $k\eta_c$ can also be used to characterize the vortex formation: vortex generation occurs for the long waves with $k\eta_c > 0.13$, but not for the short waves with $k\eta_c > 0.4$; while a SLC is always observed for $k\eta_c > 0.25$. Concurrently, the short waves represented by case 2.1 and 2.3 are characterized by higher values of kR than the other group ($kR = 0.29$).

Although all these parameters seem to influence the vortex generation and its connection with the SLC, no strong evidence of which one is dominant over the other for the vortex shedding is proven. Any considerations thus pertain solely to our test matrix that, being fairly limited, does not allow an objective interpretation and generalization.

Concerning again on the observed vorticity pattern, it is worth mentioning again the vorticity associated with case 3.1. The vortex dynamics appears completely different from that found for wave having similar parameters, like for example case 1.1. It has to be kept in mind that case 1.1 is a strong plunging breaking wave, while case 3.1 consists in a very steep, non-breaking wave, so energy dissipation due to breaking may play a role. Differently from similar waves, the vortex formation involved the fluid at lower levels, with small vortices arising in greater number with a frequency much higher than the wave

frequency. It means they are nonlinear, by definition, and this issue will be object of further investigation.

An attempt to clarify the relationship between the shed vorticity and hydrodynamic loads were conducted with the application of Equation (5.6) by Wu et al. (2007), which proposes the calculation of force induced by vorticity from PIV fields (see section 5.5). The results of the application confirmed what observed till now in terms of secondary load occurrence and vortex formation. In particular, for cases 1.1, 1.2, 4.1 and 3.1, the force arising from vortex formation may explain the presence of the SLC, being the magnitude of the calculated force at that stage very close to that of the SLC. In general, the magnitude of the force induced by vortices on the cylinder at the time of SLC occurrence is estimated to be around 8-15% of the maximum measured force.

Otherwise, the absence of a SLC for case 3.3, even though the vortex dynamics is developed and generates a force close to the minimum measured load, might be explained by assuming that the vortex formation produces a significant force that does not solicit the cylinder at the frequency at which the SLC is commonly reconduced. To investigate this, a frequency analysis of the force signal could be useful. Again, this is not evident for the other cases (2.1 and 2.3) where no vortices are observed.

In short, it is observed that the main features of the SLC are in agreement with the range of limits provided by previous experiences in literature (Chaplin et al., 1997; Grue, 2002a; Suja-Thauvin et al., 2017; Riise et al., 2018b). The experiments show that the vortex generation and the SLC are correlated for our test matrix. Vortex generation may occur with or without provoking the SLC and viceversa. The vorticity arising downstream close to the cylinder may be responsible of the secondary load occurrence, but it cannot be the single cause.

With a broader look at the problem of the contribution of vortical structures to the excitation of high-order wave forces that may lead to high-frequency ringing response in strong wave events, the experimental evidence has been compared with the recent CFD-computations by Paulsen et al., 2014a and Kristiansen and Faltinsen (2017).

The vortex generation measured in the present experiments is smaller than that obtained for intermediate water depths by Kristiansen and Faltinsen (2017), who got a vortex core

of diameter comparable to the cylinder radius. Analogously, the diameter of the vortices attached to the cylinder in the simulations of Paulsen et al., 2014a, induced by breaking wave effects, was 65% of the cylinder radius. They associated the SLC to the formation of a downstream vortex (from the interaction between the incoming and return flow) and ascribed it to the modelled free surface flow separation effect.

Vortices observed in the present experiments achieve a maximum extension of about 20%-35% of the cylinder radius. With reference to the causes of the vortex generation measured, looking at the PIV results, this would seem induced at the wall boundary layer of the cylinder, more than by the free surface flow separation, as claimed by Paulsen et al., 2014a. However, with the aim to investigate the nonlinear high frequency forces driving the ringing response under extreme wave events, included steep waves impact, originating either from the flow separation, free surface gravity waves or a combination, a further comparison was made. The experimental data were compared with those provided by Riise et al. (2018b) according to some local wave proxies, i.e. the dimensionless wave period and the local wave slope (see Figure 41). The line $Fr=0.4$ was introduced as reference of the gravity wave effect at the scale of the cylinder diameter, while the dashed line $KC=0.5$ indicates the lower limit of flow separation and contribution of possible drag forces. Most of the events of the present study are placed in the region where the Keulegan-Carpenter number exceeds $KC>0.5$, indicating that possible flow separation effects contribute to the ringing responses. Only exceptions could be considered the borderline cases 2.1 and 2.3. Similarly, data except case 3.3, lie in the region of $Fr>0.4$ indicating the surface gravity wave effects at the scale of the cylinder diameter (Grue et al., 1993). The occurrence of SLC and ringing response coincide, but an open research question remains whether one of the effect is dominant over the other or if they equally contribute.

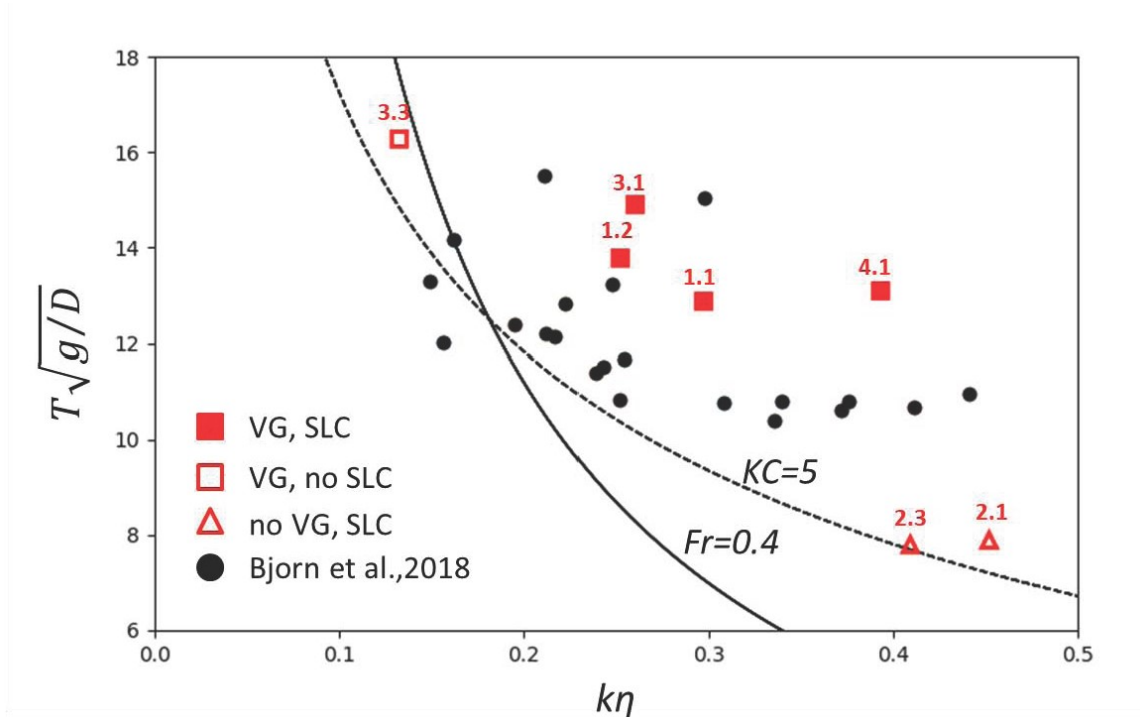


Figure 41. Extreme response events identification. Experimental data (red markers) and data by Riise et. al, 2018 (black dots). Open square: vorticity generation occurrence with no SLC (case 3.1). Filled square: vorticity generation and SLC (cases 1.1, 1.2, 3.1, 4.1). Open triangle: no vorticity, presence of SLC (cases 2.1, 2.3). Dashed line: $KC=0.5$. Continuous line: $Fr=0.4$. Adapted from Fig. 10d by Riise et al. (2018b).

Cases	Description	<i>VG</i>	<i>SLC</i>	η_c (cm)	T_{tt} (s)	T_f (s)	T_{av}^* (s)	$k\eta_c$	kR	KC	Fr
3.3	Mildly steep non-br.	Y	N	5.39	1.24	1.28	16.3	0.13	0.074	6.0	0.37
1.2	Strong spilling br.	Y	Y	7.63	1.07	1.08	13.8	0.25	0.10	8.8	0.64
1.1	Strong spilling br.	Y	Y	7.98	0.99	1.02	12.9	0.30	0.11	9.4	0.73
3.1	Very steep non-br.	Y	Y	9.21	1.12	1.20	14.9	0.26	0.085	10.7	0.72
4.1	Plunging br.	Y	Y	11.3	0.98	1.07	13.1	0.39	0.10	13.8	1.05
2.3	Weak spilling br.	N	Y	4.30	0.61	0.63	7.8	0.41	0.29	5.3	0.67
2.1	Weak spilling br.	N	Y	4.70	0.59	0.63	7.9	0.45	0.29	5.7	0.75

Table 3. Reorganized parameters of the tested waves in light of results available: η_c surface elevation at the crest measured by WG4, T_{tt} trough-to-trough period, T_f zero up-crossing period of the force history, T_{av}^* dimensionless average period, L wave length, k wave number, $k\eta_c$ wave slope, kR dimensionless wave number (with respect to the cylinder radius), Re Reynolds number, KC Keulegan-Carpenter number and Fr Froude number. VG means Vortex Generation, while SLC secondary load cycle, whose presence is indicated by ‘Y’(yes) or ‘N’ (no).

Chapter 6

CONCLUSIONS

This thesis finds its main motivation in the need of increasing the knowledge on high-order, nonlinear wave forces acting on vertical slender cylinders typically used as support for offshore platforms and wind turbines. These forces are at the origin of wave-induced high frequency structural vibrations, such as the *ringing*, that often threatens the safety of offshore structures.

An investigation of the dynamic processes arising at a bottom-hinged, surface-piercing, vertical, slender cylinder exposed to steep waves, breaking and non-breaking, in deep waters has been experimentally conducted. Specific focus is on the causes of occurrence of the *secondary load cycle* and the possible links with the flow separation and the vortex formation that occur at the lee side of the cylinder. These issues are still not properly known and the research community is currently active on this topic. In such perspective, a main setup dedicated to Particle Image Velocimetry (PIV) investigation of the flow downstream the cylinder over four horizontal planes parallel to the bottom at different elevations has been undertaken. The setup allowed also to record the incident wave elevation at the cylinder and to measure the wave-exciting moment on the cylinder, induced by seven cases of steep waves, both breaking and non-breaking. The novelty of this experimentation is constituted by the complex setup arrangement, that joins use of many different experimental measurement techniques at the same time. This increases the information acquired about the phenomenon and is the experimental demonstration of the relationship between vortex-induced force and SLC.

The analysis of the PIV results, in the form of vorticity maps superposed to the related velocity fields, showed the occurrence of flow separation and formation of vorticity pattern for all the breaking waves, with the exception of weak spilling breakers (cases 2.1 and 2.3), and of the non-breaking waves, but with a completely different scenario. In particular, the vortex generation by the non-breaking event 3.1 appears to be constituted by many small vortical structures and the vorticity reached also the lowest investigated level. A strong nonlinearity is recognized for this vortex dynamics, having observed a frequency of vortex creation much higher than wave frequency. This needs to be investigated more in depth. On the contrary, the vorticity generated by the strong spilling breaking wave 1.1 follows a simple pattern, with vorticity mainly generated laterally to the cylinder in the form of a symmetrical pairs of vortices, that decrease in size and intensity, with depth. This suggests that the vortices, which remain very close to the cylinder, have a funnel shape with the minimum size at the lowermost location.

These differences were found despite the wave parameters are similar (Table 3). The observation of the wave parameters leads to establish the occurrence of vortex generation for values of the dimensionless wave slope $k\eta_c$ exceeding 0.13.

A second analysis of the vorticity maps together with the wave-exciting moment has provided important information on the SLC occurrence. Such secondary load has been observed in all cases, but case 3.3 related to mild steep non-breaking waves, for Froude number Fr exceeding 0.4.

Furthermore, secondary load and vortex generation occur together for waves characterized by a dimensionless period $T\sqrt{g/D}$ in the range 13-16, steepness $k\eta_c > 0.25$ and Froude number $Fr > 0.6$. In short, it is observed that the main features of the SLC are in agreement with the range of limits provided by previous experiences in literature (Chaplin et al., 1997; Grue, 2002; Riise et al., 2018b; Suja-Thauvin et al., 2017). The experiments show that the vortex generation and the SLC are correlated for our test matrix. The vortex generation may happen with or without provoking the SLC and viceversa. The vorticity arising downstream close to the cylinder may be responsible of the SLC, but it cannot be the single cause.

In the effort to provide better insights in the relationship between shed vorticity and hydrodynamic loads, the formulation by Wu et al. (2007) (Equation 5.6) has been applied

to PIV results. The formula proposes the calculation of timeseries of the force induced by vorticity from PIV analysed fields (see section 5.5). The results from the application show that vortex generation may be responsible of the occurrence of SLC, but it is not the only cause. In fact, a force of magnitude compared to that of the SLC is observed in correspondence of SLC occurrence for cases 1.1, 1.2, 4.1 and 3.1, differently it is not true for the other cases for which vortices do not induce a SLC (case 3.3) and the SLC appears without distinct vortex formation (cases 2.1 and 2.3). A frequency analysis of the time-history of the calculated force could be useful. In general, the magnitude of the force induced by vortices on the cylinder at the time of SLC occurrence is estimated to be around 8-15% of the maximum measured force.

Furthermore, with a broader look at the problem of the contribution of vortical structures to the excitation of high-order wave forces, which may lead to high-frequency ringing response in strong wave events, the experimental evidence has been compared with the recent CFD-computations by Paulsen et al., 2014a and Kristiansen and Faltinsen (2017). Vortices observed in the present experiments achieve a maximum extension of about 20%-35% of the cylinder radius while those found in the literature have a diameter roughly comparable to the cylinder radius. The causes of vortex generation are investigated by comparing the present data with the extreme response events chart by Riise et al. (2018b). The resulting graph indicates that the occurrence of SLC and ringing response coincide, but the question if the free surface effects or the flow separation effect is dominant or they equally contribute still remains partly unresolved.

An higher-harmonic force components analysis will lead to a better comprehension of the occurrence of SLC in relation to ringing responses, but also to understand which vorticity pattern can be responsible for the SLC and together with what other phenomenon.

References

- Adrian, R. J. (1988). *Laser Anemometry in Fluid Mechanics III: Selected Papers from the Third International Symposium on Applications of Laser Anemometry to Fluid Mechanics, Lisbon, Portugal, July, 1986*, Ladoan, Instituto Superior Técnico, Centro de Termodinâmica Apicada e Mecânica dos Flúidos. Retrieved from <https://books.google.it/books?id=3qBRAAAAMAAJ>
- Babanin, A., Chalikov, D., Young, I., & Savelyev, I. (2010). *Numerical and laboratory investigation of breaking of steep two-dimensional waves in deep water*. *Journal of Fluid Mechanics*, Vol. 644. doi:10.1017/S002211200999245X
- Bachynski, E. E., Kristiansen, T., & Thys, M. (2017). Experimental and numerical investigations of monopile ringing in irregular finite-depth water waves. *Applied Ocean Research*, **68**, 154–170.
- Baldock, T. E., Swan, C., & Taylor, P. H. (1996). A laboratory study of nonlinear surface waves on water. *Philosophical Transactions of the Royal Society of London. Series A: Mathematical, Physical and Engineering Sciences*, **354**(1707), 649 LP-676.
- Banner, M. L., & Peregrine, D. H. (1993). Wave Breaking in Deep Water. *Annual Review of Fluid Mechanics*, **25**(1), 373–397.
- Basco, D. R., & Niedzwecki, J. M. (1989). Breaking Wave Force Distributions and Design Criteria for Slender Piles. *Offshore Technology Conference*, Houston, Texas: Offshore Technology Conference, p. 8.
- Benjamin, T. B., & Feir, J. E. (1967). The disintegration of wave trains on deep water Part 1. Theory. *Journal of Fluid Mechanics*, **27**(3), 417–430.
- Bonmarin, P. (1989). Geometric properties of deep-water breaking waves. *Journal of Fluid Mechanics*, **209**, 405–433.
- Bonmarin, P., & Ramamonjiarisoa, A. (1985). Deformation to breaking of deep water gravity waves. *Experiments in Fluids*, **3**(1), 11–16.
- Brown, M. G., & Jensen, A. (2001). Experiments on focusing unidirectional water waves. *Journal of Geophysical Research: Oceans*, **106**(C8), 16917–16928.
- Chakrabarti, S. K. (1987). *Hydrodynamics of offshore structures*, Computational Mechanics. Retrieved from <https://books.google.it/books?id=Ds1QAAAAYAAJ>

- Chan, E.-S., Cheong, H.-F., & Tan, B.-C. (1995). Laboratory study of plunging wave impacts on vertical cylinders. *Coastal Engineering*, **25**(1), 87–107.
- Chaplin, J. R. (1996). On Frequency-Focusing Unidirectional Waves. *International Journal of Offshore and Polar Engineering*, **6**(02), 7.
- Chaplin, J. R., & Rainey, R. C. T. (2003). Wave breaking and cavitation around a vertical cylinder: Experiments and Linear Theory. In *18th International Workshop on Water Waves and Floating Bodies*. Retrieved from <https://eprints.soton.ac.uk/53841/>
- Chaplin, J. R., Rainey, R. C. T., & Yemm, R. W. (1997). Ringing of a vertical cylinder in waves. *Journal of Fluid Mechanics*, **350**, S002211209700699X.
- Chella, M. A., Collados, X. R., Bihs, H., Myrhaug, D., & Arntsen, Ø. A. (2016). Numerical and Experimental Investigation of Breaking Wave Interaction with a Vertical Slender Cylinder. *Energy Procedia*, **94**, 443–451.
- Chella, M. A., Tørum, A., & Myrhaug, D. (2012). An Overview of Wave Impact Forces on Offshore Wind Turbine Substructures. *Energy Procedia*, **20**, 217–226.
- Chen, X., Molin, B., & Petitjean, F. (1991). Faster evaluation of resonant exciting loads on tension leg platforms. In *Proc. VIII Int. Symp. Offshore Enging.*, p. 114,185-194.
- Chong, M. S., Perry, A. E., & Cantwell, B. J. (1990). A general classification of three-dimensional flow fields. *Physics of Fluids A: Fluid Dynamics*, **2**(5), 765–777.
- Dean, R. G. (1965). Stream function representation of nonlinear ocean waves. *Journal of Geophysical Research*, **70**(18), 4561–4572.
- Eatock Taylor, R., & Chau, F. P. (1992). Wave Diffraction Theory—Some Developments in Linear and Nonlinear Theory. *Journal of Offshore Mechanics and Arctic Engineering*, **114**(3), 185–194.
- Faltinsen, O. M., Newman, J. N., & Vinje, T. (1995). Nonlinear wave loads on a slender vertical cylinder. *Journal of Fluid Mechanics*, **289**(1), 179.
- Fan, X., Zhang, J., & Liu, H. (2018). Numerical analysis on the secondary load cycle on a vertical cylinder in steep regular waves. *Ocean Engineering*, **168**, 133–139.
- Farazmand, M., & Haller, G. (2015). Polar rotation angle identifies elliptic islands in unsteady dynamical systems. *Physica D: Nonlinear Phenomena*, Vol. 315. doi:10.1016/j.physd.2015.09.007
- Fenton, J. D. (1985). A Fifth-Order Stokes Theory for Steady Waves. *Journal of Waterway, Port, Coastal, and Ocean Engineering*, **111**(2), 216–234.
- Fiabane, L., Gohlke, M., & Cadot, O. (2011). Characterization of flow contributions to drag and lift of a circular cylinder using a volume expression of the fluid force. *European Journal of Mechanics - B/Fluids*, **30**(3), 311–315.
- Goda, Y., Haranaka, S., & Kitahata, M. (1966). *Study on impulsive breaking wave forces on*

piles, Vol. 6(5).

- Griffin, O. M., Peltzer, R. D., Wang, H. T., & Schultz, W. W. (1996). *Kinematic and dynamic evolution of deep water breaking waves*. *Journal of Geophysical Research*, Vol. 1011. doi:10.1029/96JC00281
- Grue, J. (2002). On four highly nonlinear phenomena in wave theory and marine hydrodynamics. *Applied Ocean Research*, **24**(5), 261–274.
- Grue, J., Bjørshol, G., & Strand, Ø. (1993). Higher harmonic wave exciting forces on a vertical cylinder, Vol. in Preprin, Matematisk Institutt, Universitetet i Oslo, pp. 1–30.
- Grue, J., Clamond, D., Huseby, M., & Jensen, A. (2003). Kinematics of extreme waves in deep water. *Applied Ocean Research*, **25**(6), 355–366.
- Grue, J., & Huseby, M. (2002). Higher-harmonic wave forces and ringing of vertical cylinders. *Applied Ocean Research*, **24**(4), 203–214.
- Haller, G., Hadjighasem, A., Farazmand, M., & Huhn, F. (2016). Defining coherent vortices objectively from the vorticity. *Journal of Fluid Mechanics*, **795**, 136–173.
- HBM website. (2018). Z6 Bending Beam Load cell. Retrieved from <https://www.hbm.com/en/2701/z6-beam-load-cell/>
- Hemming, S. A. (1996). Second-order wavemaker theory for irregular waves. *Ocean Engineering*, **23**(1), 47–88.
- Holmèn, V. (2012). *Methods for vortex identification*, Lund University, Sweden.
- Honji, H. (1981). Streaked flow around an oscillating circular cylinder. *Journal of Fluid Mechanics*, **107**, 509–520.
- Hua, B. L., & Klein, P. (1998). An exact criterion for the stirring properties of nearly two-dimensional turbulence. *Physica D: Nonlinear Phenomena*, **113**(1), 98–110.
- Hunt, J. C. R., Wray, A., & Moin, P. (1988). *Eddies, stream, and convergence zones in turbulence*. Center for Turbulence Report CTR-88.
- Huseby, M., & Grue, J. (2000). An experimental investigation of higher-harmonic wave forces on a vertical cylinder. *Journal of Fluid Mechanics*, **414**, 75–103.
- Jefferys, E. R., & Rainey, R. C. T. (1994). Slender Body Models of TLP and GBS 'Ringing'. In *Seventh International Conference on the Behaviour of Offshore structures*, Cambridge; MA: Pergamon, pp. 587–606.
- Jensen, A., & Grue, J. (2002). A note on the difference in the speed of gravity waves in a physical and numerical wave tank. *Wave Motion*, **36**(1), 41–48.
- Jensen, A., Sveen, J. K., Grue, J., Richon, J.-B., & Gray, C. (2001). Accelerations in water waves by extended particle image velocimetry. *Experiments in Fluids*, **30**(5), 500–510.
- Jeong, J., & Hussain, F. (1995). On the identification of a vortex. *Journal of Fluid*

Mechanics, **285**, 69–94.

- Jillians, W. J. (1989). The superharmonic instability of Stokes waves in deep water. *Journal of Fluid Mechanics*, **204**, 563–579.
- Johannessen, T. B. (2011). Nonlinear Superposition Methods Applied to Continuous Ocean Wave Spectra. *Journal of Offshore Mechanics and Arctic Engineering*, **134**(1), 11302–11314.
- Kjeldsen, S. P., Tørum, A., & Dean, R. G. (1986). Wave Forces on Vertical Piles Caused by 2- and 3-Dimensional Breaking Waves. *Coastal Engineering 1986*. doi:doi:10.1061/9780872626003.142
- Kjeldsen, S. P., Vinje, T. P., Myrhaug, D. P., & Brdvig, P. P. (1980). Kinematics Of Deep Water Breaking Waves. *Offshore Technology Conference*, Houston, Texas: Offshore Technology Conference, p. 10.
- Kristiansen, T., & Faltinsen, O. M. (2017). Higher harmonic wave loads on a vertical cylinder in finite water depth. *Journal of Fluid Mechanics*, **833**, 773–805.
- Krokstad, J. R., & Solaas, F. (2000). Study of Nonlinear Local Flow. In *The Tenth International Offshore and Polar Engineering Conference*, Seattle, Washington, USA: International Society of Offshore and Polar Engineers, p. 6, vol. 3.
- Krokstad, J. R., Stansberg, C. T., Nestegård, A., & Marthinsen, T. (1998). A New Nonslender Ringing Load Approach Verified Against Experiments. *Journal of Offshore Mechanics and Arctic Engineering*, **120**(1), 20–29.
- Kulite website. (2018). XT-190(M) - Miniature Ruggedized Pressure Transducer. Retrieved from <https://www.kulite.com/products/product-advisor/product-catalog/miniature-ruggedized-pressure-transducer-xt-190-xt-190m-xt-190m-xt-190m-xt-190m-xt-190m/>
- Langen, I., Skjåstad, O., & Haver, S. (1998). Measured and predicted dynamic behaviour of an offshore gravity platform. *Applied Ocean Research*, **20**(1), 15–26.
- Le Méhauté, B. (1969). *An Introduction to Hydrodynamics and Water Waves*. doi:10.1007/978-3-642-85567-2
- Li, J., Wang, Z., & Liu, S. (2014). Experimental study of interactions between multi-directional focused wave and vertical circular cylinder, part II: Wave force. *Coastal Engineering*, **83**, 233–242.
- Lin, J.-C., & Rockwell, D. (1996). Force identification by vorticity fields: techniques based on flow imaging. *Journal of Fluids and Structures*, **10**(6), 663–668.
- Liu, S., Jose, J., Ong, M. C., & Gudmestad, O. T. (2019). Characteristics of higher-harmonic breaking wave forces and secondary load cycles on a single vertical circular cylinder at different Froude numbers. *Marine Structures*, **64**, 54–77.
- Longuet-Higgins, M. S. (1978). The instabilities of gravity waves of finite amplitude in deep water II. Subharmonics. In *Proceedings of the Royal Society of London. A*.

Mathematical and Physical Sciences, Vol. 360, p. 489 LP-505.

- Longuet-Higgins, M. S. (1988). Mechanisms of Wave Breaking in Deep Water. In B. R. Kerman, ed., *Sea Surface Sound: Natural Mechanisms of Surface Generated Noise in the Ocean*, Dordrecht: Springer Netherlands, pp. 1–30.
- Lugt, H. J. (1979). The Dilemma of Defining a Vortex. In U. Müller, K. G. Roesner, & B. Schmidt, eds., *Recent Developments in Theoretical and Experimental Fluid Mechanics: Compressible and Incompressible Flows*, Berlin, Heidelberg: Springer Berlin Heidelberg, pp. 309–321.
- Madsen, O. S. (1986). Hydrodynamic force on circular cylinders. *Applied Ocean Research*, **8**(3), 151–155.
- Malenica, Š., & Molin, B. (1995). Third-harmonic wave diffraction by a vertical cylinder. *Journal of Fluid Mechanics*, **302**, 203.
- Mansard, E. P. D., & Funke, E. R. (1982). A New Approach to Transient Wave Generation. In *Coastal Engineering 1982*, pp. 1–18.
- Marthinsen, T., Stansberg, C. T., & Krokstad, J. R. (1996). On the Ringing Excitation of Circular Cylinders. *The Sixth International Offshore and Polar Engineering Conference*, Los Angeles, California, USA: International Society of Offshore and Polar Engineers, p. 9.
- Matteotti, G. (1995). *Lineamenti di costruzioni marittime*, S.G.E. Retrieved from <https://books.google.it/books?id=B6BQAAAACAAJ>
- Melville, W. K. (1982). The instability and breaking of deep-water waves. *Journal of Fluid Mechanics*, **115**, 165–185.
- Melville, W. K. (1996). The Role of Surface-Wave Breaking in Air-Sea Interaction. *Annual Review of Fluid Mechanics*, **28**(1), 279–321.
- Melville, W. K., & Rapp, R. J. (1988). Experiments on Breaking Waves BT - Sea Surface Sound: Natural Mechanisms of Surface Generated Noise in the Ocean. In B. R. Kerman, ed., , Dordrecht: Springer Netherlands, pp. 39–49.
- Morison, J. R., Johnson, J. W., & Schaaf, S. A. (1950). The Force Exerted by Surface Waves on Piles. *Journal of Petroleum Technology*, **2**(05), 149–154.
- Natvig, B. J., & Teigen, P. (1993). Review Of Hydrodynamic Challenges In Tlp Design. *International Journal of Offshore and Polar Engineering*, **3**(04), 9.
- Newman, J. N. (1996). Nonlinear Scattering of Long Waves by a Vertical Cylinder BT - Waves and Nonlinear Processes in Hydrodynamics. In J. Grue, B. Gjevik, & J. E. Weber, eds., , Dordrecht: Springer Netherlands, pp. 91–102.
- Noca, F. (1996). *On the evaluation of instantaneous fluid-dynamic forces on a bluff body*. Retrieved from <https://core.ac.uk/download/pdf/33115276.pdf>

- Noca, F., Shiels, D., & Jeon, D. (1997). Measuring instantaneous fluid dynamic forces on bodies, using only velocity fields and their derivatives. *Journal of Fluids and Structures*, **11**(3), 345–350.
- Okubo, A. (1970). *Horizontal dispersion of floatable particles in vicinity of velocity singularities such as convergences*. *Deep Sea Research*, Vol. 17. doi:10.1016/0011-7471(70)90059-8
- Osyka, B. (2016). *Violent Wave Slamming in Deep and Intermediate Water*, Universitet i Oslo. Retrieved from <https://www.duo.uio.no/handle/10852/51955>
- Paulsen, B. T., Bredmose, H., Bingham, H. B., & Jacobsen, N. G. (2014a). Forcing of a bottom-mounted circular cylinder by steep regular water waves at finite depth. *Journal of Fluid Mechanics*, **755**, 1–34.
- Paulsen, B. T., Bredmose, H., Bingham, H. B., & Jacobsen, N. G. (2014b). Forcing of a bottom-mounted circular cylinder by steep regular water waves at finite depth. *Journal of Fluid Mechanics*, **755**, 1–34.
- Perlin, M., Choi, W., & Tian, Z. (2013). Breaking Waves in Deep and Intermediate Waters. *Annual Review of Fluid Mechanics*, **45**(1), 115–145.
- Phillips, O. M. (1977). *The Dynamics of the Upper Ocean*, Cambridge: Cambridge University Press. Retrieved from <https://books.google.it/books?id=fYk6AAAAIAAJ>
- Photron website. (2018). Photron FASTCAM S45 datasheet. Retrieved from <https://photron.com/fastcam-sa-5/>
- Raffel, M., Willert, C., & Kompenhans, J. (1998). *Particle Image Velocimetry: A Practical Guide*. doi:10.1007/978-3-662-03637-2
- Rainey, R. C. T. (1989). A new equation for calculating wave loads on offshore structures. *Journal of Fluid Mechanics*, **204**, 295–324.
- Rainey, R. C. T. (2007). Weak or strong nonlinearity: the vital issue. *Journal of Engineering Mathematics*, **58**(1), 229–249.
- Rapp, R. J., & Melville, W. K. (1990). Laboratory measurements of deep-water breaking waves. *Philosophical Transactions of the Royal Society of London. Series A, Mathematical and Physical Sciences*, **331**(1622), 735 LP-800.
- Riise, B. (2009). *Nonlinear kinematics in irregular waves on finite depth*, University of Oslo.
- Riise, B. H., Grue, J., Jensen, A., & Johannessen, T. B. (2018a). A note on the secondary load cycle for a monopile in irregular deep water waves. *Journal of Fluid Mechanics*, **849**, R1.
- Riise, B. H., Grue, J., Jensen, A., & Johannessen, T. B. (2018b). High frequency resonant response of a monopile in irregular deep water waves. *Journal of Fluid Mechanics*, **853**, 564–586.

- Sarpkaya, T. (1976). *In - Line And Transverse Forces, On Cylinders In Oscillatory Flow At High Reynolds Numbers.*, Vol. Naval Post, Monterey, CA.
- Sarpkaya, T. (1986). Force on a circular cylinder in viscous oscillatory flow at low Keulegan—Carpenter numbers. *Journal of Fluid Mechanics*, **165**, 61–71.
- Sawaragi, T., & Nochino, M. (1984). Impact Forces of Nearly Breaking Waves on a Vertical Circular Cylinder. *Coastal Engineering in Japan*, **27**(1), 249–263.
- Schultz, W. W., Huh, J., & Griffin, O. M. (1994). Potential energy in steep and breaking waves. *Journal of Fluid Mechanics*, **278**, 201–228.
- Skjelbreia, L., & Hendrickson, J. (1960). Fifth order gravity wave theory. *Coastal Engineering Proceedings; No 7 (1960): Proceedings of 7th Conference on Coastal Engineering, The Hague, The Netherlands, 1960*. doi:10.9753/icce.v7.10
- Stansberg, C. T. (1997). Comparing ringing loads from experiments with cylinders of different diameters: an empirical study. In *BOSS 97 Conference*.
- Stansberg, C. T., Huse, E., Krokstad, J. R., & Lehn, E. (1995). Experimental Study of Non-Linear Loads On Vertical Cylinders In Steep Random Waves. *The Fifth International Offshore and Polar Engineering Conference*, The Hague, The Netherlands: International Society of Offshore and Polar Engineers, p. 8.
- Su, M.-Y., Bergin, M., Marler, P., & Myrick, R. (1982). Experiments on nonlinear instabilities and evolution of steep gravity-wave trains. *Journal of Fluid Mechanics*, **124**, 45–72.
- Suja-Thauvin, L., Eliassen, L., & Krokstad, J. R. (2014). The scalability of loads on large diameter monopile offshore wind support structures. In *International Wind Engineering Conference*, Hannover.
- Suja-Thauvin, L., & Krokstad, J. R. (2016). Simplified Bottom Fixed Offshore Wind Turbine in Extreme Sea States. *The 26th International Ocean and Polar Engineering Conference*, Rhodes, Greece: International Society of Offshore and Polar Engineers, p. 8.
- Suja-Thauvin, L., Krokstad, J. R., Bachynski, E. E., & de Ridder, E.-J. (2017). Experimental results of a multimode monopile offshore wind turbine support structure subjected to steep and breaking irregular waves. *Ocean Engineering*, **146**, 339–351.
- Sumer, B. M., & Fredsøe, J. (2006). *Hydrodynamics Around Cylindrical Structures. Advanced Series on Ocean Engineering*, Vol. Volume 26, WORLD SCIENTIFIC. doi:doi:10.1142/6248
- Sveen, J. K., & Cowen, E. A. (2004). Quantitative imaging techniques and applications to wavy flows. In *PIV and Water Waves*, Vol. Volume 9, WORLD SCIENTIFIC, pp. 1–49.
- Tanaka, M. (1983). The Stability of Steep Gravity Waves. *Journal of the Physical Society of Japan*, **52**(9), 3047–3055.

- Tanaka, M. (1985). The stability of steep gravity waves. Part 2. *Journal of Fluid Mechanics*, **156**, 281–289.
- Tanimoto, K., Takashi, S., Kaneko, T., & Shiota, K. (1986). Impact force of breaking waves on an inclined pile. In *5th Int. OMAE Symp.*, Tokyo, Japan, p. 1:235-241.
- Teledyne Dalsa website. (2018). FALCON2 datasheet. Retrieved from <https://www.teledynedalsa.com/en/products/imaging/cameras/falcon2/>
- Tromans, P., Swan, C., & Masterton, S. (2006). *HSE Health & Safety Executive Nonlinear potential flow forcing: the ringing of concrete gravity based structures A summary report*. Retrieved from <http://www.hse.gov.uk/research/rrpdf/rr468.pdf>
- Veic, D., Kraskowski, M., & Bugalski, T. (2016). Bottom Fixed Substructure Analysis, Model Testing and Design for Harsh Environment BT - MARE-WINT: New Materials and Reliability in Offshore Wind Turbine Technology. In W. Ostachowicz, M. McGugan, J.-U. Schröder-Hinrichs, & M. Luczak, eds., , Cham: Springer International Publishing, pp. 193–211.
- Weiss, J. (1991). The dynamics of enstrophy transfer in two-dimensional hydrodynamics. *Physica D: Nonlinear Phenomena*, **48**(2), 273–294.
- Welch, S., Levi, C., Fontaine, E., & Tulin, M. P. (1999). Experimental Study of the Ringing Response of a Vertical Cylinder In Breaking Wave Groups. *International Journal of Offshore and Polar Engineering*, **9**(04), 7.
- Wienke, J., & Oumeraci, H. (2005). Breaking wave impact force on a vertical and inclined slender pile—theoretical and large-scale model investigations. *Coastal Engineering*, **52**(5), 435–462.
- Wienke, J., Sparboom, U., & Oumeraci, H. (2000). Breaking Wave Impact on a Slender Cylinder. *Coastal Engineering 2000*. doi:doi:10.1061/40549(276)139
- Wienke, J., Sparboom, U., & Oumeraci, H. (2001). *Breaking Wave Impact on a Slender Cylinder. Coastal Engineering 2000 - Proceedings of the 27th International Conference on Coastal Engineering, ICCE 2000*, Vol. 276. doi:10.1061/40549(276)139
- Williamson, C. H. K. (1985). Sinusoidal flow relative to circular cylinders. *Journal of Fluid Mechanics*, **155**, 141–174.
- Wu, J.-Z., Lu, X.-Y., & Zhuang, L.-X. (2007). Integral force acting on a body due to local flow structures. *Journal of Fluid Mechanics*, **576**, 265–286.
- Zhou, J., Adrian, R. J., Balachandar, S., & Kendall, T. M. (1999). Mechanisms for generating coherent packets of hairpin vortices in channel flow. *Journal of Fluid Mechanics*, **387**, 353–396.